PANS METHOD FOR TURBULENCE: SIMULATIONS OF HIGH AND LOW REYNOLDS NUMBER FLOWS PAST A CIRCULAR CYLINDER

A Thesis

by

SUNIL LAKSHMIPATHY

Submitted to the Office of Graduate Studies of
Texas A&M University
in partial fulfillment of the requirements for the degree of

MASTER OF SCIENCE

December 2004

Major Subject: Aerospace Engineering

PANS METHOD FOR TURBULENCE: SIMULATIONS OF HIGH AND LOW REYNOLDS NUMBER FLOWS PAST A CIRCULAR CYLINDER

A Thesis

by

SUNIL LAKSHMIPATHY

Submitted to Texas A&M University
in partial fulfillment of the requirements
for the degree of

MASTER OF SCIENCE

Approved as to style and content by:

Sharath S. Girimaji (Chair of Committee)	Paul Cizmas (Member)
Prabir Daripa (Member)	Walter Haisler (Head of Department)

December 2004

Major Subject: Aerospace Engineering

ABSTRACT

PANS Method for Turbulence: Simulations of
High and Low Reynolds Number Flows Past a
Circular Cylinder. (December 2004)
Sunil Lakshmipathy, B.E., Bangalore University
Chair of Advisory Committee: Dr. Sharath S. Girimaji

The objective of the study is to investigate the capability of PANS (Partially Averaged Navier-Stokes Simulation) model over a wide range of Reynolds numbers and flow physics. In this regard, numerical simulations of turbulent flow past a circular cylinder are performed at Re_D 140,000 and Re_D 3900 using the PANS model. The high Reynolds number PANS results are compared with experimental results from Cantwell and Coles, Large Eddy Simulation results from Breuer, and Detached Eddy Simulation results from Travin et al. Low Reynolds number PANS results are compared with experimental results from Ong and Wallace and Large Eddy Simulation results from Breuer. The effects of the various PANS parameters (f_k, f_ε, σ_{ku}, $\sigma_{\varepsilon u}$) on the ability to capture turbulence physics at various Reynolds numbers are studied. It is confirmed, as previously predicted from theoretical considerations that: (i) for high Reynolds number flow $f_\varepsilon = 1$ and $\sigma_{ku} = \sigma_k \times f_k^2 / f_\varepsilon$ are most appropriate; and (ii) for low Reynolds number flow $f_\varepsilon = f_k$ and $\sigma_{ku} = \sigma_k$ are most suitable. These choices for the parameters stem from the fact that there is no clear separation of scales between the energy scales and the dissipation scales at low Reynolds number unlike in the high Reynolds number where there is a clear separation of scales between the energy containing scales and the dissipation scales. Also, in both cases it is found that decreasing f_k leads to improved accuracy in predicting the flow statistics.

To my mother and my sister for their
love, support and encouragement.

ACKNOWLEDGMENTS

I am fortunate to have Dr Sharath S. Girimaji as my graduate advisor and the chair of my committee. His profound knowledge, innovative and relentless approach to achieve excellence has been nothing less than an inspiration and an ideal for life. I am deeply indebted to him for his steadfast support throughout my master's program. His critical and creative suggestions, along with his ingenious ways to teach various concepts, have helped in making this thesis a success.

I would like to thank Dr. Paul Cizmas and Dr. Prabir Daripa for being on my thesis committee. The courses I took under them have provided me with the background knowledge to tackle this project effectively. I am also grateful to them for reviewing my thesis and giving me insightful feedback that enabled me to turn in a competent thesis.

This section would be incomplete without mentioning my friends and their contribution to my project both professionally and personally. I can hardly forget innumerous caffeine shots I've had with Ravi Srinivasan while discussing CFD issues. These discussions have been highly beneficial and I appreciate his contribution to the success of this project. I would also like to thank my fellow graduate students, Aditya Murthi and Eunhwan Jeong, for the constructive discussions I've had during the course of this project. I would like to extend my gratitude to all my friends who have helped make my TAMU experience one to cherish for life.

I would like to thank the Aerospace Department and its administrative staff especially Ms. Karen Knabe and Ms. Donna Hollick for their patience in obliging all my bureaucratic requests and making sure my stay at TAMU went without a glitch.

Finally, I would like to thank Maria-Antonieta Bohm for her support and always giving pep-talks to make sure that I am motivated at all times and bringing out the best in me.

TABLE OF CONTENTS

LIST OF FIGURES

Page

Page

Page

Page

LIST OF TABLES

1. INTRODUCTION

1.1 INTRODUCTION TO CFD

All flows and related phenomena can be described by partial differential equations, which cannot be solved analytically except in special cases. We use various discretization methods which approximate the differential equations by a system of algebraic equations which can then be solved on a computer. The approximations are applied to a small domain in space and/or time so that the numerical solutions provide results at discrete locations in space and time. The accuracy of the numerical solutions depends on the quality of the discretizations used. CFD covers a range of activities from the automation of well-established engineering design methods to the use of the detailed solution of the Navier-Stokes equations as substitutes for experimental research into the nature of complex flows. Hence CFD complements experimental and theoretical fluid dynamics by providing an alternative cost-effective means of simulating real flows. Figure 1 gives a brief overview of the CFD process, where the partial differential equations are discretized into a system of algebraic equations using several discretization schemes. This system of algebraic equations can then be solved to produce the numerical solutions which could be interpreted to obtain useful results.

CFD offers several advantages compared to experimental methods as, it is not limited to a certain range of Reynolds number and also it provides the convenience of being able to switch off specific terms in the governing equations. CFD provides five major advantages compared with experimental fluid dynamics:

- Lead time in design and development is significantly reduced.
- CFD can simulate flow conditions not reproducible in experimental model tests.
- CFD provides more detailed and comprehensive information.
- CFD is increasingly more cost effective than wind tunnel testing.
- CFD typically incurs lower energy consumption.

This thesis follows the style of *Flow, Turbulence and Combustion.*

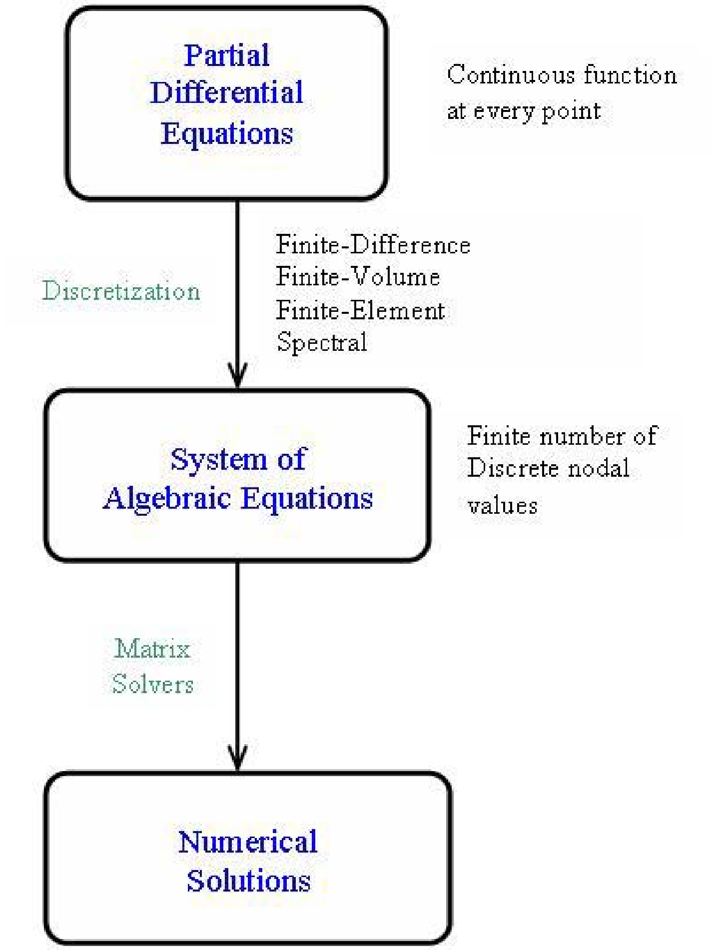

Figure 1: Overview of CFD

CFD, particularly in the field of engineering, is still at the stage of development where, problems involving complex geometries can be treated with simple physics and those involving simple geometry can be treated with complex physics. With the advancement in computer hardware and numerical algorithms, the accepted norm for simplicity and complexity is changing.

1.2 FLOW PAST BLUFF BODIES

In many engineering situations, flow past bluff bodies generate complex phenomena such as multiple separations with partial reattachment, vortex shedding, bi-modal flow behavior, high turbulence level and large scale turbulent structures which contribute considerably to the momentum, heat and mass transport. Usually, the Reynolds number in these flows is high so that the turbulent processes are important and must be accounted for in the prediction method. The wakes produced from flow past bluff bodies typically involve the interaction of three shear layers in the same problem namely, a boundary layer, a separating free shear layer, and a wake [27].

Flow around a circular cylinder is an idealized problem of flow past a bluff body because the geometry is simple, but the flow is complex with unsteady separation. Alternating vortices are shed from the cylinder and transported downstream, where they retain their identity in a Kármán vortex street for a considerable distance. These vortices are predominantly two-dimensional, but large scale three-dimensional structures exist which lead to a modulation of the shedding frequency. Flow past a circular cylinder is physically and geometrically more complex compared to its square counterpart. The separation is not imposed by a geometric singularity as in the case of the square cylinder. Rather it depends on the boundary layer development before separation. These characteristics of the circular cylinder flow combined with an exhaustive database from both experimental and numerical studies renders this flow to be an excellent test case for validating new approaches in CFD for bluff body aerodynamics.

1.3 LITERATURE REVIEW

Flow over circular cylinder exhibits vastly different behaviors as the Reynolds number ($Re_D = VD/\nu$ based on the free-stream velocity V, cylinder diameter D, and kinematic viscosity ν) increases from zero to larger values. The cylinder flow has been subjected to numerous studies and the global statistics such as drag, lift, pressure coefficient, and Strouhal number have been examined. These statistics vary by as much as 25% from one experiment to another at a given Reynolds number [7]. This leads to the conclusion that several parameters arising from the experimental set-ups are important in the cylinder flow. These include the blockage ratio, free-stream turbulent intensity, cylinder aspect ratio, and the end boundary conditions, each of which has been subjected to numerous studies.

Based on the study by Roshko [22], Beaudan and Moin [2] gave a broad classification of the cylinder flow behavior in different regimes of Reynolds number. The flow past a cylinder can be broadly classified as sub-critical, critical, and super-critical based on the Reynolds Number of the flow. In sub-critical flows, where the Reynolds Number of the flow is less that 10^4 the separation is laminar, and the transition to turbulence occurs in the separated free shear layers. For Reynolds number higher than approximately 40 the vortices are shed at a regularly frequency forming a Kármán vortex street. The shedding frequency is characterized by Strouhal number (S_t). Typical values for drag coefficient and Strouhal number in the sub-critical range are 1.2 and 0.2. The critical range of Reynolds number, between 2×10^5 and 3.5×10^6, displays two transitions in the drag coefficient, labeled the lower and upper transitions by Roshko [22]. A laminar separation of the boundary layer is followed by transition to turbulence, reattachment and a final turbulent separation. The separation point moves from the front to the downstream side of the cylinder. The drag coefficient in this regime reduces to its lowest value of about 0.2. In the post-critical regime, beyond Reynolds number 3.5×10^6 the transition to turbulence occurs before separation. The separation-reattachment bubble in the critical region disappears. The base pressure coefficient continues its monotonic decrease started at Reynolds number 5×10^5, reaching 0.6 at about Reynolds number 8×10^6. Following that, the drag coefficient is constant at around 0.7, and the vortices are shed regularly with an approximate Strouhal frequency of 0.27 [21]. Williamson [27] performed a thorough analysis of the wake vortex dynamics of bluff bodies and discovered several new phenomena in wakes.

Several experimental and numerical studies provide complete data sets for flow over a circular cylinder at Reynolds number 3900, and 140,000 based on the cylinder diameter, both of which are in the sub-critical range, but in the cylinder flow case of Reynolds number 140,000 the boundary layer is much thinner and the separated free-shear layer becomes turbulent quickly.

Beaudan and Moin [2] were among the first to perform Large Eddy Simulations (LES) of flow past a circular cylinder at $Re_D = 3900$. They solved the compressible Navier-Stokes equation on an O-grid with fifth order accurate and seventh order accurate upwind-biased scheme. Based on their calculations they concluded that the high order upwind scheme was highly dissipative in the wake and hence ill-suited for LES. Lourenco and Shih [16] performed experimental studies on the cylinder flow at $Re_D = 3900$ using the Particle Image Velocimetry. Ong and Wallace [19] performed experimental studies for the same case using hot-wire probes. Both the experiments provide valuable data for near-wake statistics. Mittal and Moin [18] performed LES of the same case by solving the incompressible Navier Stokes equations on a C-grid using the central difference scheme of second order. They employed a Fourier-spectral method in the spanwise direction in conjunction with the periodic boundary condition. Their results for the mean flow field did not differ much from the one of Beaudan and Moin [2], their power spectra in the near wake were in better agreement with the experiments since there is no numerical dissipation and the smaller scales are more energetic. Numerical and modeling aspects of Large Eddy Simulations of the flow past a circular cylinder at $Re_D = 3900$ were studied by Breuer [3]. He investigated five different discretization schemes and with dynamic and Smogorinsky subgrid-scale models. This work confirmed the earlier findings that central difference schemes are better suited than the higher order upwind schemes. In addition, he concluded that the dynamic model combined with central difference schemes yields the best results, which agree well with the experimental measurements. Kravchenko and Moin [14] performed simulations of the flow past circular cylinder at $Re_D = 3900$. They concluded that the numerical method based on the B-spline was the most accurate scheme compared to the central difference schemes and upwind schemes. Their simulations agreed well with the experimental data of Lourenco and Shih [16] and Ong and Wallace [19]. Also they emphasized on the influence of numerical resolution and the spanwise domain size of the three dimensional simulations. They found that inadequate grid resolution can cause early transition in the shear layers separating from the cylinder which leads to inaccurate predictions of the near-wake flow statistics. In each of the above case, the spanwise extent of the computational domain was πD. Ma et al. [17] performed both DNS and LES calculations with a spectral finite element method, solving the incompressible equations in a box shaped domain. They showed the two converged states of the flow field in the very near wake exist, that are related to the shear layer transition and depend on the spanwise extent of the computational domain. Another DNS was performed by Tremblay et al. [25]. They performed their simulations in a box shaped domain with spanwise extent of πD. They solved the incompressible equations with finite volume method and central difference using the Cartesian grid method developed and thus successfully demonstrated the capability of using Cartesian method to provide reliable solutions in an efficient way for flow around bodies of arbitrary shape. They also obtained a larger recirculation length than in the experiment of Lourenco and Shih [16], but nearly 20% shorter than the one of Ma et al. [17] for the corresponding size. Hansen and Forsythe [11] performed DES simulations, using *Cobalt,* an unstructured finite volume code to solve the problem of flow past a circular cylinder at $Re_D = 3900$. They mainly studied the effects of grid resolution on the solution and the effects of using unstructured grids for turbulence resolving calculations. With sufficient grid resolution, grid independence was achieved in some of the variables examined and the global statistics of drag, recirculation zone length, and Strouhal number were well within the range of experimental uncertainty.

Cylinder flows in the upper sub-critical regime ($Re_D = 140{,}000$) were first studied in detail by Cantwell and Coles [5] in laboratory experiments. The complexity of this flow due to high Reynolds number makes it a challenging case to study. The boundary layer is about six times thinner ($\delta \approx 1/\sqrt{Re}$). There is large scale vortex motion in the wake. Cantwell and Coles [5] studied the near wake of a circular cylinder at a Reynolds number of 140,000. They used X-ray hot wire probes for measurements. Achenbach [1] performed experimental studies of flow around smooth cylindrical surfaces for $6\times10^4 < Re_D < 5\times10^6$. He studied the distribution of the pressure coefficient and skin friction around the circular cylinder for various Reynolds number. He also studied the effect of Reynolds number on the separation angle. Breuer [4] was among the first to perform LES calculations of the circular cylinder flow with $Re_D = 140,000$. This was a continuation of his previous work with $Re_D = 3900$ [3]. He ran several cases to evaluate the performance of LES calculations using both dynamic modeling and smagorinsky modeling with different values for smagorinsky constant. The numerical simulations were in satisfactory agreement with the experimental data of Cantwell and Coles [5], especially in the near wake. The study focused on the effects of grid resolution, spanwise extent of the calculation domain (1D-πD) and sub-grid scale model. The predicted Strouhal number is higher than that measured by Cantwell and Coles [5], but is in reasonable agreement with other measurements at a similar Reynolds number. Also, contrary to the belief, the fine grid results compared poorly with the experimental results of Cantwell and Coles [5] than the coarse grid results. The predicted velocity statistics did not match the experimental results closely. Breuer concluded that the grid resolution studies did not lead to improved results in terms of accuracy. He also concluded that the dynamic model gave the best results but was not decisively better than the Smogirinsky model for this flow. Travin et al. [24] performed DES of flow past circular cylinder at $Re_D = 140,000$ using structured grids and fifth order upwind code. However they modified the inflow to produce boundary layer separation in agreement with experiment. Wang et al. [26] performed simulations of circular cylinder flow at supercritical Reynolds number. They used LES with wall modeling to study the high Reynolds number flow thus alleviating the need for near wall grid resolution. The overall results were fairly good at $Re_D = 5\times10^5$ and 1×10^6. Roshko [22] performed experimental measurements on a large circular cylinder in Reynolds number 10^6 to 10^7. His study mainly focused on the variation of the drag coefficient in this Reynolds number range. In his experiments, he also introduced a splitter plate at various locations in the wake region and noticed that introducing the splitter plate in the transcritical regime had no effects on the drag coefficient C_d and the cylinder back pressure coefficient C_{pb}. This observation was in stark contrast to earlier studies which showed effects of reduced drag and subdued shedding when the splitter plate was introduced in the subcritical regime.

1.4 OBJECTIVE

The primary objective of this present research is to perform Pantially Averaged Navier Stokes simulations of flow past circular cylinder at Re_D = 3900 and 140,000. Flow past a circular cylinder has become a benchmark for any numerical prediction method due to its simple geometry yet challenging due to the nature of the flow which includes flow separation, transition to turbulence in the thin shear layers that separate and shed large scale vortices. Also availability of complete data sets from both experimental and numerical studies makes the case of flow past a circular cylinder at Re_D = 3900 and 140,000 an appropriate choice to validate the new technique of turbulence modeling using PANS method. Past attempts at simulating the sub-critical regime with k-ε model reveal the inability of the Reynolds-averaged approach to accurately predict the near-wake statistics. DNS simulations require no extra assumptions, but are computationally demanding in terms of memory and CPU time and hence restricted to flows with low Reynolds number and are unsuitable for complex engineering flows. LES gives fairly good results but expensive for high Reynolds number flows. It cannot predict the separation since there is no LES content in the shear layer. The super-critical range of flow, where the separation is turbulent is out of reach of whole-domain of LES. Therefore applying PANS method which is a new method of simulation seems an ideal choice to numerically predict the flow accurately.

In performing PANS of flow past a circular cylinder, our objectives are to take advantage of the viability and accuracy of this numerical method (i) compute the global statistics of drag, lift, shedding frequency; (ii) to obtain the mean statistics of flow at various domains in the wake region. A boxed domain is chosen to perform the simulations. The spanwise length is chosen similar to the spanwise domain length of available numerical simulations of LES and DES simulations for effective comparison. Effect of grid resolution and time resolution on the accuracy of the solution will be studied. Comparison of the present work with existing data from both numerical and experimental studies would validate the performance of PANS as a suitable choice for predicting engineering flows.

1.5 THESIS OUTLINE

The next section compares the PANS method used in this report with other existing methods. Section 3 describes the CFD tools used to generate the grid and perform numerical simulations. The description of the test cases is presented in Section 4. Section 5 and 6 present the results and discussion of the numerical simulations performed and their comparisons with experimental and numerical data for Re_D 140,000 and Re_D 3900 respectively.

2. CURRENT COMPUTATION METHODS AND RAISON D'ÊTRE OF PANS

Current turbulence computation method options are DNS, LES, RANS and hybrid methods. First, we will discuss each one of these options in detail and then motivate the need for PANS method.

2.1 DIRECT NUMERICAL SIMULATIONS

DNS of the three-dimensional Navier-Stokes equations provide comprehensive data to study turbulence, including quantities that cannot be accurately measured experimentally. Direct solution of the Navier-Stokes equations had been made possible by the development of fast digital computers, with the first simulation of isotropic turbulence appearing in the 1970's [15]. Since that time there have been notable advances in algorithms relating to spectral methods and high order finite difference schemes. However, for the most part simulations of more complicated flows have depended for their feasibility on further developments in computer hardware. With the advent of massively parallel computing the range of flows that can be treated by DNS is increasing. In a DNS no turbulence model is applied so that motions of all sizes have to be resolved numerically by a grid which is sufficiently fine. Hence, the computational requirements increase rapidly with Re.

To appreciate the limitations of DNS we need to know something about the flows we are trying to compute. Turbulence is a highly non-linear phenomenon with a wide range of spatial and temporal scales. The large scales are usually fixed by the geometry of the flow, while the smallest scales are determined by the flow itself. Estimates for the size of the smallest scales are available from simple dimensional reasoning. The Kolmogorov microscale η is defined as:

$$\eta = \left(\frac{\upsilon^3}{\varepsilon} \right)^{1/4}$$

based on the assumption that η depends only on the fluid viscosity ν and the rate of dissipation of energy ε. Upon further assumptions that for a flow in equilibrium the production is equal to dissipation, we can relate the Kolmogorov scales to the flow Reynolds number. The production can be assumed to scale as U^3/L where U is the reference bulk velocity and L a length scale of the problem, usually fixed by the geometry. Both U and L are characteristic of the largest scales of the turbulence. Thus we can write

$$\frac{\eta}{L} \approx \mathrm{Re}^{-3/4}$$

where Re = UL/ν is the bulk Reynolds number of the flow. The number of grid points N that we will require for a given simulation will be proportional to L/η and hence to $\mathrm{Re}^{3/4}$. We can now extend our prediction of increase in N over time from the previous section to increase in Re over time. A doubling of Reynolds number will require a factor of 2.2 to 2.5 increases in N at a total cost increase of a factor of 37 to 76. At the current rate of increase of computer performance and assuming that algorithms can be made to continue scaling efficiently, this leads to potential doubling of Reynolds number every 6 to 7 years [15].

According to this estimate a DNS channel flow at $\mathrm{Re} = 10^6$ for example would take around hundred years on a computer running at several GFLOPS. This is obviously not feasible. Moreover, in an expensive DNS a huge amount of information would be generated which is mostly not required by the practical user. A typical user would mostly be content by knowing the average flow statistics and some lower moments to a precision of a few percent. Hence for many applications a DNS which is of great value for theoretical investigations and model testing is not only unaffordable but would also result in a computational overkill.

2.2 LARGE EDDY SIMULATIONS

LES uses a coarser grid for the simulations. The coarser grid is able to resolve only the larger eddies in the flow but not the ones which are smaller than the individual cell dimensions. From the physical point of view, however, there is an interaction between the motions on all scales so that the result for the large scales would generally be inaccurate without taking into the account the influence of the fine scales on the large ones. This requires a sub-grid scale model. Hence a model for the unresolved motion has to be devised and an intricate coupling between physical and numerical modeling is generated. Direct computation of large scales of the flow, while modeling only the smaller ones and not the entire spectrum is an advantage of the LES approach compared to the methods based on the Reynolds Averaged Navier Stokes (RANS) equations. By resolving the large eddies, LES gives access to the flow-dependent unsteady motion so that it can, for example be used to study aero-acoustics, fluid structure coupling, or the control of turbulence by an appropriate unsteady forcing.

In LES, the larger turbulent structures are resolved, while the smaller structures which are unresolved are modeled using subgrid scale models. This is carried out by descretization of the Navier Stokes equation and thereby splitting it into large and small scales, since the latter cannot be resolved by the descretized system. Subgrid-scale modeling is a particular feature of LES and distinguishes it from all other approaches. It is well known that in three-dimensional turbulent flows energy cascades, on an average from large to small scales. The primary task of SGS model therefore is to ensure that the energy drain in the LES is the same as that obtained with the cascade fully resolved as in a DNS. If the grid scale is much finer than the dominant scales of the flow even a crude model would suffice to yield the right behavior of the dominant scales. On the other hand, if the grid scale is coarse and close to the most energetic, anisotropic, and inhomogeneous scales, the SGS model should be of better quality. Obviously, there exist two possible approaches; one is to improve the SGS model and the other is to refine the grid. In the limit, the SGS contribution vanishes and the LES turns into a DNS. Refining the grid however is restricted due to rapidly increasing computational cost. The alternative strategy, like solving an additional transport equation in a more elaborate SGS model, can be comparatively inexpensive.

One of the first used SGS models was the Smagorinsky model (SM). Like most of the present SGS models it employs the concept of an eddy viscosity, relating the traceless part of the SGS stresses to the strain rate through a coefficient of proportionality called the eddy viscosity of residual motions which involves the Smagorinsky lengthscale (analogous to mixing lengthscale), l_s and the Smagorinsky coefficient C_s. The main reason for the frequent use of the SM is its simplicity. Its drawback is that the parameter $C_{s,}$ the Smagorinsky coefficient, has to be calibrated and its optimal value may vary with the type of flow, the Reynolds number, or the discretization scheme. The kind of damping to be applied near a wall is a further point of uncertainty. Also, the SM is strictly dissipative and does not allow for backscatter and is inappropriate for simulating transition [15].

For physical reasons one would prefer to change the constant value of C_s, by a value changing in space and time. The dynamic procedure has been developed by Germano et al. [8] in order to determine such a value from the information provided by the resolved scales, in particular the ones close to the cut-off scale. The advantage of this is that the parameter of the SM is no longer required from the user but is determined *in situ* during computation. In fact, it is automatically reduced close to walls and vanishes for well resolved laminar flows. Negative values of C_s are possible and can be viewed as a way of modeling backscatter although the fidelity to turbulence physics of such a model is debatable.

The shortcomings and limitations of LES are described in detail by Jiménez and Moser [13]. LES lies between DNS and RANS in terms of computational requirements. Therefore it would still be expensive to perform LES for high Reynolds number flows. In LES calculations, the filtering of the energy containing scales is explicitly performed by specifying the grid spacing. Scales of motion which cannot be resolved by the grid are modeled using subgrid scale models. In order to keep the computational costs of LES calculation viable for high Reynolds number flows, the subgrid scale models are less complicated than RANS. The subgrid scale models perform very poorly in predicting the subgrid stresses. The presence of a wall in the turbulent regime causes LES to be extremely costly due to a vanishingly small viscous sublayer which must be resolved. Therefore cases with flow separation leading to a thin shear layer as in the cylinder flow problem with high Reynolds number is out of reach of whole-domain of LES.

2.3 REYNOLDS AVERAGED NAVIER-STOKES SIMULATIONS

In RANS models, we solve the Reynolds equations for the mean velocity field. The Reynolds stresses – which appear as unknowns in the Reynolds equations- are determined by a turbulent model, either via the turbulent viscosity hypothesis or more directly from modeled Reynolds-stress transport equations. The turbulent viscosity models are based on the turbulent viscosity hypothesis. According to the hypothesis, the Reynolds stresses are given by:

$$\langle u_i u_j \rangle = \frac{2}{3} k \delta_{ij} - \nu_T \left(\frac{\partial \langle U_i \rangle}{\partial x_j} + \frac{\partial \langle U_j \rangle}{\partial x_i} \right)$$

or, in simple shear flow, the shear stress is given by

$$\langle uv \rangle = -\nu_T \frac{\partial \langle U \rangle}{\partial y}$$

Given the turbulent viscosity field $\nu_T(x,t)$, the above equation provides a most convenient closure to the Reynolds equations, which then have the same form as the Navier-Stokes equations. It is unfortunate that the accuracy of the turbulent viscosity hypothesis is poor.

The k-ε model is the most widely used complete RANS model and it is incorporated in most commercial CFD codes. In this model, the model transport equations are solved for two turbulence quantities i.e, k and ε. From these quantities, we can device equations for the length scale ($L = k^{3/2}/\varepsilon$), a timescale ($\tau = k/\varepsilon$), and a quantity of dimension $\nu_T(k^2/\varepsilon)$, etc. This makes the two equation models complete. In addition to the turbulent viscosity hypothesis, the k-ε consists of

1. the model transport equation for k (which is the same as that in the one equation model);
2. the model transport equation for ε; and
3. the specification of the turbulent viscosity as

$$\nu_T = C_\mu k^2/\varepsilon,$$

where $C_\mu = 0.09$ is one of the five model constants. The model transport equations for k and ε are developed as explained in Pope [20]. They are

$$\frac{\overline{D}k}{\overline{D}t} \equiv \frac{\partial k}{\partial t} + \langle U \rangle \bullet \nabla k \equiv P - \varepsilon + \vec{\nabla} \bullet \left(\frac{\nu_T}{\sigma_k} \nabla k \right)$$

$$\frac{\overline{D}\varepsilon}{\overline{D}t} = \nabla \bullet \left(\frac{\nu_T}{\sigma_\varepsilon} \nabla \varepsilon \right) + C_{\varepsilon 1} \frac{P\varepsilon}{k} - C_{\varepsilon 2} \frac{\varepsilon^2}{k}$$

The standard values for all the model constants due to Launder and Sharma(1974) are

$$C_\mu = 0.09,\ C_{\varepsilon 1} = 1.44,\ C_{\varepsilon 2} = 1.92,\ \sigma_k = 1.0,\ \sigma_\varepsilon = 1.3.$$

The k-ε model is arguably the simplest complete turbulent model and hence it has the broadest range of applicability and has been applied to a diverse range of problems including heat transfer, combustion, and multi phase flows. Although it predicts simple turbulent flows with reasonable accuracy, it can be inadequate for complex flows, to the extent that the calculated mean flow patterns can be even qualitatively incorrect. The inaccuracies stem from the turbulent-viscosity hypothesis and from the ε equation. Higher order RANS closures (e.g. Second moment closures) can yield more accurate constitutive relations than eddy-viscosity hypothesis. But they are still handicapped by the shortcomings of the ε equation.

The RANS method necessarily averages the entire spectrum of turbulent structures. While often adequate in steady turbulent flows with no regions of flow reversal, or possibly exhibiting shallow separations, it is inevitable that RANS turbulent models will be unable to accurately predict phenomena dominated by large scale unsteadiness (e.g. massive separation). Unsteady massively separated flows are characterized by geometry-dependent and three dimensional turbulent eddies. These unsteady eddies, which are flow dependent defeat the RANS capability to accurately predict complexities.

2.4 HYBRID METHODS

Due to the inherent limitations of the several turbulent flow computational strategies studied earlier, new methods in the form of hybrid models are envisioned. There are several new hybrid models which are being tested for their effectiveness to use them in the mainstream modeling. They are DES, hybrid RANS/LES, unsteady RANS, and VLES to name a few [9]. A new addition to this list of hybrid models is the PANS method of modeling turbulence proposed by Girimaji [9].

2.5 PANS METHODOLOGY

The PANS model is purported for any degree of physical resolution – ranging from RANS to DNS. In PANS, the physical resolution is quantified in terms of the unresolved kinetic energy and unresolved dissipation. The most important feature of PANS is that it permits high fidelity computations at any desired degree of resolution. The PANS method is distinct from standard LES in three important aspects:

1. the decomposition of the velocity field is based on kinetic energy content rather than on cut-off wavenumber.
2. the filtering operation defined to decompose the instantaneous velocity into filtered component and residual component is implicit rather than explicit, requiring no filtering operation during computation; and
3. the sub-filter scale viscosity is independent of grid spacing i.e., the physical resolution is decoupled from numerical resolution.

The salient features of PANS are explained in detail by Girimaji in [10]. The following sub-sections give a summary of the important results discussed in [10].

2.6 PANS MODEL EQUATIONS

We start with the instantaneous incompressible Navier Stokes equations:

$$\frac{\partial V_i}{\partial t} + V_j \frac{\partial V_i}{\partial x_j} = -\frac{\partial p}{\partial x_i} + \nu \frac{\partial^2 V_i}{\partial x_j \partial x_j} \tag{1}$$

$$\frac{\partial^2 p}{\partial x_i \partial x_i} = -\frac{\partial V_i}{\partial x_j}\frac{\partial V_j}{\partial x_i} \tag{2}$$

Decomposing the instantaneous velocity component, V_i into resolved and unresolved components:

$$V_i = U_i + u_i \tag{3}$$

This appears analogous to the Reynolds decomposition. However, important differences are that, the average of the unresolved component is non-zero. Let $\langle\ \rangle$ denote an arbitrary (implicit or explicit) filter which is constant preserving and commutes with the spatial and temporal differentiation.

$$\begin{aligned} U_i &= \langle V_i \rangle; \\ \langle u_i \rangle &\neq 0 \end{aligned} \tag{4}$$

Applying the filtering operation to the Navier Stokes equations (1), we obtain the governing equations for the resolved velocity field U_i. The filtered Navier Stokes equations are simply

$$\frac{\partial U_i}{\partial t} + U_j \frac{\partial U_i}{\partial x_j} + \frac{\partial \tau(V_i, V_j)}{\partial x_j} = -\frac{\partial \langle p \rangle}{\partial x_i} + \nu \frac{\partial^2 U_i}{\partial x_j \partial x_j} \tag{5}$$

$$-\frac{\partial^2 \langle p \rangle}{\partial x_i \partial x_i} = -\frac{\partial U_i}{\partial x_j}\frac{\partial U_j}{\partial x_i} - \frac{\partial \tau(V_i V_j)}{\partial x_i \partial x_j} \tag{6}$$

In equations (5) and (6), $\tau(V_i V_j)$ is the generalized central second moment which is defined in general as [8]:

$$\tau(A,B)=\langle AB\rangle-\langle A\rangle\langle B\rangle\Rightarrow\tau(V_iV_j)=(\langle V_iV_j\rangle-\langle V_i\rangle\langle V_j\rangle) \tag{7}$$

The generalized third moment is give by

$$\tau(A,B,C)=\langle ABC\rangle-\langle A\rangle\tau(B,C)-\langle B\rangle\tau(C,A)-\langle C\rangle\tau(A,B)-\langle A\rangle\langle B\rangle\langle C\rangle. \tag{8}$$

The closure problem arises due to the Sub-Filter Stress (SFS) term, $\tau(V_iV_j)$ in the PANS equations. The evolution equation for the SFS term is similar in form to its RANS counterpart and is given by:

$$\frac{\partial\tau(V_iV_j)}{\partial t}+U_k\frac{\partial\tau(V_i,V_j)}{\partial x_k}=\mathrm{P}_{ij}+\Phi_{ij}-D_{ij}+T_{ij} \tag{9}$$

In the above equation, the various terms on the left-hand side (LHS) are production (P_{ij}), pressure-correlation (Φ_{ij}), Dissipation (D_{ij}) and transport (T_{ij}) of SFS stress.

$$\mathrm{P}_{ij}=-\tau(V_i,V_k)\frac{\partial U_j}{\partial x_k}-\tau(V_j,V_k)\frac{\partial U_i}{\partial x_k}; \tag{10}$$

$$\Phi_{ij}=2\tau(p',S_{ij}); \qquad S_{ij}=\frac{1}{2}\left(\frac{\partial\langle U_i\rangle}{\partial x_j}+\frac{\partial\langle U_j\rangle}{\partial x_i}\right); \tag{11}$$

$$D_{ij}=2\nu\tau\left(\frac{\partial U_i}{\partial x_k},\frac{\partial U_j}{\partial x_k}\right); \tag{12}$$

$$T_{ij}=-\frac{\partial}{\partial x_k}\left(\tau(V_i,V_j,V_k)+\tau(p,V_j)\delta_{ik}-\nu\frac{\partial\tau(V_i,V_j)}{\partial x_k}\right) \tag{13}$$

In the above, p' is the pressure field corresponding to the unresolved fluctuations.

$$\nabla^2p'=-2\frac{\partial U_i}{\partial x_j}\frac{\partial u_j}{\partial x_i}-\frac{\partial u_i}{\partial x_j}\frac{\partial u_j}{\partial x_i} \tag{14}$$

Equation (9) is invariant to the type of filter and consequently, invoking Germano's averaging invariance property [8], the SFS stress term must be invariant to the type of averaging, provided the generalized central moments are used. Based on these arguments, PANS is capable of inheriting its model form from either RANS or LES. However, most of the current sub-grid scale models used in LES are algebraic in nature and hence too elementary to be used as a basis for PANS.

In PANS, the filter and the cut-off wave-number are not known explicitly. The implied cut-off wave-number and length are taken to be λ_c and $l_c = 2\pi/\lambda_c$. The kinetic energy and the dissipation of the PANS unresolved scales of motion are defined as:

$$k_u = \tau\langle u_i u_i\rangle \tag{15}$$

$$\varepsilon_u = \upsilon\tau \left\langle \frac{\partial u_i}{\partial x_j}\frac{\partial u_i}{\partial x_j}\right\rangle \tag{16}$$

The kinetic energy and the dissipation of the total fluctuations are denoted by k and ε. In PANS, the extent of filtering is quantified by specifying the ratios of unresolved kinetic energy and unresolved dissipation [9].

$$f_k = \frac{k_u}{k} \quad ; \qquad f_\varepsilon = \frac{\varepsilon_u}{\varepsilon}. \tag{17}$$

The prescription of the resolution control parameters f_K and f_ε depends on the desired physical resolution and affordability of the numerical resolution. In PANS, unlike in LES, the numerical and physical resolutions are decoupled, requiring adequacy of the computational grid for a given f_K to ensure trustworthy simulations.

The closure for the SFS term $\tau(V_i V_j)$ can be obtained by using the Bouissinesq-type approaximation or mixing length arguments for partial fields according to:

$$\tau\left(V_i V_j\right) = -\upsilon_u\left(\frac{\partial U_i}{\partial x_j} + \frac{\partial U_j}{\partial x_i}\right) + \frac{2}{3}k_u\delta_{ij}; \tag{18}$$

where $\upsilon_u = C_\mu \dfrac{K_u^2}{\varepsilon_u}$ is the eddy viscosity of the unresolved scales. In order to solve equation (18) we need to prescribe suitable models for k_u and ε_u.

As in [9], we start with the RANS two equation k-ε model:

$$\frac{\partial k}{\partial t} + \overline{U}_j\frac{\partial K}{\partial x_j} = P - \varepsilon + \frac{\partial}{\partial x_j}\left(\frac{\upsilon_t}{\sigma_k}\frac{\partial K}{\partial x_j}\right) \tag{19}$$

$$\frac{\partial \varepsilon}{\partial t} + \overline{U}_j\frac{\partial \varepsilon}{\partial x_j} = C_{\varepsilon 1}\frac{P\varepsilon}{k} - C_{\varepsilon 2}\frac{\varepsilon^2}{k} + \frac{\partial}{\partial x_j}\left(\frac{\upsilon_T}{\sigma_\varepsilon}\frac{\partial \varepsilon}{\partial x_j}\right) \tag{20}$$

where $\overline{U}$ is the mean velocity, P is the production of the kinetic energy, ε is the dissipation rate, ν_T is the total eddy viscosity $\left(\upsilon_T = C_\mu \frac{k^2}{\varepsilon}\right)$, and $C_{\varepsilon 1}$, $C_{\varepsilon 2}$ are model coefficients.

The model equations for the unresolved kinetic energy, k_u and unresolved dissipation, ε_u are derived from the definition of the PANS resolution control parameters (17). Note that the physics of PANS dictates:

1. $0 \le f_k \le f_\varepsilon \le 1$.
2. PANS must reduce to RANS as f_K and f_ε tend to unity.
3. PANS must reduce to DNS as f_K and f_ε tend to zero.

From (17) we get:

$$k_u = f_k k \tag{21}$$

Since f_k is a constant, the evolution equation of kinetic energy for PANS and RANS can be related according to:

$$\frac{dk_u}{dt} = f_k \frac{dk}{dt} \tag{22}$$

The evolution equation for the unresolved kinetic energy can be justifiably written in classical RANS form [9].

$$\frac{\partial K_u}{\partial t} + U_j \frac{\partial K_u}{\partial x_j} = \mathrm{P}_u - \varepsilon_u + T_{ku} + \left(U_j - \overline{U}_j\right)\frac{\partial K_u}{\partial x_j}$$

$$\text{where } \mathrm{P}_u = \tau\left(V_i, V_j\right)\frac{\partial U_i}{\partial x_j}; \qquad T_{ku} = \frac{\partial}{\partial x_j}\left(\frac{\upsilon_t}{\sigma_k}\frac{\partial K_u}{\partial x_j}\right) \tag{23}$$

The unresolved-scale production $\left(\mathrm{P}_u\right)$ is due to the spectral transfer of kinetic energy from resolved to unresolved scales, and not only due to direct interaction with the mean flow. This spectral-transfer production appears in closed form requiring no further consideration. Substituting the RANS equation for kinetic energy (19) into (22), we get:

$$\frac{dK_u}{dt} = f_k\left[\mathrm{P} - \varepsilon + \frac{\partial}{\partial x_j}\left(\frac{\nu_t}{\sigma_k}\frac{\partial K}{\partial x_j}\right)\right] \tag{24}$$

To achieve the required f_k equations (23) and (24) must be consistent with one another. Thus, this consistency requirement is used to impose the implicit filtering in the PANS procedure. From these equations we can write

$$\mathrm{P}_u - \varepsilon_u + T_{ku} = f_k \left(\mathrm{P} - \varepsilon + \frac{\partial}{\partial x_j}\left(\frac{\nu_t}{\sigma_k} \frac{\partial K}{\partial x_j} \right) \right) - \left(U_j - \overline{U}_j \right) \frac{\partial K_u}{\partial x_j} \tag{25}$$

The relationship between various RANS terms and the corresponding PANS terms are now evident. Equating the source/sink terms (local processes) we get:

$$\mathrm{P}_u - \varepsilon_u = f_k \left(\mathrm{P} - \varepsilon \right) \tag{26}$$

From this the RANS production can be expressed in terms of PANS variables (noting $\varepsilon = \varepsilon_u / f_\varepsilon$):

$$\mathrm{P} = \frac{1}{f_k}\left(\mathrm{P}_u - \varepsilon_u \right) + \frac{\varepsilon_u}{f_\varepsilon} \tag{27}$$

This relationship will be useful later to close the PANS dissipation equation. Comparing the transport terms of PANS and RANS from (25):

$$T_{ku} + \left(\overline{U}_j - U_j \right) \frac{\partial K_u}{\partial x_j} = f_k \frac{\partial}{\partial x_j}\left(\frac{\nu_t}{\sigma_k} \frac{\partial K}{\partial x_j} \right) = \frac{\partial}{\partial x_j}\left(\frac{\nu_t}{\sigma_k} \frac{\partial K_u}{\partial x_j} \right) \tag{28}$$

The model for the transport term can now be surmised:

$$\begin{aligned} T_{ku} &\equiv \frac{\partial}{\partial x_j}\left(\frac{\nu_t}{\sigma_k} \frac{\partial K}{\partial x_j} \right) - \left(\overline{U}_j - U_j \right) \frac{\partial K_u}{\partial x_j} \\ &= \frac{\partial}{\partial x_j}\left(\frac{\nu_u f_\varepsilon}{\sigma_k f_k^2} \frac{\partial K_u}{\partial x_j} \right) - \left(\overline{U}_j - U_j \right) \frac{\partial K_u}{\partial x_j} \end{aligned} \tag{29}$$

since, $\dfrac{\nu_u}{\nu_t} = \dfrac{C_\mu k_u^2 / \varepsilon_u}{C_\mu k^2 / \varepsilon} \approx \left(\dfrac{k_u}{k} \right)^2 \left(\dfrac{\varepsilon}{\varepsilon_u} \right) = \dfrac{f_k^2}{f_\varepsilon}$

Now the only unclosed term is the transport of SFS kinetic energy due to the resolved velocity fluctuations $\left(U_j - \overline{U}_j \right)$. Assuming that the resolved fluctuations do not contribute to the SFS energy transport:

$$\left(\overline{U}_j - U_j\right)\frac{\partial K_u}{\partial x_j} = 0 \tag{30}$$

The completed closure model for the SFS transport term from (29) is:

$$T_{ku} = \frac{\partial}{\partial x_j}\left(\frac{\nu_u}{\sigma_{ku}}\frac{\partial K_u}{\partial x_j}\right) \tag{31}$$

where the turbulent prandtl number $\left(\sigma_{ku}\right)$ depends on the resolved-fluctuation transport model involved:

$$\sigma_{ku} \equiv \sigma_k \frac{f_k^2}{f_\varepsilon} \tag{32}$$

We expect this model to be appropriate for high Reynolds numbers. For low Reynolds numbers, the resolved scale transport is likely to scale as

$$\left(\overline{U}_j - U_j\right)\frac{\partial k_u}{\partial x_j} \approx -\frac{\partial}{\partial x_j}\left(\frac{\nu_r}{\sigma_k}\frac{\partial K_u}{\partial x_j}\right) \tag{33}$$

where $\nu_r = \nu_t - \nu_u$. Upon substitution into equation (29) this leads to

$$\sigma_{ku} \equiv \sigma_k \tag{34}$$

This completes the modeling of the SFS kinetic energy equation.

We develop the unresolved dissipation equation based on the definition of the resolution control parameter f_ε (17).

$$\begin{aligned}\frac{\partial \varepsilon_u}{\partial t} + \overline{U}_j\frac{\partial \varepsilon_u}{\partial x_j} &= f_\varepsilon\left(\frac{\partial \varepsilon}{\partial t} + \overline{U}_j\frac{\partial \varepsilon}{\partial x_j}\right) \\ &= f_\varepsilon\left(C_{e1}\frac{\mathrm{P}\varepsilon}{K} - C_{e2}\frac{\varepsilon^2}{K} + \frac{\partial}{\partial x_j}\left(\frac{\nu_t}{\sigma_\varepsilon}\frac{\partial \varepsilon}{\partial x_j}\right)\right)\end{aligned} \tag{35}$$

As RANS variables are not known, to close the ε_u equations, all terms must be expressed in PANS variables $\left(K_u, \varepsilon_u, \mathrm{P}_u\right)$ and PANS parameters $\left(f_k, f_\varepsilon\right)$. We then have

$$\frac{\partial \varepsilon_u}{\partial t} + U_j\frac{\partial \varepsilon_u}{\partial x_j} = C_{e1} f_k\frac{\mathrm{P}\varepsilon_u}{K_u} - C_{e2}\frac{f_k}{f_\varepsilon}\frac{\varepsilon_u^2}{K_u} + \frac{\partial}{\partial x_j}\left(\frac{\nu_t}{\sigma_\varepsilon}\frac{\partial \varepsilon_u}{\partial x_j}\right) + \left(U_j - \overline{U}_j\right)\frac{\partial \varepsilon_u}{\partial x_j} \tag{36}$$

The last two remaining unclosed term are the RANS kinetic energy production, P (determined from (27)) and the transport due to the resolved scales -$\left(\overline{U}_j - U_j\right)$ term.

$$\frac{\partial \varepsilon_u}{\partial t} + U_j \frac{\partial \varepsilon_u}{\partial x_j} = C_{e1} f_k \left(\frac{\mathrm{P}_u}{f_k} - \frac{\varepsilon_u}{f_\varepsilon f_k} \left(f_\varepsilon - f_k \right) \right) \frac{\varepsilon_u}{K_u} - C_{e2} \frac{f_k}{f_\varepsilon} \frac{\varepsilon_u^2}{K_u}$$

$$+ \frac{\partial}{\partial x_j} \left(\frac{\nu_t}{\sigma_\varepsilon} \frac{\partial \varepsilon_u}{\partial x_j} \right) + \left(U_j - \overline{U}_j \right) \frac{\partial \varepsilon_u}{\partial x_j} \tag{37}$$

$$\frac{\partial \varepsilon_u}{\partial t} + U_j \frac{\partial \varepsilon_u}{\partial x_j} = C_{e1} \frac{\mathrm{P}_u \varepsilon_u}{K_u} - C_{e2}^* \frac{\varepsilon_u^2}{K_u} + \frac{\partial}{\partial x_j} \left(\frac{\nu_u}{\sigma_{\varepsilon u}} \frac{\partial \varepsilon_u}{\partial x_j} \right) \tag{38}$$

where

$$C_{e2}^* \equiv C_{e1} + \frac{f_k}{f_\varepsilon} \left(C_{e2} - C_{e1} \right)$$

As in the derivation of the unresolved kinetic energy, we assume zero resolved-scale transport for high Reynolds number flow leading to

$$\sigma_{\varepsilon u} \equiv \sigma_\varepsilon \frac{f_k^2}{f_\varepsilon} \tag{39}$$

Again for low Reynolds number flow we propose

$$\sigma_{\varepsilon u} \equiv \sigma_\varepsilon \tag{40}$$

The two-equation PANS model can be summarized as

$$\frac{dK_u}{dt} = \mathrm{P}_u - \varepsilon_u + \frac{\partial}{\partial x_j} \left(\left(\frac{\nu_u}{\sigma_{ku}} + \nu \right) \frac{\partial K_u}{\partial x_j} \right) \tag{41}$$

$$\frac{d\varepsilon_u}{dt} = f_k \left(C_{e1} \frac{\mathrm{P}_u \varepsilon_u}{K_u} - C_{e2}^* \frac{\varepsilon_u^2}{K_u} \right) + \frac{\partial}{\partial x_j} \left(\left(\frac{\nu_u}{\sigma_{eu}} + \nu \right) \frac{\partial \varepsilon_u}{\partial x_j} \right) \tag{42}$$

where

$$C_{e2}^* \equiv C_{e1} + \frac{f_k}{f_\varepsilon} \left(C_{e2} - C_{e1} \right)$$

In these equations viscous transport has also been include. The values for various coefficients are:

$$C_{e1} = 1.44\,;\; C_{e2} = 1.92\,;\; \sigma_k = 1.0\,;\; \sigma_\varepsilon = 1.3$$

For PANS, to be implemented successfully as a hybrid turbulence model, it must be consistent with the turbulent physics at various cut-off wave-numbers i.e.

1. It must function as a RANS model when the cut-off wave-number is in the largest scales of motion.
2. It must function as LES model when the cut-off wave number is in the inertial scales.
3. It must function as DNS when the cut-off wave number is in the smallest dissipation scales of motion.

Girimaji [10] performed fixed point analysis on PANS model to determine the behavior of PANS at various cut-off wave numbers in the energy spectrum. A *priori* test of PANS proved that PANS is ideally suited for performing variable-resolution simulations. Another important observation is that the PANS equations are identical to RANS equations, except that the model coefficients are modified. This enables PANS model to be implemented easily into the CFD codes without any significant changes to the code. Only the model coefficients need to be modified based on the PANS equations to implement PANS model.

Having outlined the PANS methodology, further sections deal with the applicability of PANS to cylinder flows and specification of the model parameters to yield good agreement with the experimental and other numerical data.

3. FLUENT PACKAGE DETAILS

3.1 INTRODUCTION

FLUENT is one of the many commercial packages available to perform CFD. It is also the most widely used general-purpose CFD software to perform fluid flow and heat transfer analysis of real industrial processes. Its unique capabilities include an unstructured, finite volume based solver which is near-ideal for parallel performance. Its enhanced features such as complete mesh flexibility, solver capabilities, additional models to simulate the accompanying effects of turbulence, acoustics, heat transfer, species transport, reactions and combustion, dynamic mesh modeling, makes it an ideal choice to perform CFD simulations with. In this section a brief description of the salient features of the FLUENT CFD package is presented.

Any CFD package would have the following components

1. Pre-Processing (or) grid generation utility, which breaks down the geometrical domain into discrete control volumes.
2. A front-end that contains the input specification of the problem.
3. Solution module which solves the discretized representations of the problem, and,
4. Post-processing (or) the graphics tool using which the solution to the problem is visualized.

3.2 FLUENT CFD PACKAGE DESCRIPTION

3.2.1 Pre-processing module

The pre-processing module contains tools using which the topological data pertaining to the simulated problem is input to the code. It is equipped with CAD based grid generation software in which the geometrical domain is constructed and the boundaries of the domain are declared. Once this is done, a finite-difference grid is generated on the domain. This completes the pre-processing stage of the problem specification

FLUENT is equipped with three different pre-processing modules namely,

1. GAMBIT
2. G/TURBO
3. TGRID

GAMBIT is a general purpose grid generation tool which produces high quality grids to successfully perform CFD simulations using FLUENT solver. G/TURBO is a grid generation tool that enables the rapid creation of FLUENT meshes for turbo machinery applications. TGRID performs advanced hybrid volume mesh generation using Cartesian hanging-node hexa-, tetrahedral-pyramids, and prisms (wedges or hexahedra) and 2-D meshing with triangles and quadrilaterals.

3.2.2 Front-end module

Front-end module takes the input specification of the problem and converts it to the machine executable form, while performing detailed error checking. As the geometry and the boundary details are already available, the appropriate values of the initial and boundary conditions of the problem are declared here. In addition, the other ingredients of the problem solving as the information on the fluid, details pertaining to the turbulence model to be used, solvers and under-relaxation factors employed are declared here. Also, the material property of the fluid to be used for the simulation is set. Moreover, this module also contains options to input user defined subroutines wherein special requirements pertaining to the simulated problem can be input to the code, before commencing the simulation.

3.2.3 Solution module

The solution module contains tools such as the various solvers and the parallel processing algorithms that solve the problem. Once the discretized representation of the problem is available from the previous modules; the solution module solves the problem and writes out the results both in the alphanumeric and the graphical formats. The alphanumeric output file contains a summary of the progress of the solution and the final results written out, whereas, the graphical file contains all the results in the binary form so that they can be visualized in a suitable post-processor.

3.2.4 Post processing module

This module is used help analyze the output from the solver module. Results of the simulation can be visualized using this module. In addition, this module contains advanced features using which operations/manipulations can be performed on the graphics file to obtain the results of the run in different formats as graphs (charts) or movies. The advantages of visualizing the results are that an incisive insight into the physical phenomenon occurring in the flow can be obtained. Hence, this module serves as an excellent trouble shooting tool.

3.3 FLUENT PACKAGE FEATURES

FLUENT is a state of art computer program to model fluid flows and heat transfer in complex geometries. FLUENT provides complete mesh flexibility, and hence we can solve flow problems with unstructured meshes that are generated over complex geometry with relative ease. Supported mesh types include 2D triangular/quadrilateral, 3D tetrahedral/hexahedral/pyramid/wedge, and mixed (hybrid) meshes. FLUENT also allows the user to refine or coarsen the grid based on the flow solution.

FLUENT is written in the C computer language and makes full use of the flexibility and power offered by the language. Consequently, true dynamic memory allocation, efficient data structures, and flexible solver control are all made possible. In addition, FLUENT uses a client/server architecture, which allows it to run as separate simultaneous processes on client desktop workstations and powerful compute servers, for efficient execution, interactive control, and complete flexibility of machine or operating system type.

FLUENT uses unstructured meshes which are more advantageous than using conventional, multi-block structured meshes in providing the user an option of creating meshes to model complex geometries with relative ease. FLUENT can also use body-fitted, block-structured meshes. FLUENT is capable of handling triangular and quadrilateral elements (or a combination of the two) in 2D, and tetrahedral, hexahedral, pyramid, and wedge elements (or a combination of these) in 3D.

GAMBIT is the preprocessor that is used for geometry modeling and mesh generation. It helps the CFD users to build and mesh models using its graphical user interface (GUI). The GAMBIT GUI makes the basic steps of building, meshing, and assigning zone types to a model simple and intuitive, yet it is versatile enough to accommodate a wide range of modeling applications. GAMBIT also allows the user to import the mesh created from other CAD based tools such as ACIS, Parasolid, IGES, STEP, CATIA, and CAD which describe the model geometry.

FLUENT solver is a tool where all the other CFD operations such as pre-processing, solving, and post-processing are integrated into this single module. The operations include setting boundary conditions, defining fluid properties, executing the solution, refining the grid, and viewing and post processing the results. FLUENT allows for importing the mesh files from other pre processing tools such as preBFC, ANSYS, I-DEAS, NASTRAN and PASTRAN.

FLUENT provides comprehensive modeling capabilities for a wide range of incompressible and compressible, laminar and turbulent fluid flow problems. Steady-state or transient analyses can be performed. In FLUENT, a broad range of mathematical models for transport phenomena (like heat transfer and chemical reactions) is combined with the ability to model complex geometries. FLUENT also solves flows in all speed regimes from low subsonic to hypersonic flows.

For all flows, FLUENT solves conservation equations for mass and momentum. For flows involving heat transfer or compressibility, an additional equation for energy conservation is solved. For flows involving species mixing or reactions, a species conservation equation is solved or, if the non-premixed combustion model is used, conservation equations for the mixture fraction and its variance are solved. Additional transport equations are also solved when the flow is turbulent.

Periodic flow occurs when the physical geometry of interest and the expected pattern of the flow/thermal solution have a periodically repeating nature. Two types of periodic flow can be modeled in FLUENT. In the first type, no pressure drop occurs across the periodic planes. In the second type, a pressure drop occurs across translationally periodic boundaries, resulting in ``fully-developed'' or ``streamwise-periodic'' flow.

Some of the other modeling capabilities included in FLUENT are:

- Heat transfer including forced, natural, and mixed convection, conjugate heat transfer, as well as several radiation models
- Chemical species transport and reaction, including homogeneous and heterogeneous combustion models and surface reaction models
- Free surface, Eulerian and mixture multiphase models
- Lagrangian trajectory calculation for dispersed phase modeling (particles/droplets/bubbles)
- Phase change model for melting/solidification applications
- Cavitation model
- Porous media model

Various turbulent models are available in FLUENT to model turbulent flows. These include:

- Spalart Allmaras model
- Standard κ−ε model
- Re-Normalization Group (RNG) κ−ε model
- Realizable κ−ε model
- Standard κ−ω model
- Shear Stress Transport (SST) κ−ω model
- v^2-f model
- Reynolds Stress Model (RSM)
- Large Eddy Simulation (LES) Model

All these models are available for use with both incompressible and compressible flows. FLUENT also provides the option to the user to modify constants in the turbulence models to suit the modeled problem.

FLUENT uses two numerical schemes namely segregated solver and coupled solver. The two numerical methods employ a similar discretization process (finite-volume), but the approach used to linearize and solve the discretized equations is different. In the segregated solver approach, the governing equations are solved sequentially whereas in the coupled solver approach, the governing equations of continuity, momentum, and (where appropriate) energy and species transport are solved simultaneously. The FLUENT solver also contains two forms of multigrid: algebraic (AMG) and full-approximation storage (FAS). AMG is an essential component of both the segregated and coupled implicit solvers, while FAS is an important, but optional, component of the coupled explicit solver.

FLUENT uses a control-volume-based technique to convert the governing equations to algebraic equations that can be solved numerically. This control volume technique consists of integrating the governing equations about each control volume, yielding discrete equations that conserve each quantity on a control-volume basis. The various discretization schemes used in FLUENT are first order upwind, second-order upwind, power law and QUICK. FLUENT provides the option to choose among three pressure-velocity coupling algorithms: SIMPLE, SIMPLEC, and PISO.

The post-processing tool of FLUENT which is integrated with the FLUENT solver is a powerful tool in which the results can be visualized. FLUENT also allows for solution-adaptive grid refinement to effectively reduce the numerical error in the digital solution, with minimal numerical cost. All the traditional operations as the creation of visual plots of contours, vectors, etc. can be performed using the FLUENT post processor. FLUENT software is also compatible with third party post processing software including Acuity, AVS, Fieldview, and Tecplot.

3.4 PROBLEM SOLVING STEPS

Once the problem is defined, the first step in solving the problem is to construct a geometry on which the simulation is planned. This is done using a CAD based pre-processor GAMBIT. The position of the reference coordinate frame needs is decided i.e. the placement of the (0,0,0) co-ordinate of the geometry is decided. The geometry is constructed using basic geometrical entities such as points, lines, curves, planes, etc. Being a CAD based tool, GAMBIT is equipped with advanced tools for the construction of the complex geometry.

Once the geometry is constructed, proper assignment of its boundaries in accordance to the actual physical state, is to be done. The various boundary options that are to be set include input, output, wall, symmetry, and periodic. Each of the above is known as a ’patch’ in code parlance. Any undeclared patch would be conceived by the code as a ‘wall’ by default. Additional information on handling more complicated boundary conditions is available in the solver manual. After setting the boundary types, the continuum type is set.

Once the assignment of patches is completed, the geometry is discretized into small control volumes. This processing is referred to as ‘Meshing’. Meshing usually starts from the surface and propagates into the domain interiors. Depending upon the geometry, flow details, different mesh densities may be required to capture finer details of flow, at regions of interest in the domain. A variety of options on specifying the mesh density are

- Uniform: specifies that heights of all first-row boundary-layer elements are equal to each other across the entire span (edge length or face surface area) of the attachment entity.
- Aspect ratio based: computes the first-row element heights as a fixed percentage of the edge mesh element lengths for the edge or face to which the boundary layer is attached.

Once the surface mesh is completed, the volume mesh is generated, based on whether the simulation is two-dimensional or three-dimensional. On completion of this step, the meshing operation is completed the mesh details are exported to a mesh file (.msh). The code in this step would indicate if there were any inconsistencies in the declaration of the boundary condition or other details. If need be, the mesh quality can be visualized at this point. This step concludes the pre-processing operation.

It is very important to generate a proper mesh based on the simulation set-up. The accuracy of the final solution is very much dependant on the quality of the mesh generated. This is the most time consuming part of the simulation process.

The next step is the creation of the Case file (.cas). In this all the other physical details of the problem are declared. These includes:

- the flow solver is segregated/couple
- the simulation is steady/time-based
- the simulation is laminar/turbulent, and if turbulent,
  - ⇒ the turbulent model to be used is selected.
  - ⇒ the model constants of the turbulent model used are set (usually the model parameters are set to default constant values, but there is an option to change these values based on the user requirements)
- the material properties of the fluid to be used are set
- the boundary conditions for each of the boundary entity is set

- if periodic boundaries exist, the boundary conditions for these boundaries are set.
- discretization schemes for the equation, and the under-relaxation parameters are chosen.
- convergence criteria is set
- the initial flow field is set and the solution is initialized
- the solver statistics are enabled to be printed on the default screen
- the time step and the maximum number of iterations are set

At the conclusion of this step, the case file (.cas) is written in alphanumeric format. This case file contains all the above information. Once the case file is generated, the iteration process is started. In the main FLUENT window, the residuals of the relevant parameters (mass, velocity components, turbulence parameters, etc...) as a function of number of iterations is printed as the problem is submitted to the run. Because of high computational requirements and the need to have dedicated CPU times, the FLUENT solver is usually run in batch/background mode. This helps to prioritize the execution of the run. The run would continue till the required convergence criterion is reached or till the maximum number of iterations is completed. The output data file (.dat), an alphanumeric output file is generated. This data file which contains the results from the run can be used to analyze the results.

The FLUENT post-processor which is integrated in the FLUENT solver can be used to interpret the data file (.dat) and produce plots, contour plots, etc. If required, the simulation can be restarted by using the output file to initialize the flow.

4. PANS SIMULATION SET-UP

4.1 INTRODUCTION

The simulations were conducted for two Reynolds numbers of 3900 and 140000, both of which are in the sub-critical regime. These two particular cases were chosen since they are representative of the complexity of the flow problem with a laminar separation and a transition to turbulence in the wake. Also, there is a comprehensive database from both experimental and numerical studies which makes them ideal cases to perform in order to validate the PANS method of turbulence modeling. In the following sub-sections we discuss the problem set up for both the cases.

4.2 DESCRIPTION OF THE TEST CASE FOR RE_D 3900

For our intended investigations we choose the cylinder flow problem with a Reynolds number of 3900 (based on the cylinder diameter, D and the free-stream velocity U_o). It is known from experiments, that for this Reynolds number transition takes place in the free shear layers. This flow problem has been studied by Beauden and Moin [2], Breuer [3], and Kravchenko and Moin [14]. Several cases were performed with varying f_k and f_ε values. Table I. gives a brief overview of the test cases performed. The table lists the f_k and f_ε values for each case. It also lists the grid resolution and the non-dimensionalized time-step ($\Delta t^* = \Delta t * U_o/D$) used for each case.

Table I. Summary of cases for Re_D 3900

Cases	f_k	f_ε	σ_{ku}	$\sigma_{\varepsilon u}$	grid	Δt^*
1	1.0	1.0	1.000	1.300	85 x 85	0.21
2	0.7	1.0	0.490	0.637	85 x 85 x 15	0.21
3	0.7	1.0	0.490	0.637	110 x 110 x 20	0.21
4	0.7	1.0	0.490	0.637	135 x 120 x 24	0.21
5	0.5	1.0	0.250	0.325	135 x 120 x 24	0.21
6	0.5	1.0	0.250	0.325	135 x 120 x 24	0.105
7	0.5	1.0	0.250	0.325	160 x 160 x 36	0.21
8	0.5	1.0	0.250	0.325	160 x 160 x 36	0.105
9	0.7	0.7	0.700	0.910	110 x 110 x 20	0.105
10	0.7	0.7	0.700	0.910	135 x 120 x24	0.105
11	0.7	0.7	0.700	0.910	160 x 160 x 36	0.105
12	0.5	0.5	0.500	0.650	160 x 160 x 36	0.105
13	0.7	1.0	1.000	0.637	135 x 120 x24	0.21
14	0.7	0.7	1.000	0.910	110 x 110 x 20	0.105

Because of the inherent incapability of RANS to capture 3D vortices, the RANS (f_k = 1.0) cases are performed with a 2D domain. The other cases with f_k values less than one are performed on a 3D computational domain. A computational domain which extends from -15D at the inflow to 15D at the outflow, from -15D to 15D in the cross flow direction and from 0 to πD in the spanwise direction (for 3D simulations) is used for the simulations. The domain chosen is in accordance with LES domain of Beauden and Moin [2]. The spanwise length of the cylinder chosen is identical to the spanwise length chosen by Beauden and Moin [2], Breuer [3], and Kravchenko and Moin [14] in their simulations.

No slip boundary conditions are used at the upper and lower solid walls for this low Reynolds number. In the spanwise direction of the cylinder, periodicity of the flow is assumed. At the inflow plane, which is fifteen diameters from the surface of the cylinder in the upstream region, a constant velocity field with a turbulence intensity of 2% is imposed. This value of Turbulence intensity has been found ideal for external turbulent flow simulations. Also, the flow is initialized to non-zero values for turbulent kinetic energy and turbulent eddy viscosity. Outflow boundary conditions are applied to the outlet which is fifteen diameters from the cylinder surface in the downstream region. FLUENT assumes a zero normal gradient for all flow variables except pressure at the outlet. Figure 2 gives the geometrical details of the computational domain for Re_D 3900 simulations.

Various structured O-type grids were generated for this investigation. The grids were generated using GAMBIT 2.0. Table I gives the overview of different grids used for different f_k values. Figure 3 gives the grid details of the computational domain used. Hexahedral cells form the grid structures around the cylinder. The cells are clustered in the wake region of the cylinder. To capture the boundary layer flow effectively the first grid point of the cell is at a y^+ of 22 from the cylinder surface. A y^+ value with a lower bound value of 30 is desirable. The mesh generation for 3D simulations was a clear extension of the 2D grid, but with a higher grid resolution.

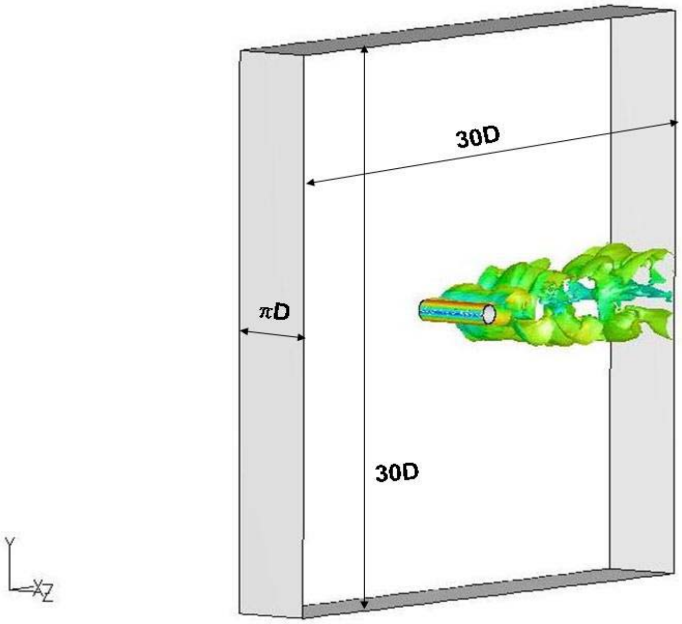

Figure 2: Geometrical details for Re_D 3900

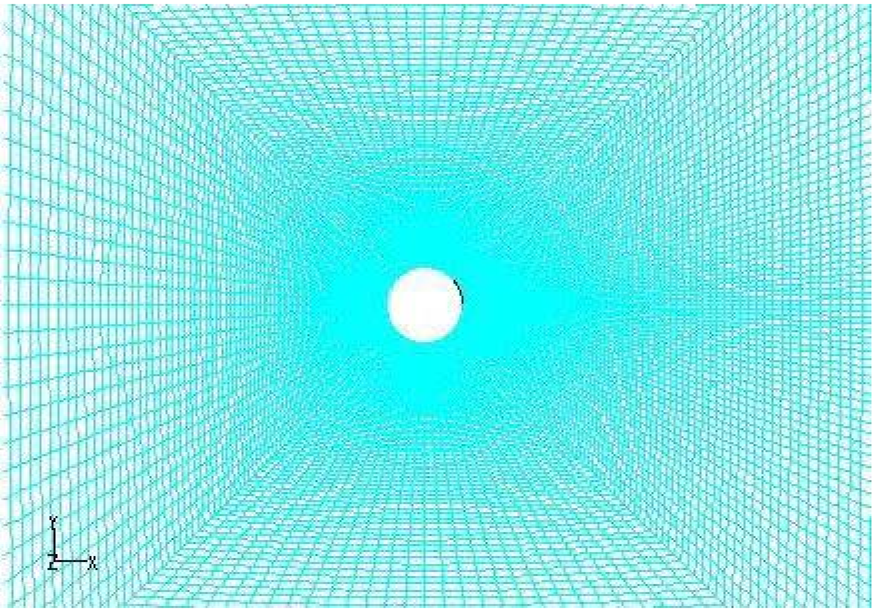

Figure 3: Grid in the vicinity of the cylinder

4.3 DESCRIPTION OF THE TEST CASE FOR RE$_D$ 140,000

The investigation of PANS for flow past a circular cylinder is also conducted for a high Reynolds number case of 140,000. At this Reynolds number the flow is still sub-critical i.e. the boundary layers at the cylinder separate laminarly and transition takes place in the free shear layers. But unlike the case of Re$_D$ 3900 case the transition to turbulence takes place close to the cylinder surface. In the wake strong vortex shedding is observed. Compared to the low-Re case the boundary layer is about six times thinner ($\delta \approx 1/\sqrt{Re}$). The simulations for this high Reynolds number were also performed for various f_k and f_ε values. Table II. gives the summary of the different cases run along with the grid resolution and the dimensionless time-step used for each case. As in the cases of Re$_D$ 3900, the RANS (f_k = 1.0) simulations were performed in a 2D domain whereas the other PANS simulations (f_k < 1.0) were performed in a 3D domain.

Table I: Summary of test cases for Re$_D$ 140,000

Cases	f_k	f_ε	σ_{ku}	$\sigma_{\varepsilon u}$	grid	Δt^*
1	1.00	1.00	1.000	1.300	85 x 85	0.21
2	1.00	1.00	1.000	1.300	101 x 101	0.21
3	0.70	1.00	0.490	0.637	125 x 135 x 32	0.21
4	0.70	1.00	0.490	0.637	125 x 135 x 32	0.105
5	0.70	1.00	0.490	0.637	125 x 135 x 32	0.0525
6	0.70	1.00	0.490	0.637	125 x 109 x 42	0.0525
7	0.70	1.00	0.490	0.637	140 x 120 x 42	0.0525
8	0.70	1.00	0.490	0.637	150 x 135 x 42	0.0525
9	0.70	0.70	0.700	0.910	125 x 135 x 32	0.21
10	0.70	1.00	1.000	0.637	125 x 135 x 32	0.21
11	0.50	1.00	0.250	0.325	125 x 135 x 32	0.21
12	0.50	1.00	0.250	0.325	125 x 135 x 32	0.105
13	0.50	1.00	0.250	0.325	125 x 135 x 32	0.0525
14	0.50	1.00	0.250	0.325	150 x 135 x 42	0.0525

No slip boundary conditions are applied to the top and bottom walls. In the spanwise direction of the cylinder, periodicity of the flow is assumed and a constant velocity profile with a turbulence intensity of 2% is imposed at the inflow plane. Also the flow is initialized with non-zero values for the turbulent kinetic energy and eddy viscosity. Experimental results predict the flow to separate with a laminar boundary layer. However Travin et al. [24] performed runs to study the effect of both laminar separation and turbulent separation by varying their inflow boundary conditions. Even thought our case set-up matches that of Travin et al. [24] to give a turbulent boundary layer separation ($\upsilon \neq 0$ at the inflow boundary; also $\upsilon \neq 0$ in the initial conditions) we are not specifically aiming for getting the separation right. At the outflow, outflow boundary conditions are imposed which assumes fully developed conditions of the flow. The computational domain is a square cross section of 30D × 30D as shown in figure 4. The spanwise length of the domain is 2D. This value was chosen for the length of the cylinder as it was consistent with the spanwise length chosen for other numerical studies performed by Breuer [4] and Travin et al. [24]. Figure 4 gives the geometric details of the computational domain used for the high Reynolds number case.

Various O-type structured grids were developed for the different cases run. GAMBIT 2.0 was used in generating the grids. The grid structure for the high Reynolds number calculations is similar to that of the low Reynolds number calculations except that first grid point is much closer to the cylinder. Hexahedral cells form the grid structures around the cylinder. To capture the boundary layer flow effectively the first grid point of the cell is at a y^+ of 22 from the cylinder surface. The mesh generation for 3D simulations was a clear extension of the 2D grid, but with a higher grid resolution.

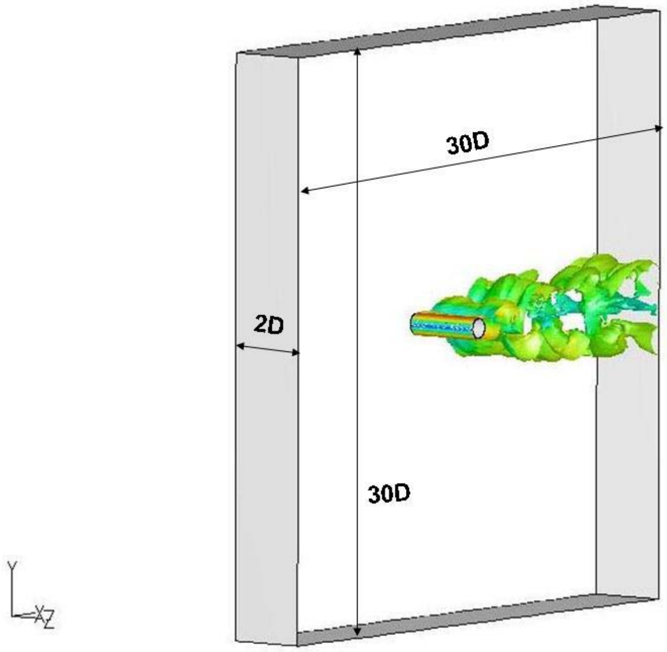

Figure 4: Geometrical details for Re_D 140,000

Table III. gives the various simulation settings used in FLUENT to perform the PANS simulation of flow past a circular cylinder at Re_D 3900 and Re_D 140,000.

Table II: PANS simulation settings

Settings	**Choice**
Simulation type	3D, Unsteady
Solver	Segregated, implicit
Temporal discretization	2nd order
Turbulence Model	k-ε Model (2eqn.) with modified PANS parameters
Pressure	PRESTO
Pressure-velocity coupling	SIMPLE
Momentum	2nd order upwind
Turbulent kinetic energy	2nd order upwind
Turbulent dissipation rate	2nd order upwind
Boundary Conditions:	
Inlet	Velocity
Outlet	Outflow
Top wall	No-slip wall
Bottom wall	No-slip wall
Lateral	Periodicity

5. RESULTS AND DISCUSSION FOR Re_D 140,000

5.1 INTRODUCTION

Several cases were performed to study the turbulent flow past a circular cylinder at Re_D 140,000 using the PANS model. A summary of these cases was provided in table II. These simulations were performed to effectively study:

1. Grid sensitivity of the solution.
2. Temporal convergence
3. Effect of f_ε
4. Effect of σ_{ku}
5. Effect of f_k

The simulations were performed for a total flow time of $300D/U_o$ time units. Initially flow data corresponding to about $120D/U_o$ is rejected. This is to allow for statistically steady vortex shedding to be established. For cases where there is large fluctuations ($f_k = 0.5$) more time was allowed for the flow to settle down and the statistics were compiled over a larger flow time. After each flow is fully developed, the data is gathered to calculate flow statistics. The instantaneous resolved quantity is decomposed into time-spanwise ensemble averaged quantity and fluctuating quantity (e.g., $U_i(t) = (U_i)_{mean}+u'$). All of the data plots are based on this decomposition.

Figure 5 gives a plot of drag coefficient as a function of time. For the case of f_k = 1.0, the drag coefficient attains steady state quickly leading to the conclusion that the flow stabilizes fairly quickly. Hence fewer samples are required to get stable statistically averaged results. Whereas for the f_k = 0.5 case, there are large fluctuations, and hence the need to obtain the statistics over a larger period of time.

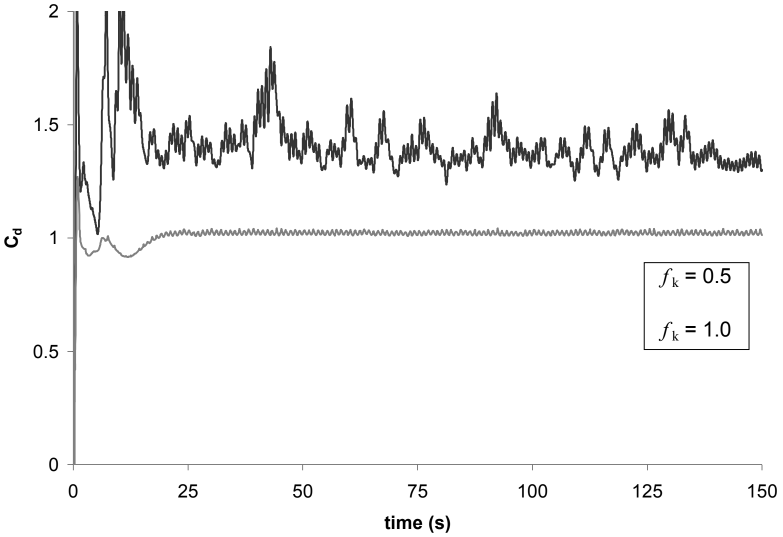

Figure 5: Time variation of the drag coefficient for various f_k values

First, we present the grid resolution and temporal resolution results for this case to validate the CFD simulations performed. Having obtained a domain with suitable grid parameters and temporally converged time step, we conduct simulations to exploit the flexibility of PANS method. Simulations are performed to study the effect of having the resolution control parameter $f_\varepsilon = f_k$ instead of fixing it to unity. Also effect of varying the turbulent prandtl number for unresolved kinetic energy (σ_{ku}) is discussed. Finally the effects of varying the cut-off i.e. reducing f_k value are discussed. Also comparison studies of results obtained from PANS calculations with available experimental results and numerical simulations are presented.

5.2 GRID SENSITIVITY STUDY

A systematic study has been performed to study the effects of grid resolution and temporal resolution. Several simulations were run to study the effect of grid resolution on various PANS cases with different f_k values. In this section, we present the results from resolution studies performed on PANS with f_k value of 0.7. Cases (6), (7), and (8) were simulated with various grid resolutions as indicated in table II for this study. All these simulations were performed with a same time-step ($\Delta t^* = 0.0525$). There was a systematic increase in the grid resolution till the compiled mean statistics were within 5% of the mean statistics obtained from the previous grid. In the following paragraphs we present the results from the grid resolution studies to illustrate the trustworthiness of the CFD simulations performed.

Figure 6 gives the comparison plot of mean streamwise velocity along the wake centerline ($y = 0$) for three PANS cases with different grid resolution. Experimental results from Cantwell and Coles [5], LES results from Breuer [4], and DES results from Travin et al. [24] are also plotted alongside for comparison purposes. We can clearly observe that there is very little variation in the mean x-velocity along the wake centerline when we refine the grid from case (6) to case (7). Further refinement of the grid as in case (8) does not change the mean flow statistics and the mean streamwise velocity plot almost overlaps the result obtained from the previous grid resolution (case (7)).

Figures 7, 8, and 9 give the mean velocity statistics at different planes in the cylinder wake region for the various PANS results studied. As in figure 6, we observe that the solution is fairly insensitive to any further grid refinement from case (7) to case (8). These results further demonstrate that PANS calculation is insensitive to any further grid refinement.

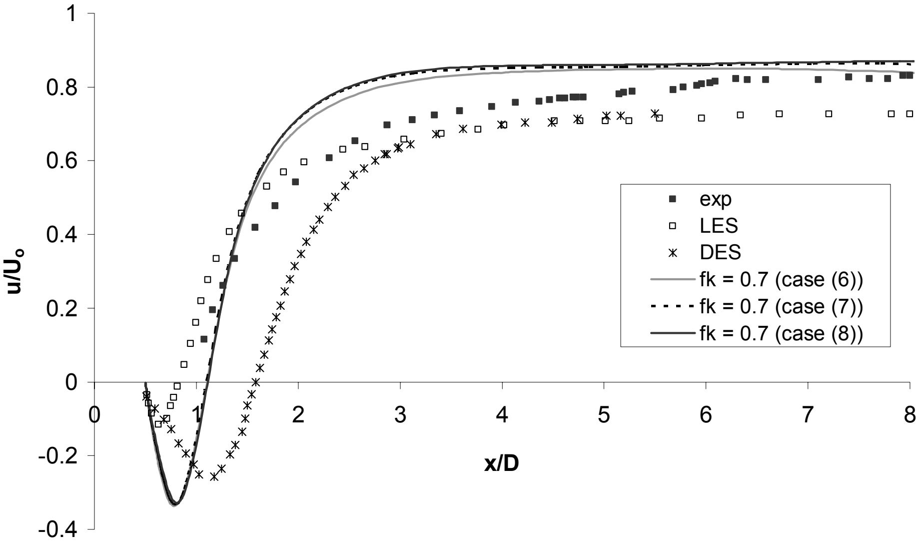

Figure 6: Grid sensitivity study for PANS cases with *f*$_k$ = 0.7. Comparison of the mean streamwise velocity at wake centerline

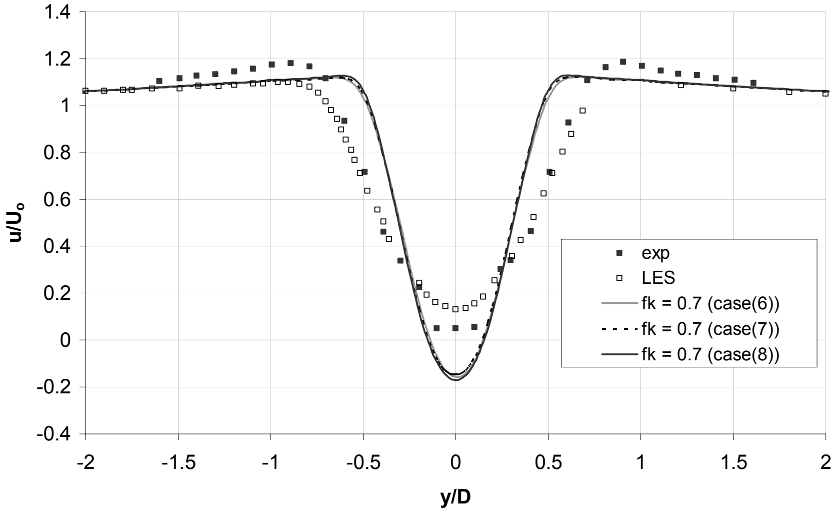

Figure 7: Grid sensitivity study for PANS cases with *f*$_k$ = 0.7. Comparison of the mean streamwise velocity at x/D = 1.0 plane

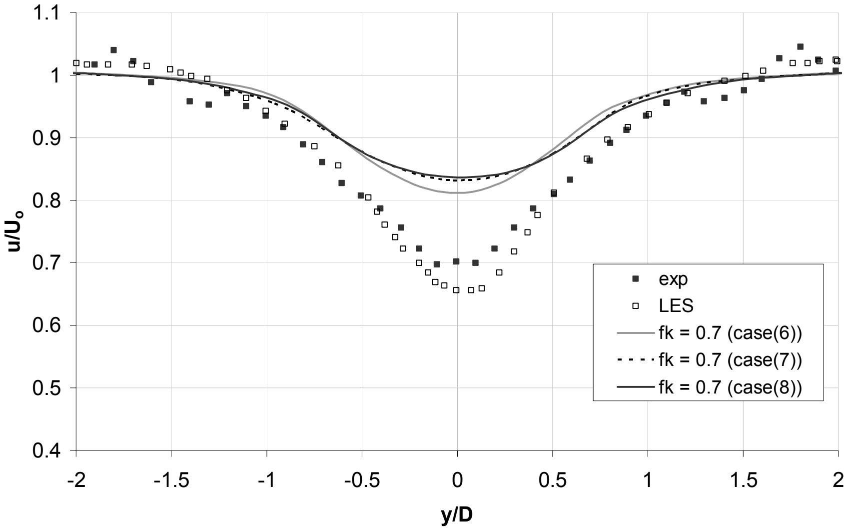

Figure 8: Grid resolution study for PANS cases with $f_k = 0.7$. Comparison of the mean streamwise velocity at x/D = 3.0 plane

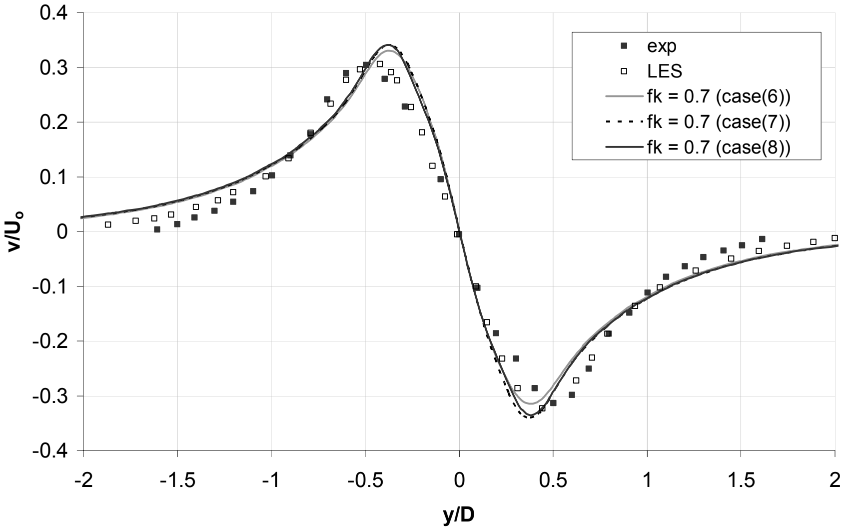

Figure 9: Grid resolution study for PANS cases with $f_k = 0.7$. Comparison of the mean normal velocity at x/D = 1.0 plane

5.3 TIME-STEP SENSITIVITY STUDY

This sub-section provides a study of the cylinder flow simulations performed at three different non-dimensional time steps (Δt^*) of 0.21, 0.105, and 0.0525. Cases (3), (4), and (5) were performed to study the time step convergence for $f_k = 0.7$ with the same reference grid. Cases (11), (12), and (13) were performed to study the time-step convergence test for $f_k = 0.5$ with the same reference grid.

Figure 10 gives comparison of the mean streamwise velocity along the wake centerline for the various PANS calculations with different time-steps and with f_k value of 0.7. From the plot we can observe that reducing the $\Delta t^*$from 0.21 to 0.105 the solution tends closer towards experimental results leading to better accuracy. A further reduction in the Δt^* to 0.0525 shifts the solution towards experimental results. But this improvement is very small compared to the addition computational expense. Figure 11 gives the comparison of the mean streamwise velocity along the wake centerline for PANS cases with $f_k = 0.5$ performed to study the effect of temporal resolution. As in the PANS case with $f_k = 0.7$, the accuracy of the results improve with decrease in the Δt^* from 0.21 to 0.105. Further decrease in the time-step from 0.105 to 0.0525 shifts the solution towards experimental results by less than 5%.

Figures 12 – 17 present the results from temporal resolution studies at various locations in the wake of the cylinder for PANS calculations with f_k values of 0.7 and 0.5. These plots clearly ascertain the monotonic behavior of improvement in the accuracy of the predicted results by decreasing the time-step. Also they imply that PANS results with Δt^* value of 0.0525 is reasonably adequate for both f_k cases.

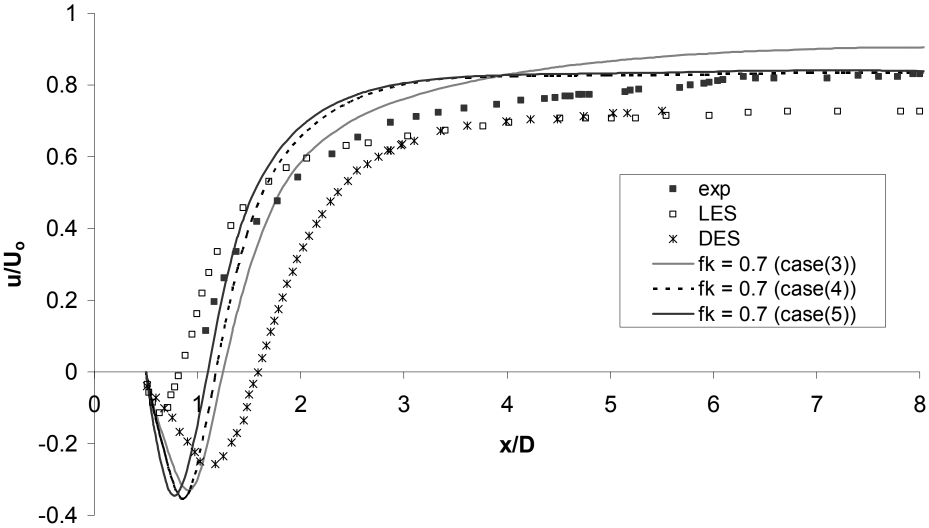

Figure 10: Time-step sensitivity study for PANS cases with f_k = 0.7. Comparison of the mean streamwise velocity at wake centerline

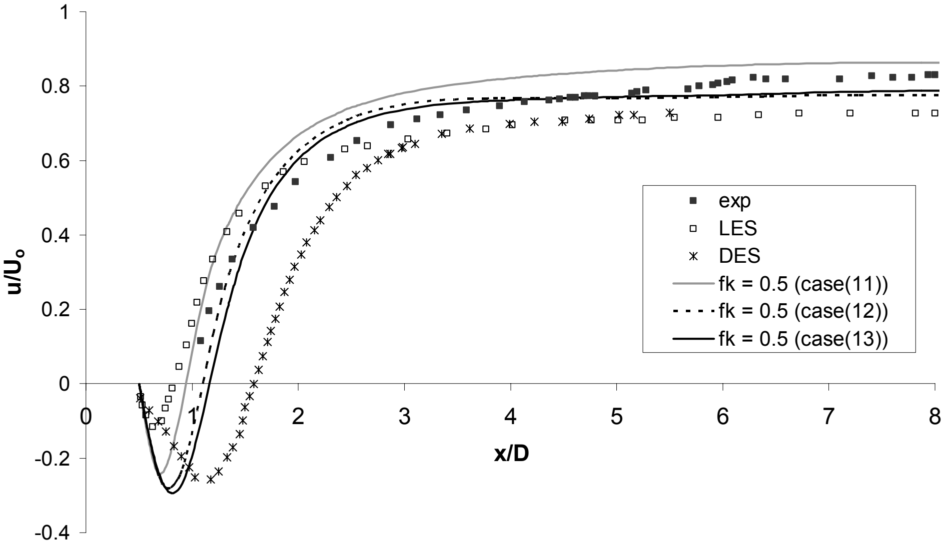

Figure 11: Time-step sensitivity study for PANS cases with f_k = 0.5. Comparison of the mean streamwise velocity at wake centerline

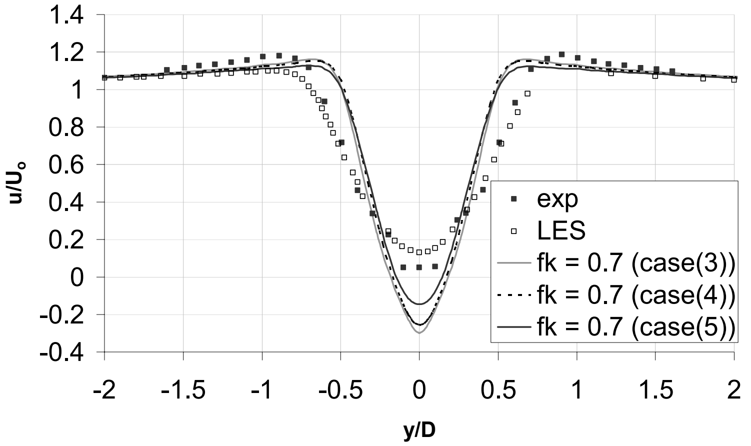

Figure 12: Time-step sensitivity study for PANS cases with f_k = 0.7. Comparison of the mean streamwise velocity at x/D = 1.0 plane

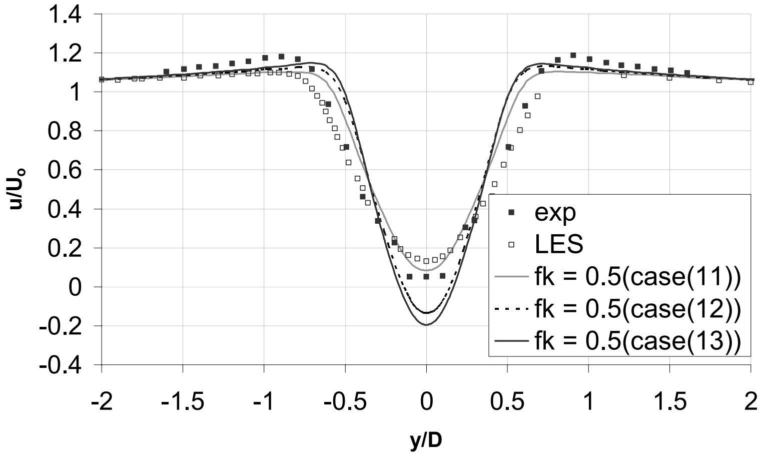

Figure 13: Time-step sensitivity study for PANS cases with f_k = 0.5. Comparison of the mean streamwise velocity at x/D = 1.0 plane

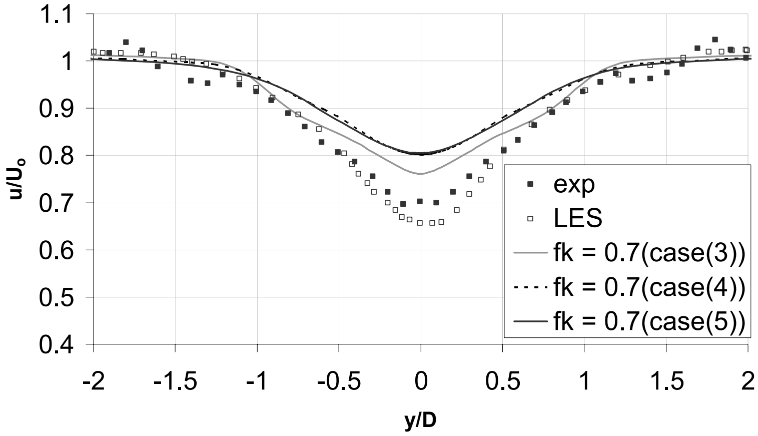

Figure 14: Time-step sensitivity study for PANS cases with f_k = 0.7. Comparison of the mean streamwise velocity at x/D = 3.0 plane

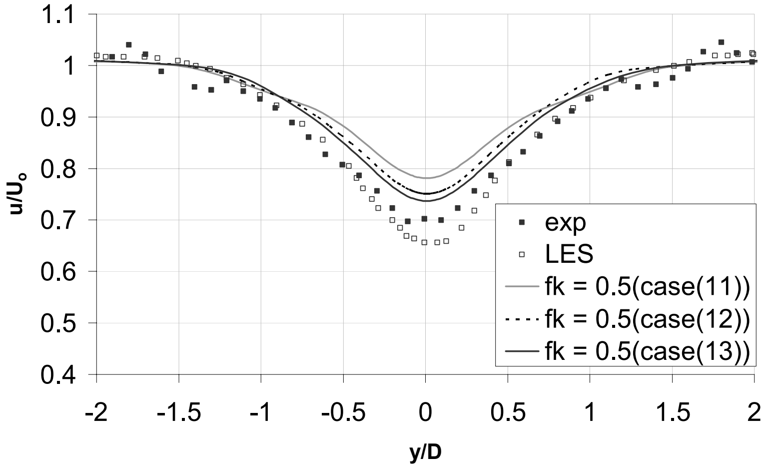

Figure 15: Time-step sensitivity study for PANS cases with f_k = 0.5. Comparison of the mean streamwise velocity at x/D = 3.0 plane

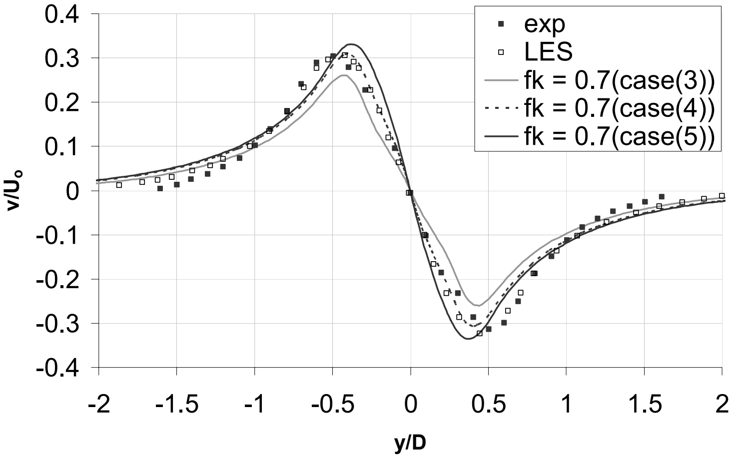

Figure 16: Time-step sensitivity study for PANS cases with f_k = 0.7. Comparison of the mean normal velocity at x/D = 1.0 plane

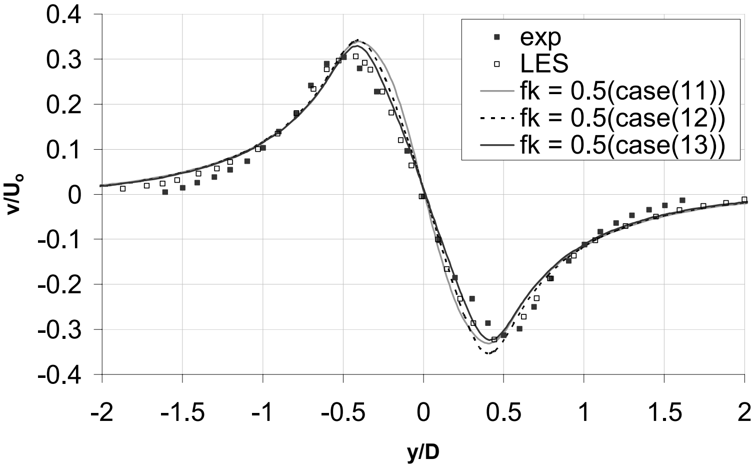

Figure 17: Time-step sensitivity study for PANS cases with f_k = 0.5. Comparison of the mean normal velocity at x/D = 1.0 plane

5.4 EFFECT OF f_ε VARIATION

Having established grid and temporal insensitivity of the PANS results, we perform further analysis of the PANS model by varying the various parameters of the model. One such study is the effect of varying the resolution control parameter f_ε such that $f_\varepsilon = f_k$. From the energy spectrum analysis of turbulent scales in appendix A, we know that for this high Reynolds number case the energy spectra is well defined with a non-overlapping energy and dissipation spectra meaning there is clear separation of scales.

A comparison study of PANS with $f_\varepsilon = 1$ and $f_\varepsilon = f_k$ was performed to better understand the performance of the PANS model for this high Reynolds number flow. Results from cases (3) and (9) are presented in this study. Both these cases were run with identical time-step and grid resolution and with an f_k value of 0.7. This provides for a direct comparison of the performance of the PANS model for the two cases.

Figure 18 gives the mean streamwise velocity along the wake centerline for the two cases compared. Results from other experimental studies and numerical studies are plotted for better comparison. We can observe that having $f_\varepsilon = 1$ for this high Reynolds number simulations give more accurate results. The case with f_ε varying as f_k predicts a much larger separation bubble leading to inaccuracies.

Figures 19, 20, and 21 give the mean velocity profiles at various planes in the wake region for the two PANS cases. Except for x/D = 3 profile, the case with $f_\varepsilon = 1$ predicts the flow statistics closer to the experimental results than the one with $f_\varepsilon = f_k$. From figures 18 - 21 we can clearly observe that fixing the resolution control parameter f_ε to unity provides more accurate results than varying it such that $f_\varepsilon = f_k$. This study merely acts as an *apriori* validation of the PANS model as it is well established from the Kolmogorov's hypothesis that for flows with high Reynolds number there is no overlapping of the energy spectra and the dissipation spectra. Hence placing the cut-off filter in the inertial sub-range of the energy spectrum no dissipation scales are resolved implying that $f_\varepsilon = 1$.

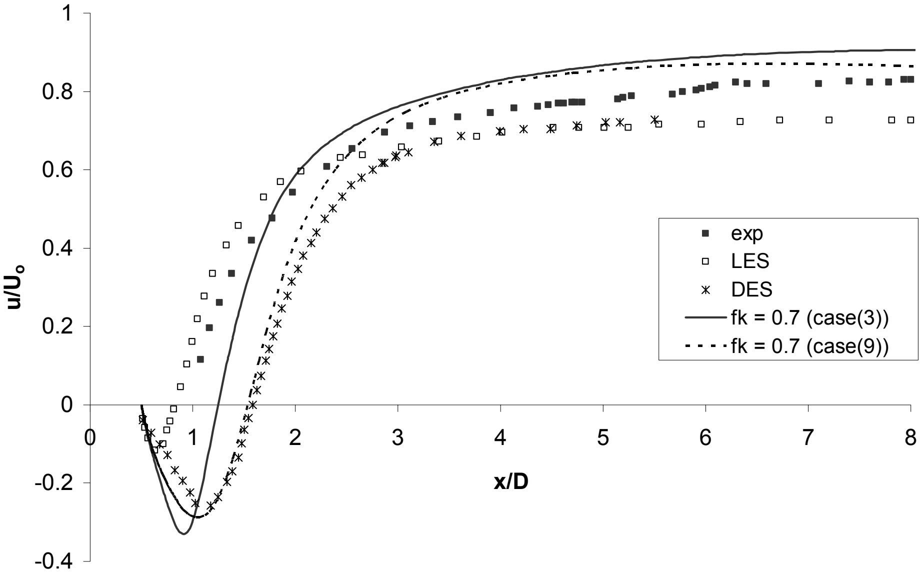

Figure 18: Effect of f_ε on PANS results. Comparison of the mean streamwise velocity at wake centerline

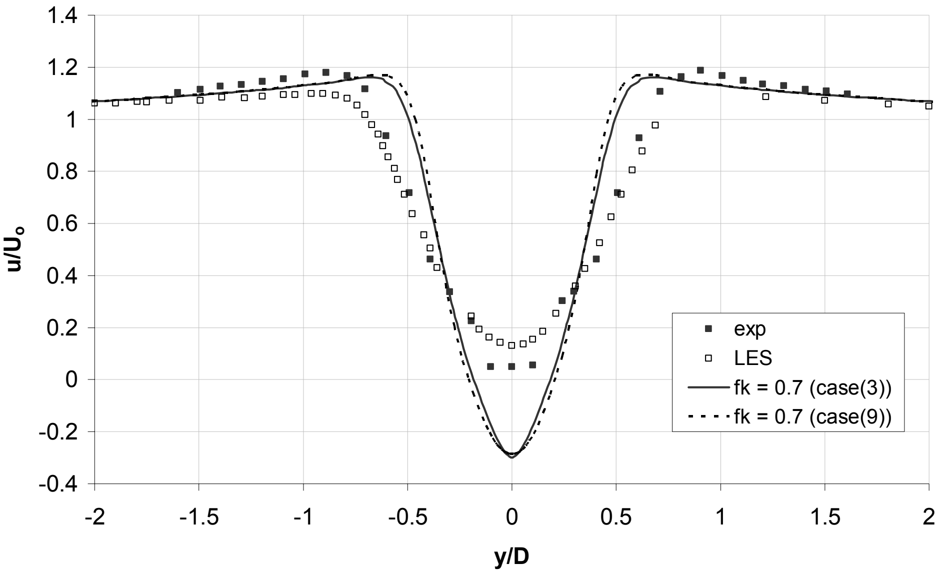

Figure 19: Effect of f_ε on PANS results. Comparison of the mean streamwise velocity at x/D = 1.0 plane

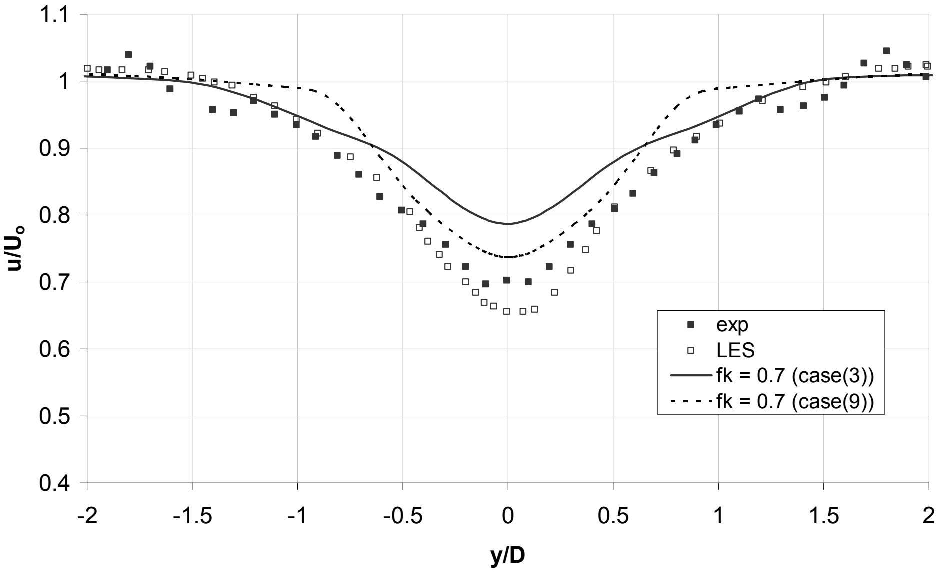

Figure 20: Effect of f_ε on PANS results. Comparison of the mean streamwise velocity at x/D = 3.0 plane

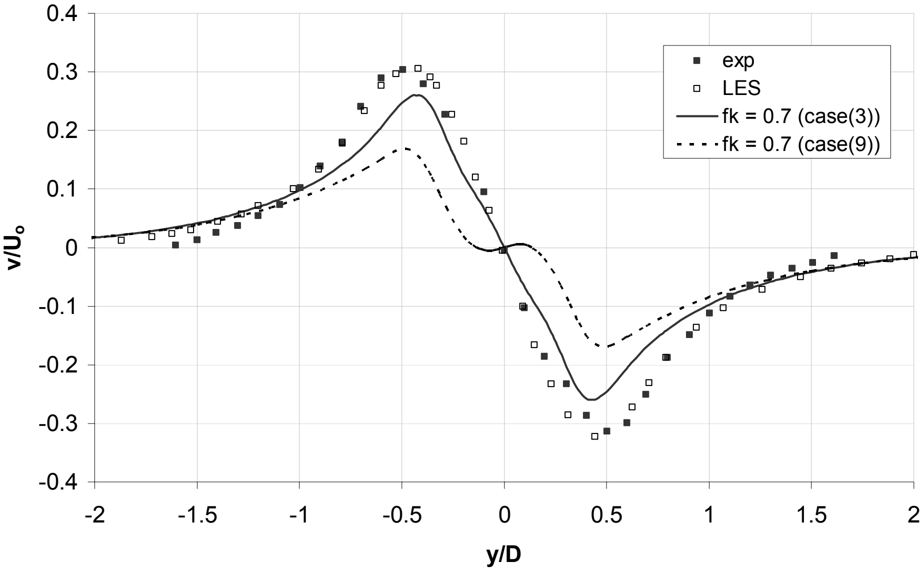

Figure 21: Effect of f_ε on PANS results. Comparison of the the mean normal velocity at x/D = 1.0 plane

5.5 EFFECT OF σ_{ku} VARIATION

Having analyzed the PANS results for variation of f_ε, we perform further analysis of the PANS model. One of the PANS model parameters whose variation is important to understand the performance of the model is the turbulent prandtl number σ_{ku}. From the PANS model equations we have the equation for the turbulent prandtl number of unresolved kinetic energy as $\sigma_{ku} = \sigma_k \times f_k^2 / f_\varepsilon$ where σ_k is the turbulent prandlt number for total kinetic energy as in the RANS method ($\sigma_k = 1$).

A comparison study was performed between specifying σ_{ku} as per PANS method and by fixing it to unity as in the RANS model. Results from Cases (3) and (10) are presented in this study of σ_{ku}. Both these results were run with the identical grid resolution and temporal resolution. Based on the results from the f_ε study, the resolution control parameters f_k and f_ε were fixed at 0.7 and 1.0 respectively.

Figure 22 gives a comparison of the two cases with σ_{ku} variation for the mean streamwise velocity along the wake centerline. Results from experimental studies and numerical studies are also plotted alongside to better understand the variation of these PANS cases with these studies. As in the f_ε study, the PANS case with σ_{ku} varying according to the PANS equations predicts the mean flow statistics in this plot with better accuracy to the PANS case with σ_{ku} varying according to the RANS method. Case (10) with $\sigma_{ku} = 1$ predicts a larger reattachment length compared to case (3) giving rise to greater discrepancies with the experimental results.

Figures 23 - 25 gives plots of velocity statistics at various planes in the wake region to further demonstrate the effects of varying σ_{ku} as per the PANS model and RANS model. It is fairly clear from these plots at various planes that varying the σ_{ku} as per the PANS model provides for improved accuracy; the reason being a considerably high Reynolds number flow such that there is a well defined process of energy cascading from production scales to dissipation scales.

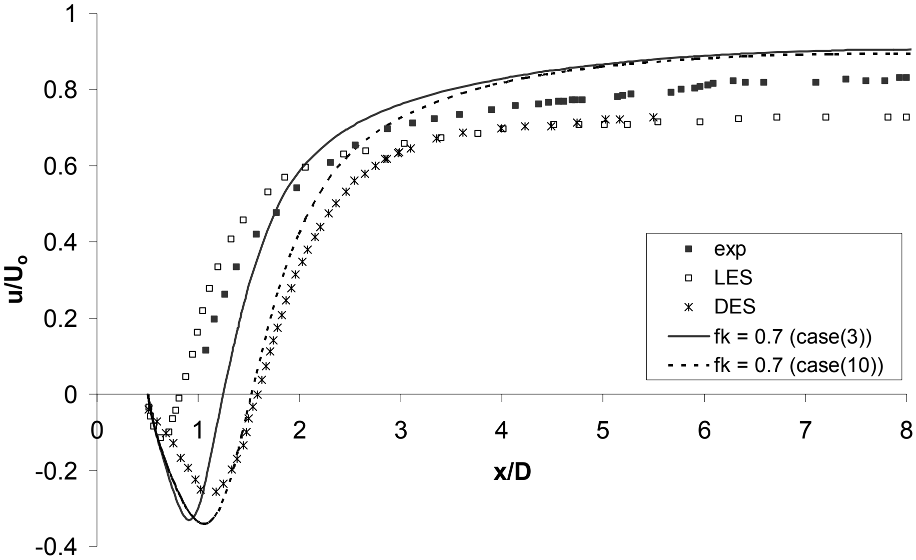

Figure 22: Effect of σ_{ku} on PANS results. Comparison of the mean streamwise velocity at wake centerline

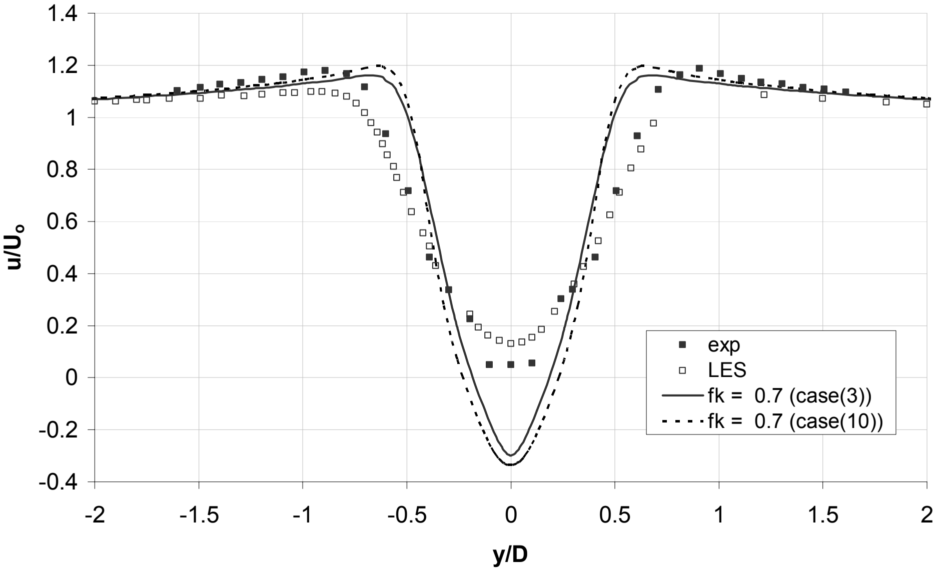

Figure 23: Effect of σ_{ku} on PANS results. Comparison of the mean streamwise velocity at x/D = 1.0 plane

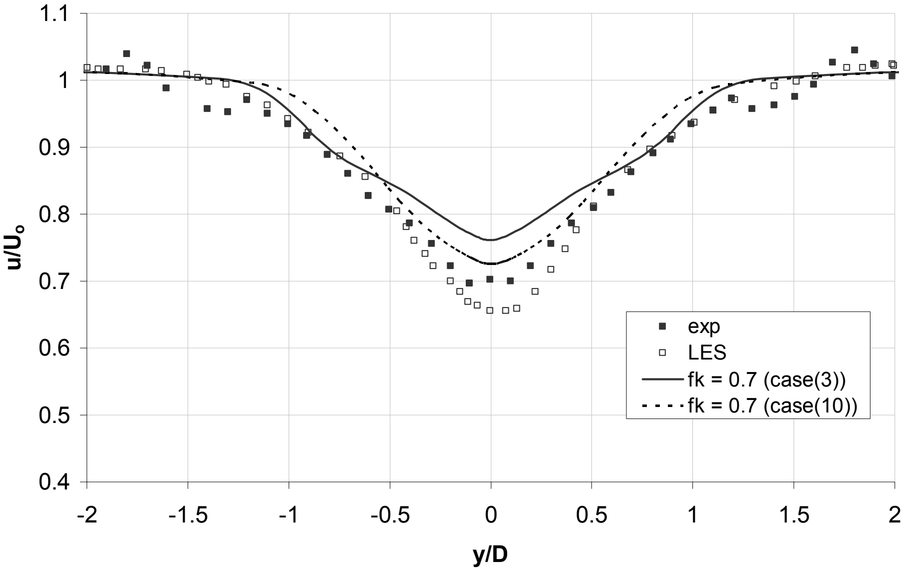

Figure 24: Effect of σ_{ku} on PANS results. Comparison of the mean streamwise velocity at x/D = 3.0 plane

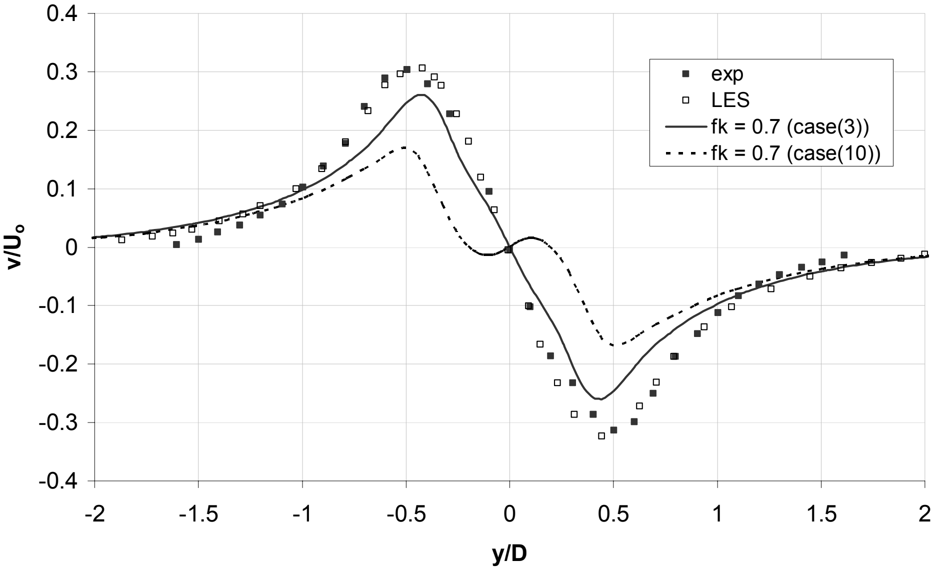

Figure 25: Effect of σ_{ku} on PANS results. Comparison of the mean normal velocity at x/D = 1.0 plane

5.6 INFLUENCE OF f_k ON FLOW STATISTICS

The preceding PANS calculations for flow past a circular cylinder at Re_D 140,000 provide us with an optimal setting for the PANS model parameters and permits for effectively studying the hybrid behavior of the PANS model. In the following paragraphs we study the PANS model capability to perform variable resolution simulations by varying the resolution control parameter f_k which could range from zero (corresponding to DNS type resolution) to one (corresponding to RANS type resolution). We study the PANS results for three values of f_k which are 1.0, 0.7 and 0.5. As *a posteriori* test for PANS model, the results from the PANS calculations are compared with available experimental and numerical results to study the effectiveness of the PANS to predict turbulent flow past a circular cylinder. The experimental results by Cantwell and Coles [5] along with numerical results from Breuer [4] and Travin et al. [24] are plotted alongside PANS results for comparison purposes.

According to Roshko [22], the laminar-turbulent transition in the boundary layer plays a determinant role in the vortex shedding flow around a circular cylinder. At moderately high Reynolds number ($Re_D < 2\times10^5$) the wall boundary layer experiences a laminar separation and gives rise to a rapid transition in the resulting mixing layer downstream of the separation point, followed by a turbulent wake. The shear layer vortices generated in this regime are expected to be three-dimensional structures.

5.6.1 Mean integral quantities

The mean integral results from PANS calculations are presented in table IV. The best resolved case for each f_k value is included. The shown quantities include the mean drag coefficient (C_d), the mean back pressure coefficient (C_{pb}), the mean separation angle (θ_s), and the Strouhal number (S_t). Experimental results, along with numerical results from DNS, LES and DES simulations are also presented.

Figure 5 gives C_d variation with time for PANS cases with f_k = 1.0 and 0.5. A clear harmonic trend with alternate sequence of high and low coherence instants is well reproduced by the numerical simulations. The computed mean C_d is under predicted by RANS simulations (C_d = 1.02). Since the periodic shedding motion is the main source of the momentum change in the flow over bluff body, non-physically big separation bubble in a standard RANS model simulation prevents mixing and leads to larger base pressure causing C_d value to be under-predicted. In PANS simulations the size of the separation bubble gets smaller and closer to the experimental results as f_k decreases. Hence the accuracy of predicted mean C_d increases with decrease in f_k value. The predicted mean C_d for PANS simulation with f_k = 0.5 is 1.37. This is comparable with the experimental results (1.237) and is very close to the LES results of Breuer (1.286) [4]. On the contrary, the LES simulations performed using Dynamic sub-grid scale model by Breuer predicts a value of 1.45 for C_d which is less accurate than the PANS predictions. This clearly illustrates the PANS model behavior of increased accuracy in predicting flow statistics with decreasing f_k values.

Table III: Mean integral quantities for Re_D 140,000

Case	Grid Resolution	Δt^*	C_d	C_{pb}	S_t	θ_{sep}
Experimental			1.237	-1.21	0.179	77
LES [26]	401 x 120 x 48	0.003	0.31	-0.32	0.28	
LES [4](B1)	325 x 325 x 64	2.00E-04	1.454	-1.764	0.204	95
LES [4](B2)	325 x 325 x 64	2.00E-04	1.286	-1.48	0.203	92.59
DES [24](LS8)	150 x 109 x 42		1.08	-1.04	0.21	77
PANS (f_k = 0.5)	150 x 135 x 42	0.0525	1.37	-0.8	0.26	95.86
PANS (f_k = 0.7)	150 x 135 x 42	0.0525	1.35	-0.769	0.26	99.77
PANS (f_k = 1.0)	85 x 85	0.21	1.02	-0.511	0.238	105

Changes in C_d are closely related to changes in $C_{pb,}$ the pressure coefficient at the back of the cylinder. As the dimensionless pressure in the back of the cylinder rises; the drag coefficient decreases. LES results from Breuer [4] over predict C_{pb} compared to the experimental results of Cantwell and Coles [5]. Again, the PANS accuracy in predicting the cylinder base pressure at the back of the cylinder improves by decreasing the f_k value from 1.0 to 0.5. Also an important observation is that PANS with $f_k = 0.5$ predicts the value of C_{pb} closer to the experimental results than LES and DES results.

Figure 26 gives a plot of distribution of pressure coefficient versus θ, the angle measured from the stagnation point. along the surface of the cylinder. The LES simulations presented in this plot are data obtained by Wang et al. [26]. The dimensionless pressure drop in the experimental results is not as much compared to the numerical results. The PANS calculations show monotonic improvement in predicting the C_p distribution with decrease in the f_k value. The PANS case with $f_k = 0.5$ is much closer to the experimental results compared to those with $f_k = 0.7$ and 1.0. Also they predict the C_p distribution with a better accuracy than LES results.

The separation angle, θ_s is the angle from the forward stagnation point at which the boundary layer separates giving rise to wake structures in the downstream of the cylinder flow. Wang et al. [25] defined the separation angle as the location where the pressure coefficient C_p has risen half way from $C_{p,min}$ to $C_{p,back}$. Also the location of the separation point can be found by plotting the wall shear stress on the cylinder surface. The point at which $\frac{\partial u}{\partial y} = 0$ is defined as the separation point.

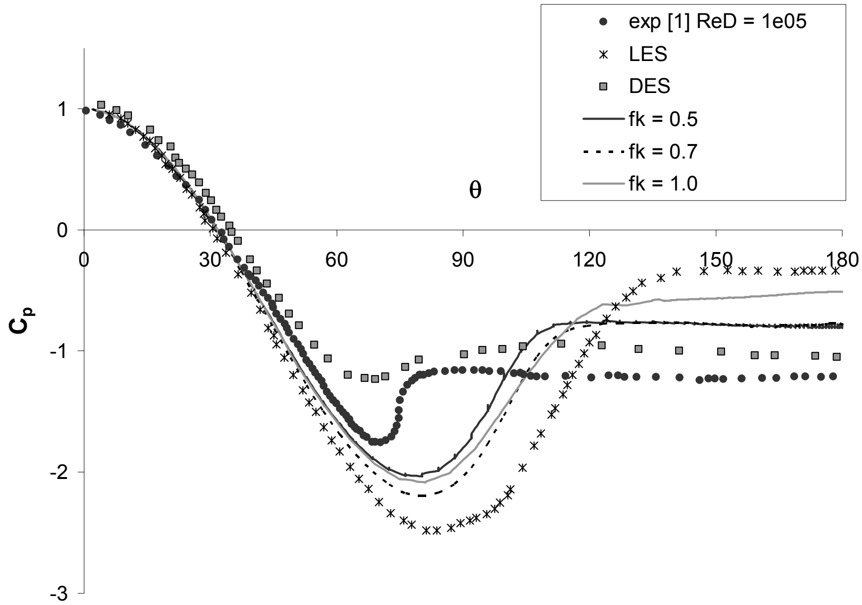

Figure 26: Coefficient of pressure distribution along the cylinder surface for various f_k values

For this Reynolds number of flow, the boundary layer is laminar at separation and experimental results predict the boundary layer to separate at $\theta = 78^o$ before reaching the main cross section. Experimental studies performed by Achenbach [1] focused on the position of the separation point and its variation as a function of the Reynolds number of the flow. He concluded that an increase in the Reynolds number from sub-critical to super-critical caused the separation angle to shift from to $\theta_s = 78^o$ to $\theta_s = 120^{o.}$ The variation of the separation angle shows a highly non-linear relationship between the Reynolds number and the separation angle. In the sub-critical range the lowest value of $\theta_s = 72^o$ has been measured. Numerical prediction of the separation angle is highly influenced by the spanwise grid elongation and resolution in the cross-sectional plane. Breuer [4] predicted a value of 95^o for θ_s indicating that the separation point is behind the apex of the cylinder contradicting experimental results. He attributed this discrepancy to extremely thin boundary layer at the cylinder. Travin et al. [24] studied the cylinder flow problem with both laminar separation and turbulent separation in their DES simulations by varying the initial condition with regard to the eddy viscosity. Their prediction of θ_s (=77^o) for laminar separation matched the experimental results. With turbulent separation, their predicted θ_s was 99^o. In the PANS simulations, the lowest value recorded for θ_s is 95.86^o corresponding to case (14) with f_k = 0.5. This is equal to the LES results. All of the PANS simulations performed over-predict the dimensionless pressure on the cylinder surface, hence leading to a delayed separation. For RANS (f_k = 1.0), θ_s is predicted to be 105^o. Decreasing the f_k value increases the accuracy of θ_s. It has been found that by suitably modifying the inflow conditions and appropriately tripping the flow can yield a better agreement with experimental data. However, these strategies require *a priori* knowledge of the separation angle. We do not attempt these *ad-hoc* manipulations but rather focus on the true predictive capability of PANS.

The strouhal number, S_t which arises due to harmonic vortex shedding effect of cylindrical structures gives the vortex shedding frequency and is defined as fD/U_0. Roshko [22] studied the strouhal number as a function of the Reynolds number. The typical value of S_t for sub-critical regime is about 0.2 Cantwell and Coles [5] found an extremely low Strouhal number St = 0.179 which, however is not in good agreement with most of the other experimentally determined S_t values. LES results from Breuer [4] predict a value of 0.203 which is a generally well accepted value for S_t. DES results from Travin et al. [24] predict a value of 0.21 for S_t. In our PANS calculations, the Strouhal number is extracted from the instantaneous lift coefficient (C_L) time series. The PANS cases predict a higher value for S_t ranging from 0.238 to 0.26 as reported in Table IV.

Due to the cancellation of errors, the integral quantities sometimes do not lead to a clear indication of the accuracy of a simulation. It is more informative to look at the profiles and distributions.

5.6.2 Mean flow and turbulence statistics

The mean flow field and the turbulence quantities are compared with existing results from experiment conducted by Cantwell & Coles [5], LES results of Breuer [4], and DES results of Travin et al. [24].

First, the mean streamwise velocity along wake centerline (y = 0) of the cylinder is considered. Figure 27 shows the normalized streamwise velocity (u/U_o) for PANS calculations with various f_k values plotted alongside the experimental and other numerical results.

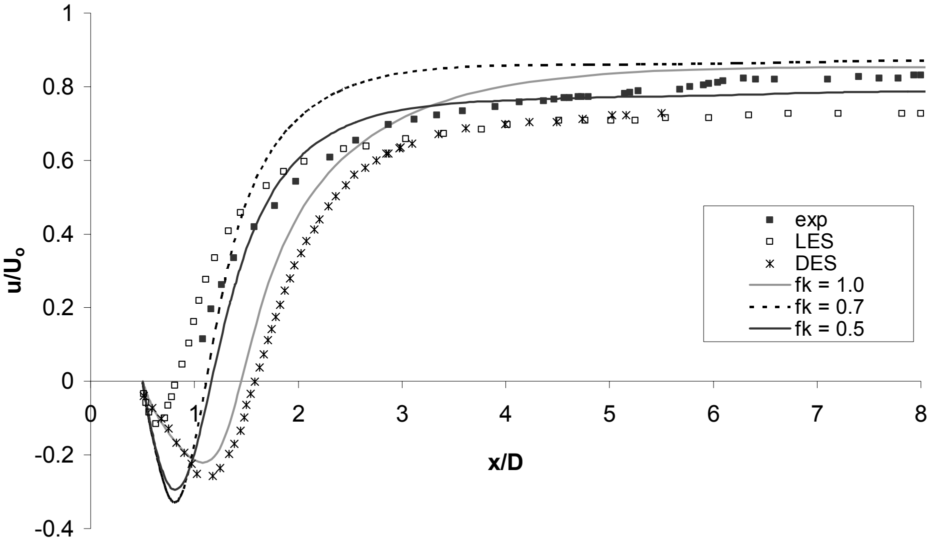

Figure 27: Effect of f_k variation. Comparison of the mean streamwise velocity along the wake centerline

The PANS calculations with $f_k = 1.0$ which is basically unsteady RANS case due to the inadequacies of the RANS model yields laminar-like shedding motion with over-prediction of the recirculation length. With PANS calculations ($f_k = 0.7$ and 0.5), the recirculation length gets smaller and closer to the experimental results. The convergence of PANS results to experimental data is not monotonic with reduction in f_k. There is no theoretical reason that this approach should be monotonic at large f_k values. The lack of a monotonic behavior reflects the gross inaccuracy of URANS (f_k = 1) equations. However, it is clear that at smaller f_k values the PANS results do approach experimental data.

LES results from Breuer [4] predict a very small separation bubble and are less accurate than the PANS cases. DES results from Travin et al. [24] for this case predict the recirculation length greater than RANS case. The PANS results provide better agreement with the experimental results compared to LES and DES results. PANS with f_k = 0.7 and f_k = 0.5 show fairly same behavior close to the cylinder ($x/D \leq 1$). Further away from the cylinder, PANS with f_k = 0.7 predicts a higher value for the mean streamwise velocity whereas PANS with f_k = 0.5 continues to show very good agreement with the experimental results.

Figure 28 shows the time-averaged streamwise velocity in the near wake along x/D = 1 plane. The PANS results predict a narrow velocity profile compared to the experimental and LES results. PANS cases with $f_k < 1$ show better agreement with the experimental results compared to PANS with f_k = 1 (RANS). In the $-0.5 < y/D < 0.5$ region, PANS result with f_k = 0.7 predicts slightly better results than PANS with f_k = 0.5. However in other regions of the plot, f_k = 0.5 agrees better with the experimental results than other PANS cases.

Figure 29 gives the mean normal velocity on x/D = 1.0 plane. Both the PANS results with f_k = 0.7 and f_k = 0.5 predict the mean normal velocity at x/D = 1.0 plane with good accuracy. Of these two cases, PANS with f_k = 0.5 shows very good agreement with the experimental results even better than PANS with f_k = 0.7. The PANS case with f_k = 1.0 (RANS) predicts a very low V-velocity profile and completely fails to capture the profile of this velocity statistics.

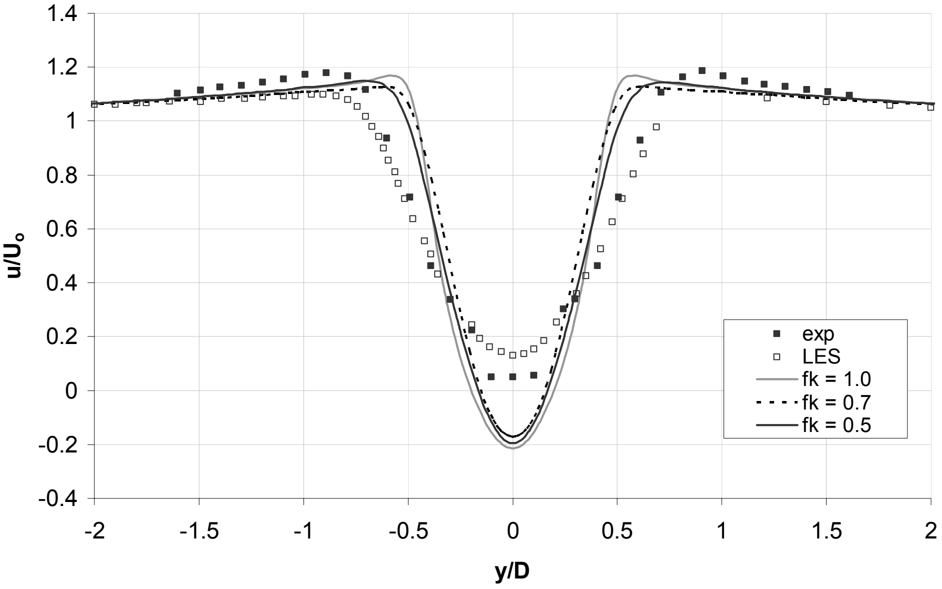

Figure 28: Effect of *f*$_k$ variation. Comparison of the mean streamwise velocity at x/D = 1.0 plane

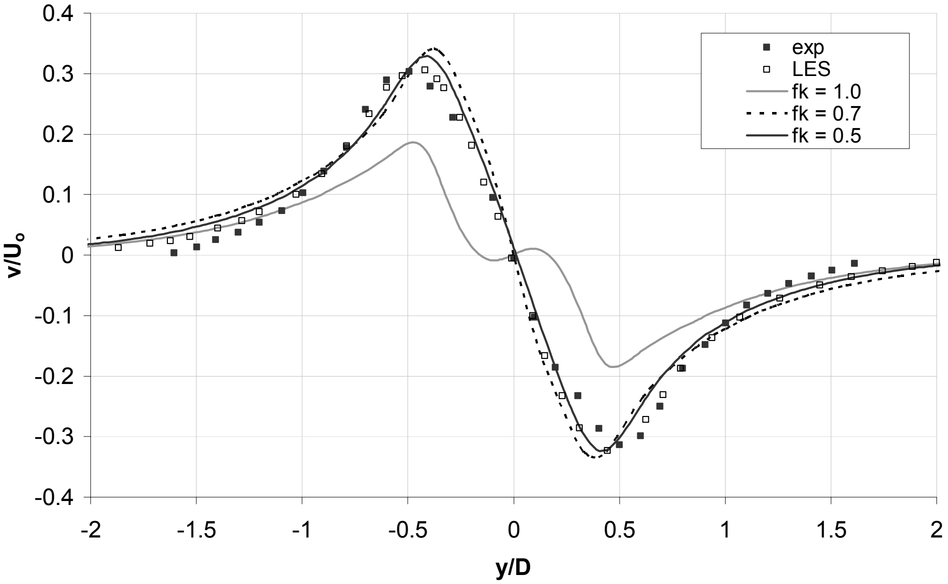

Figure 29: Effect of *f*$_k$ variation. Comparison of the mean normal velocity at x/D = 1.0 plane

Figure 30 gives the mean streamwise velocity statistics for PANS results with various f_k values along the wake centerline further downstream of the cylinder (x/D = 3.0). For this case, the PANS results with $f_k = 1.0$ (RANS) show better agreement with the experimental results in the region $-0.5 < y/D < 0.5$. However, further away from the center, the PANS with $f_k = 0.5$ is more accurate than the RANS case.

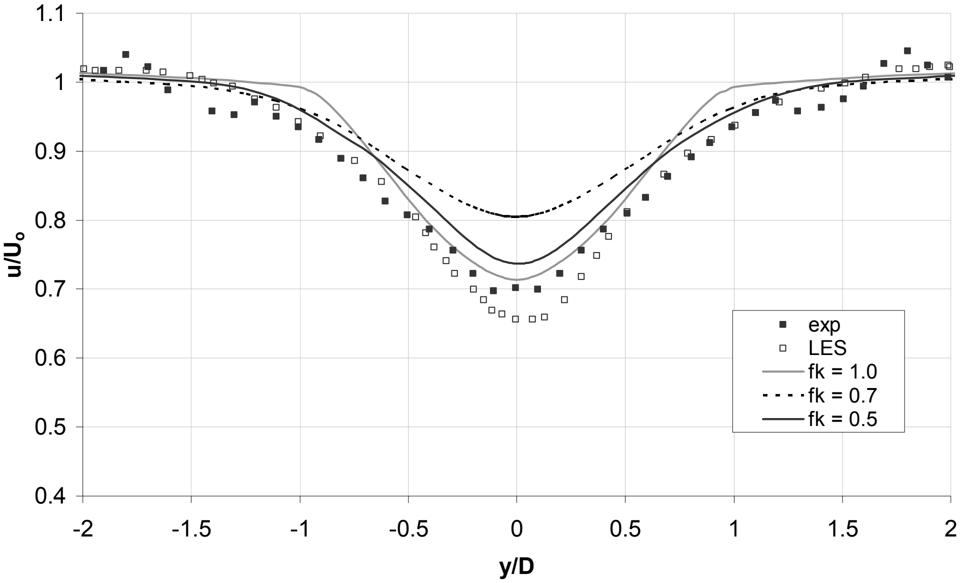

Figure 30: Effect of f_k variation. Comparison of the mean streamwise velocity at x/D = 3.0 plane

In general, PANS results show good agreement with the compared experimental results. In some statistics they are more accurate than the LES results compared. Also decreasing the f_k value tends to improve the accuracy of the solution bringing the PANS results closer to the experimental results.

Figures 31 – 52 presents qualitative comparison between PANS computations of various physical resolutions. Instantaneous contours of various quantities are plotted on different planes to visualize the wake structures for these cases. Figures 31 - 33 give the instantaneous velocity contours for various f_k values. The RANS results show smooth structures with a large separation bubble. Decreasing f_k value decreases the size of the bubble. Figures 34 - 36 show the instantaneous contours of vorticity magnitude for various f_k values. It can be seen that in the case of RANS simulations the complex near wake vorticity structures are smoothened forming a well-defined laminar-flow type vortices. This results in an unrealistically large separation bubble. Very little vorticity is seen outside the main vortex locations. However as f_k decreases, the size of separation bubble reduce and more details of the flow structure are captured. Hence as f_k is reduced, the amount of resolved vortical structures increases. Also, separation between the vortices and background flow is much sharper indicating smaller effective viscosity. This clearly demonstrates the fact that PANS method can smoothly bridge the range between RANS and DNS.

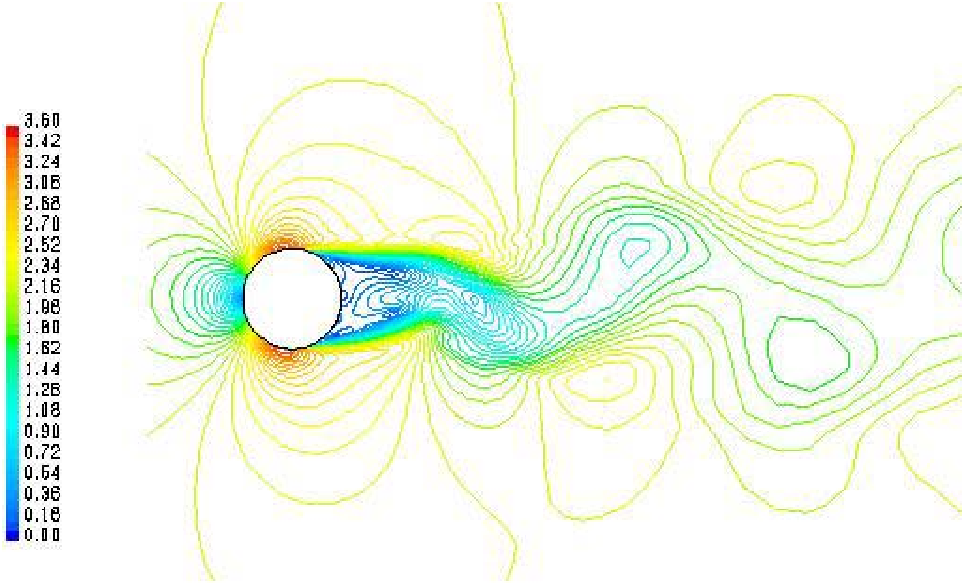

Figure 31: Instantaneous contours of velocity magnitude for f_k = 1.0 along z/D = 1.0 plane

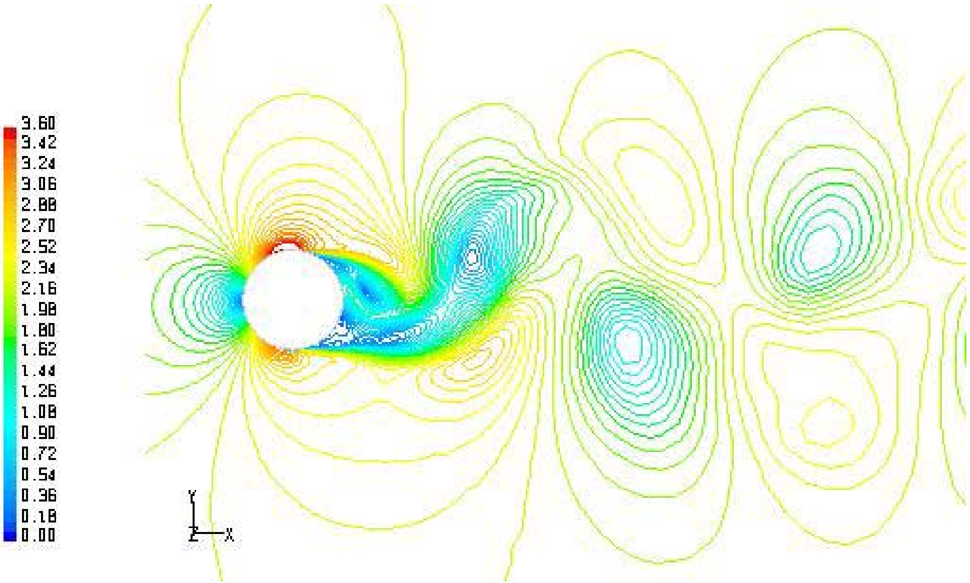

Figure 32: Instantaneous contours of velocity magnitude for f_k = 0.7 along z/D = 1.0 plane

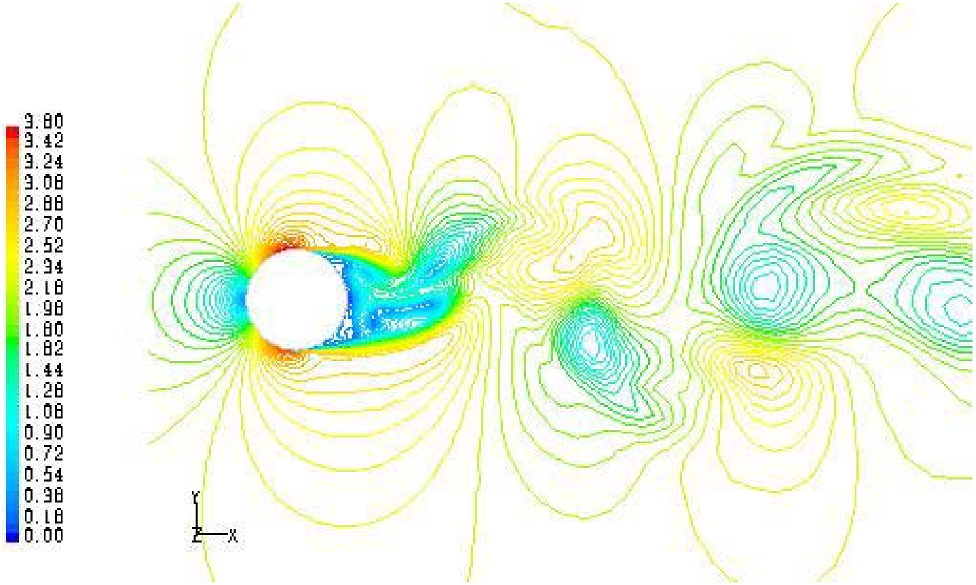

Figure 33: Instantaneous contours of velocity magnitude for f_k = 0.5 along z/D = 1.0 plane

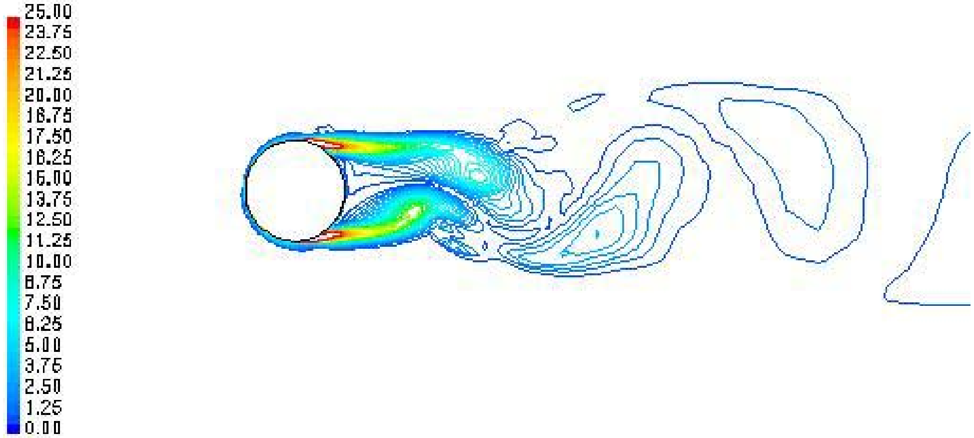

Figure 34: Instantaneous contours of vorticity magnitude for f_k = 1.0 along z/D = 1.0 plane

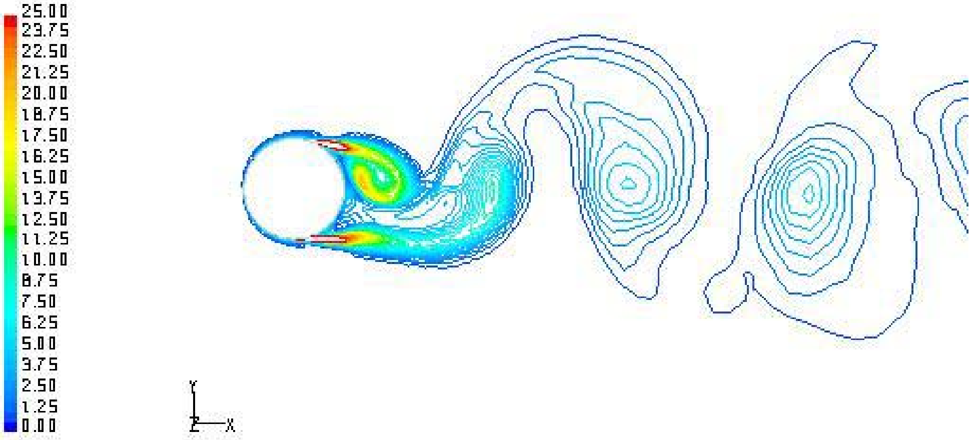

Figure 35: Instantaneous contours of vorticity magnitude for f_k = 0.7 along z/D = 1.0 plane

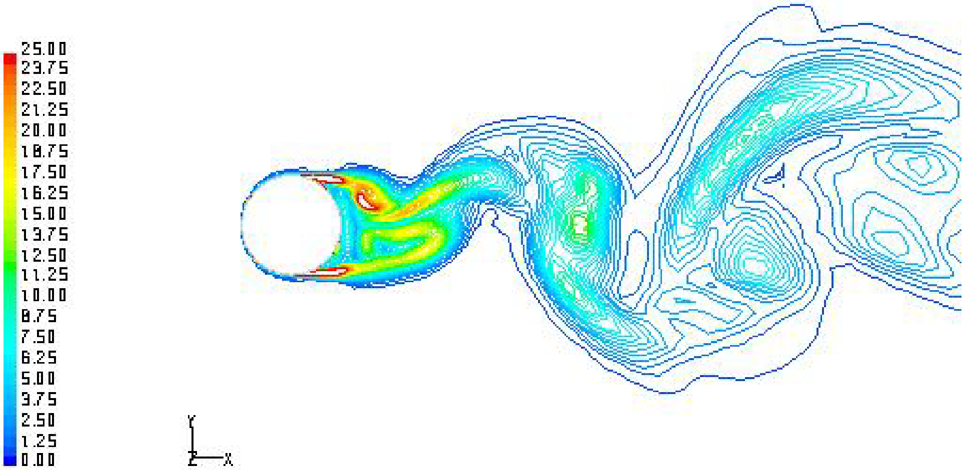

Figure 36: Instantaneous contours of vorticity magnitude for f_k = 0.5 along z/D = 1.0 plane

Figures 37 – 39 give the instantaneous contours of unresolved kinetic energy for various f_k values. As required by the model, by reducing f_k value, we are resolving more kinetic energy content of the flow. As a result the unresolved kinetic energy decreases by decreasing the f_k value from 1.0 to 0.5. This phenomenon is clearly observed in these contour plots for various f_k values. Figures 40 - 42 give the unresolved eddy viscosity for various f_k values. These contours confirm that resolving more structures, we reduce the effective viscosity and hence more accurate prediction of the flow statistics.

Figures 43 - 52 give various contour plots including three dimensional contour plots for comparison between PANS simulation of $f_k = 0.7$ and $f_k = 0.5$. These figures clearly indicate that moving from $f_k = 0.7$ to 0.5, more number of vortical structures are resolved, sharper vortices are observed and hence better visualization of the complexity of the flow structures in the wake. Figures 47 - 52 clearly indicate the necessity to perform three dimensional computations. These contour plots capture the effects of three-dimensionality of the vorticity structures in the wake region. Note that RANS cannot perform three-dimensional analysis as there is no production for z-directional fluctuation and furthermore, there is no mean motion in spanwise direction.

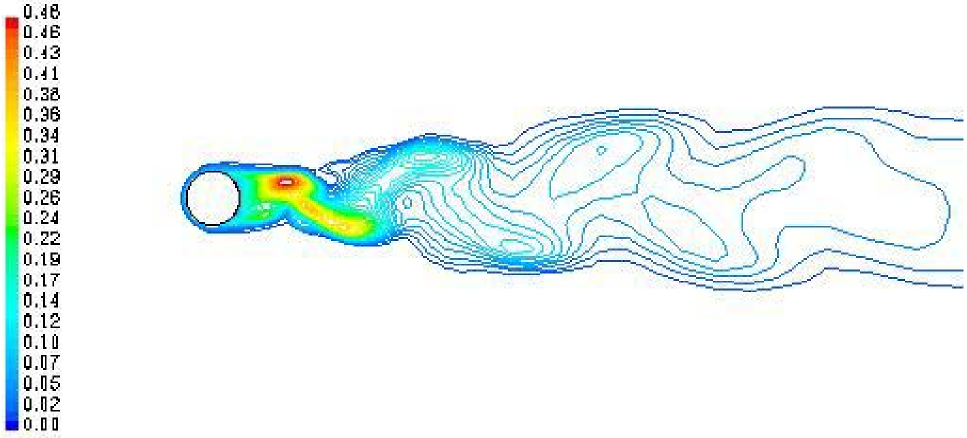

Figure 37: Contours of unresolved kinetic energy for *f*$_k$ = 1.0 along z/D = 1.0 plane

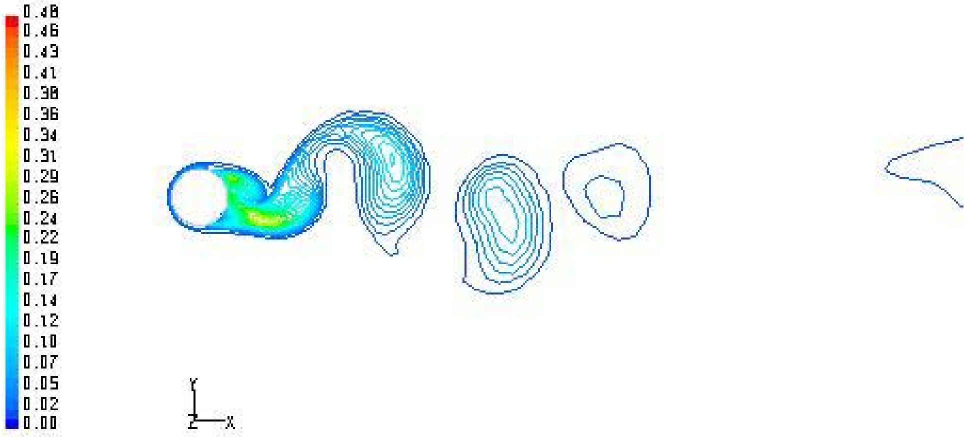

Figure 38: Contours of unresolved kinetic energy for *f*$_k$ = 0.7 along z/D = 1.0 plane

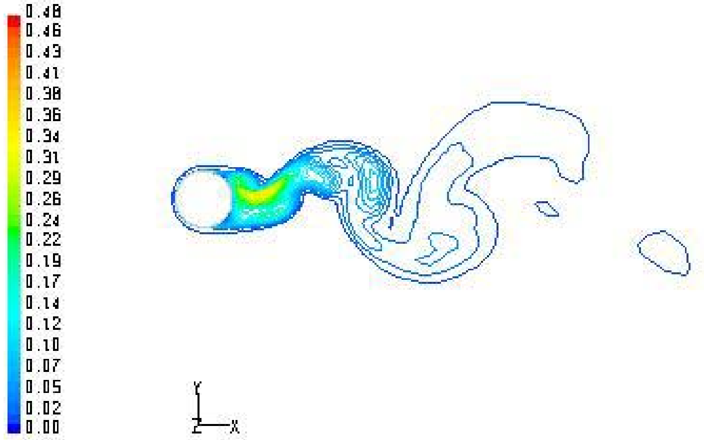

Figure 39: Contours of unresolved kinetic energy for f_k = 0.5 along z/D = 1.0 plane

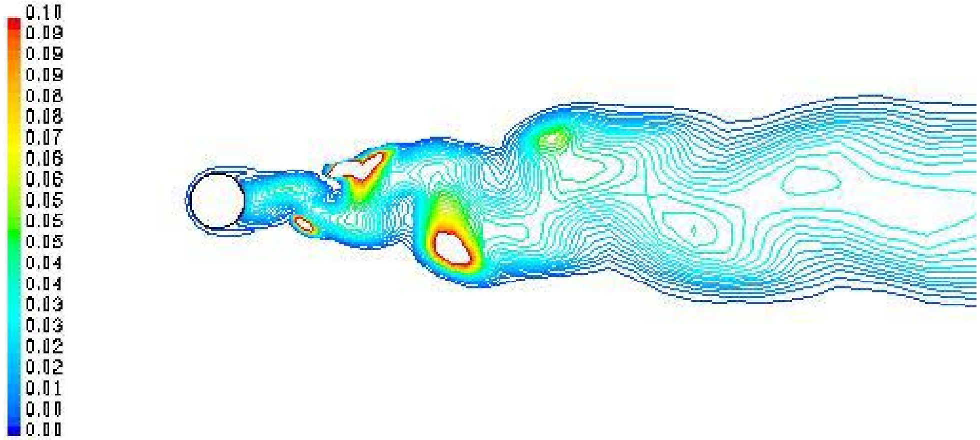

Figure 40: Contours of unresolved eddy viscosity for f_k = 1.0 along z/D = 1.0 plane

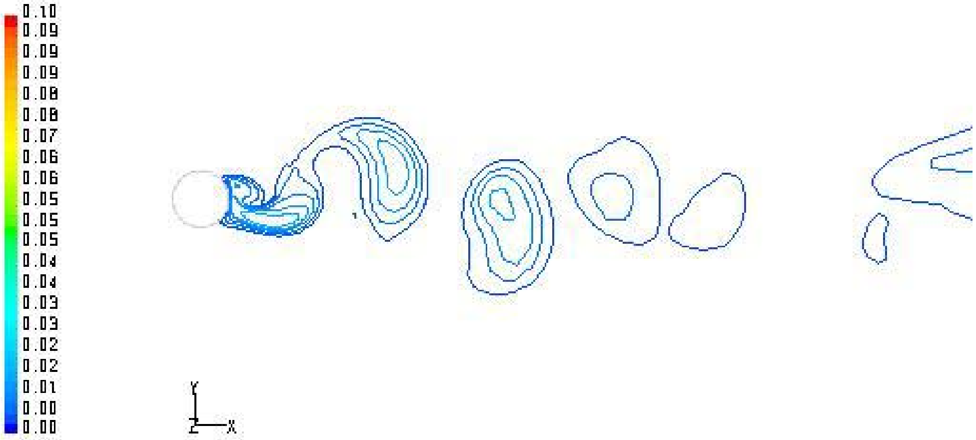

Figure 41: Contours of unresolved eddy viscosity for $f_k = 0.7$ along z/D = 1.0 plane

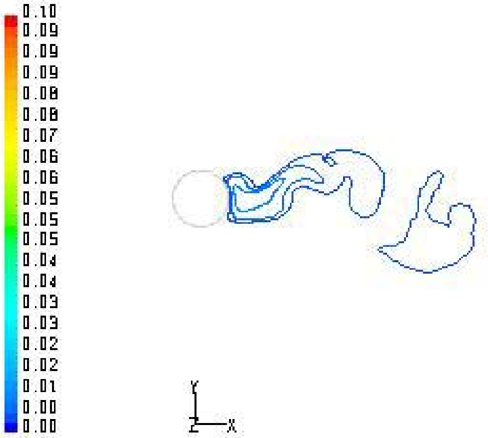

Figure 42: Contours of unresolved eddy viscosity for $f_k = 0.5$ along z/D = 1.0 plane

Figure 43: Instantaneous contours of x-vorticity for *f*$_k$ = 0.7

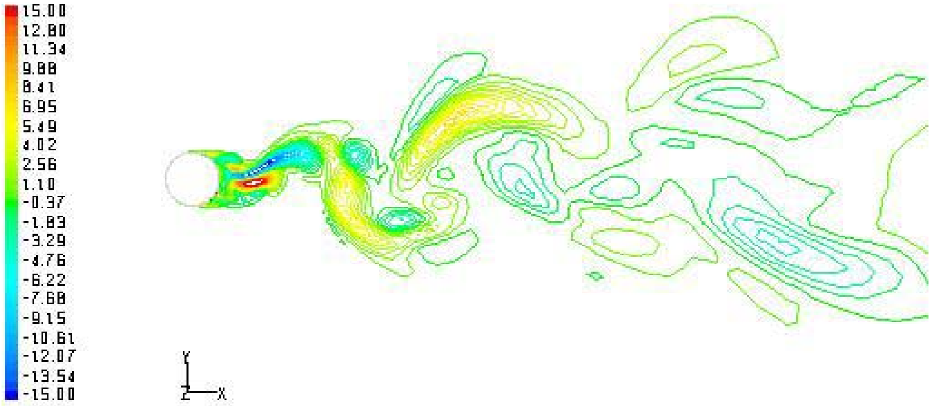

Figure 44: Instantaneous contours of x-vorticity for *f*$_k$ = 0.5

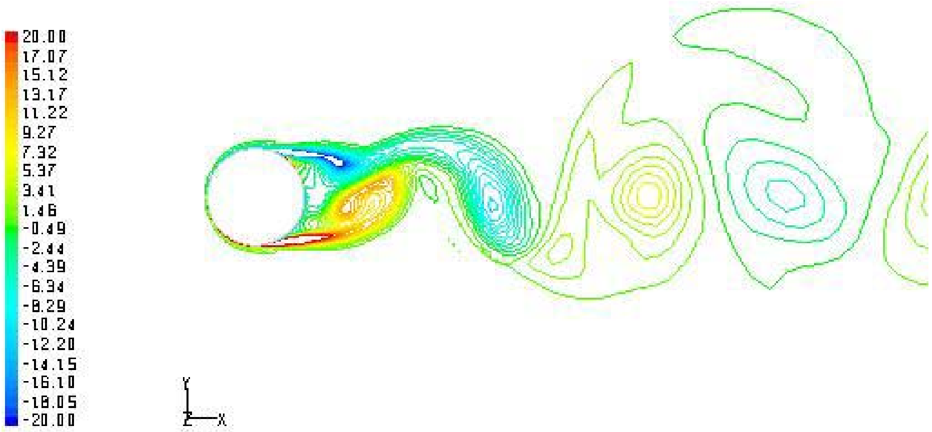

Figure 45: Instantaneous contours of z-vorticity for $f_k = 0.7$

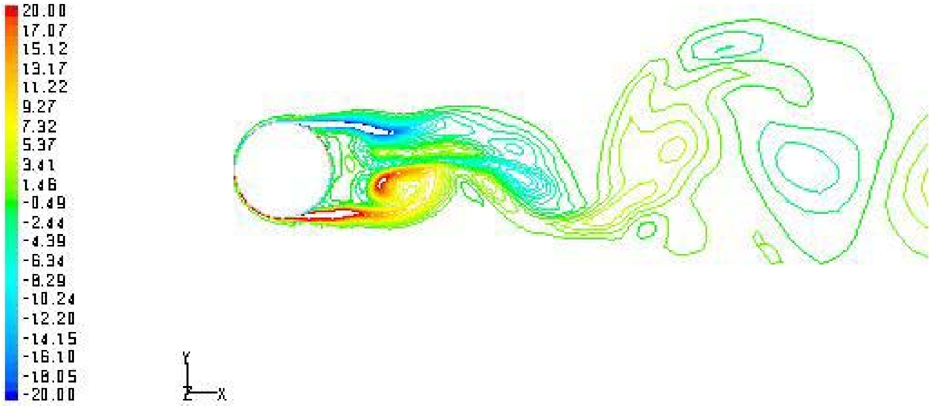

Figure 46: Instantaneous contours of z-vorticity for $f_k = 0.5$

Figure 47: Iso-vorticity contours (|ω| = 0.5,1, 1.5, 2, 2.5, 3, and 5) in the wake region for f_k = 0.7

Figure 48: Iso-vorticity contours (|ω| = 0.5,1, 1.5, 2, 2.5, 3, and 5) in the wake region for f_k = 0.5

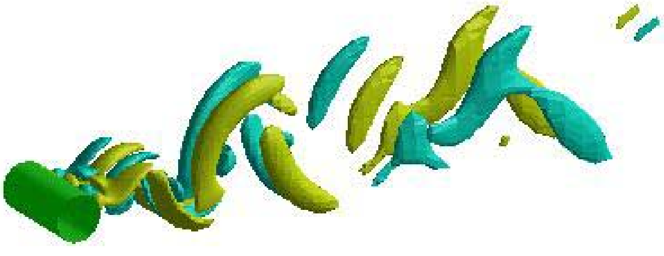

Figure 49: Contours of iso y-vorticity (ω_y= 0.5, -0.5) for f_k = 0.7

Figure 50: Contours of iso y-vorticity (ω_y= 0.5, -0.5) for f_k = 0.5

Figure 51: Contours of iso x-vorticity (ω_x= 1.0, -1.0) for f_k = 0.7

Figure 52: Contours of iso x-vorticity (ω_x= 1.0, -1.0) for f_k = 0.5

6. RESULTS AND DISCUSSION FOR Re_D 3900

6.1 INTRODUCTION

Flow past a cylinder at Re_D 3900 based on the free-stream velocity is also studied to validate the PANS methodology. At this Reynolds number, which is low for most of the technical applications, the flow is still complex as indicated by Tremblay et al. [25] in their DNS simulations. The case of cylinder flow at Re_D 3900 is the most popular test case among flow past bluff body simulations and comprehensive data from experimental studies, DNS simulations, and LES simulations are available for comparison studies. At this Reynolds number, as in the case with Re_D 140,000 the flow is characterized by laminar separation, transition to turbulence in the free shear layers leaving the body and shedding of large scale vortices. Several PANS calculations were performed to study the PANS method effectively. Table I gives the list of all the cases performed for the PANS calculations of this Re_D.

The Reynolds number of the flow being small in engineering context, we focus on varying the PANS model parameters to accurately predict the flow behavior and hence demonstrate the flexibility of the model to adapt its parameters to accommodate for PANS modeling capability in a wide range of engineering flows. In this context we study:

1. Effect of f_ε variation
2. Effect of σ_{ku} variation
3. Effect of f_k variation

As in the case of Re_D 140000, the simulations were performed for a total flow time of 300D/U∞ time units. Initial flow data corresponding to about 120D/U∞ is discarded. This is to allow for any transitions in the flow to settle down and to establish a statically steady vortex shedding. For cases where there is large fluctuations ($f_k = 0.5$) more time was allowed for the flow to settle down and the statistics were compiled over a larger flow time. After each flow is fully developed, the data are gathered to calculate flow statistics.

6.2 EFFECT OF f_ε VARIATION

Having studied the PANS results for various f_k values and with $f_\varepsilon = 1$ we observe that they show very poor agreement with the available experimental and numerical data. On the contrary, the RANS ($f_k = 1.0$) calculations predict the flow statistics more accurately for this low Reynolds number case. Based on the discussion in appendix A further PANS calculations for various f_k values and with varying f_ε values such that $f_\varepsilon = f_k$ are studied. In the following paragraphs we discuss the results from cases (3) and (9) which study f_ε variation for f_k value of 0.7. Also results from cases (8) and (12) with f_k value of 0.5 are discussed in this study.

Figure 53 gives the mean x-velocity along the wake centerline for two PANS calculations with $f_k = 0.7$. Comparisons between the two cases reveal that varying f_ε in accordance with f_k instead of having it fixed at unity increases the accuracy of the solution. Figure 54 gives the mean stream-wise velocity along the wake centerline for PANS calculations with $f_k = 0.5$. The figure gives a comparison study between PANS cases, one with a fixed value for f_ε (= 1) and the other with f_ε varying such that $f_\varepsilon = f_k$. Results from other numerical studies are also plotted for comparison. From figures 53 and 54, we can clearly conclude that the PANS calculations with $f_\varepsilon = f_k$ predicts the flow more accurately than having f_ε fixed at unity. Also, these PANS calculations agree much better with the experimental results than LES calculations of Breuer [3].

Figures 55 - 62 give the mean velocity statistics at various planes in the near wake region of the cylinder flow for the above discussed cases. These figures ascertain the advantages of having $f_\varepsilon = f_k$ for this low Reynolds number PANS modeling of turbulent flow past a circular cylinder. At all regions of flow in the wake region, PANS calculations with both the turbulent scales and the dissipation scales resolved perform more accurately than PANS with all the dissipation scales being modeled.

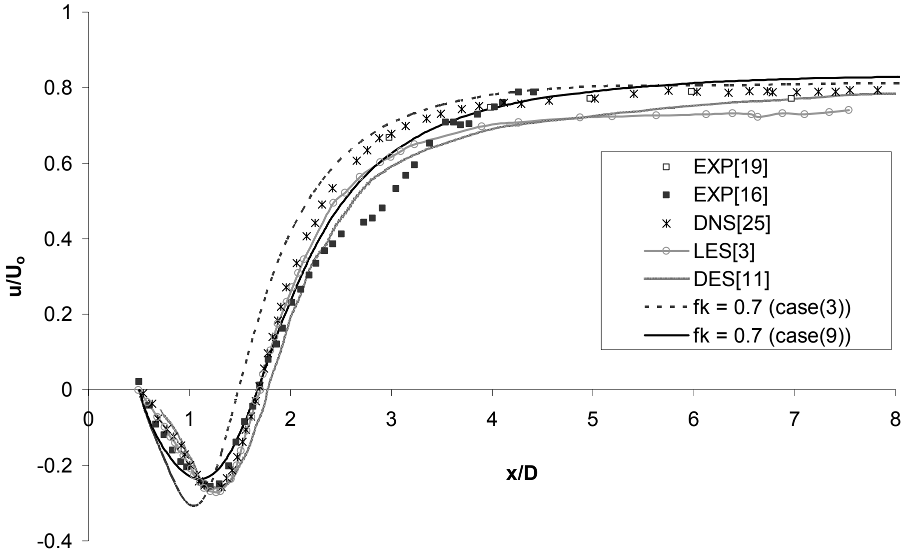

Figure 53: Effect of f_ε on PANS results. Comparison of the mean streamwise velocity at wake centerline for f_k = 0.7

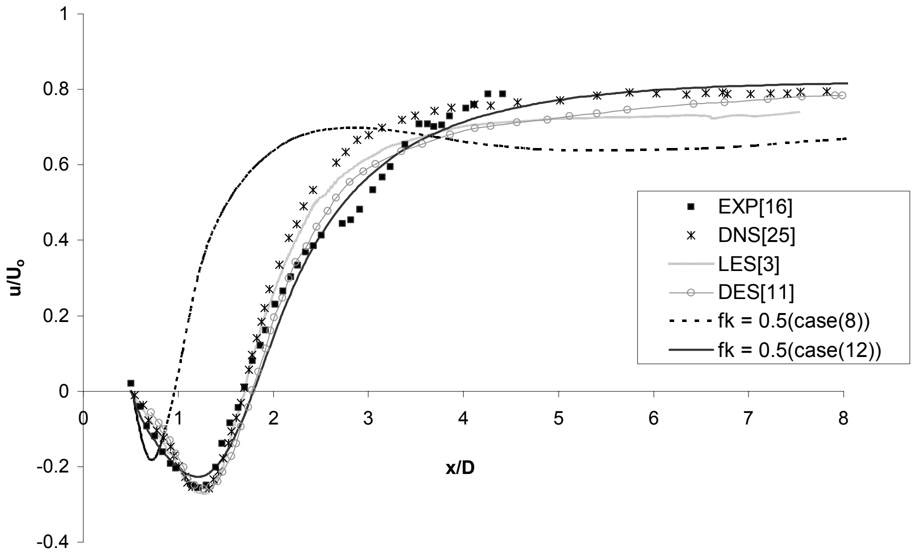

Figure 54: Effect of f_ε on PANS results. Comparison of the mean streamwise velocity at wake centerline for f_k = 0.5

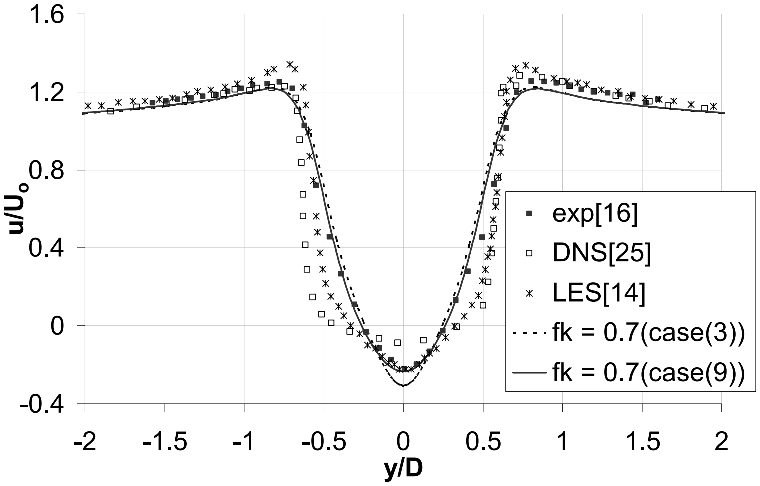

Figure 55: Effect of f_ε on PANS results. Comparison of the mean streamwise velocity at x/D = 1.06 for f_k = 0.7

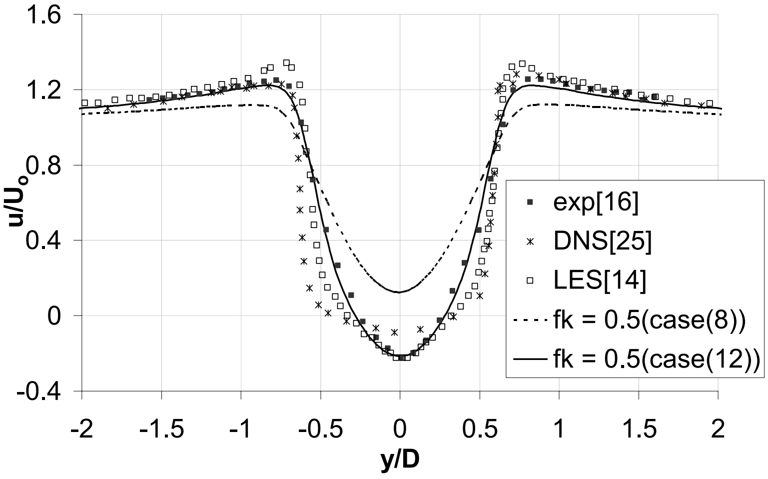

Figure 56: Effect of f_ε on PANS results. Comparison of the mean streamwise velocity at x/D = 1.06 for f_k = 0.5

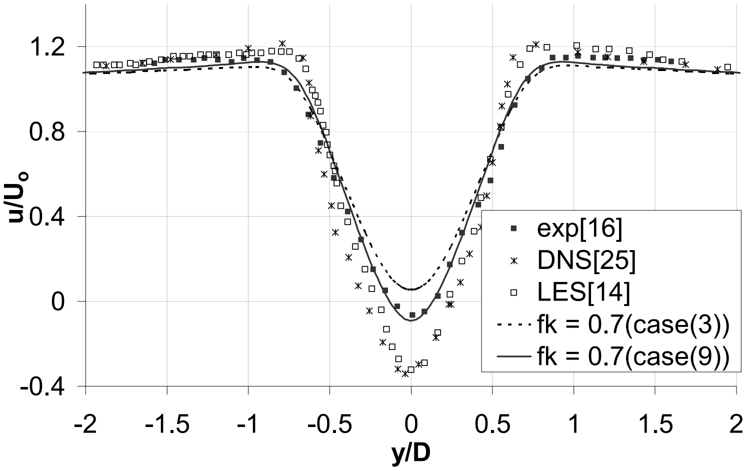

Figure 57: Effect of f_ε on PANS results. Comparison of the mean streamwise velocity at x/D = 1.54 for f_k = 0.7

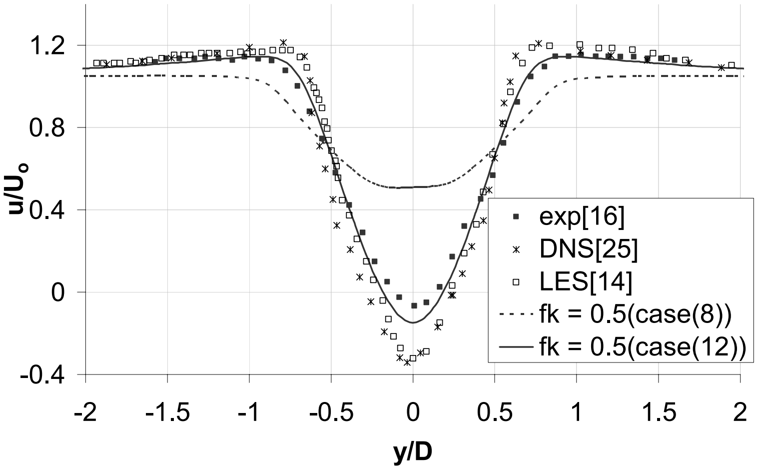

Figure 58: Effect of f_ε on PANS results. Comparison of the mean streamwise velocity at x/D = 1.54 for f_k = 0.5

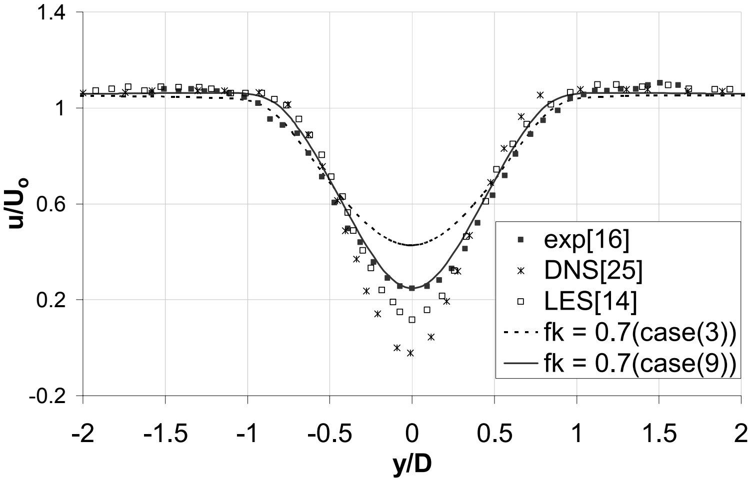

Figure 59: Effect of f_ε on PANS results. Comparison of the mean streamwise velocity at x/D = 2.02 for f_k = 0.7

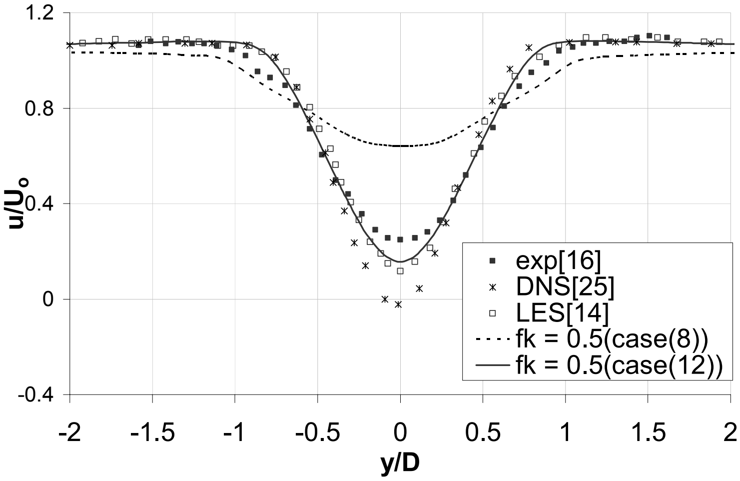

Figure 60: Effect of f_ε on PANS results. Comparison of the mean streamwise velocity at x/D = 2.02 for f_k = 0.5

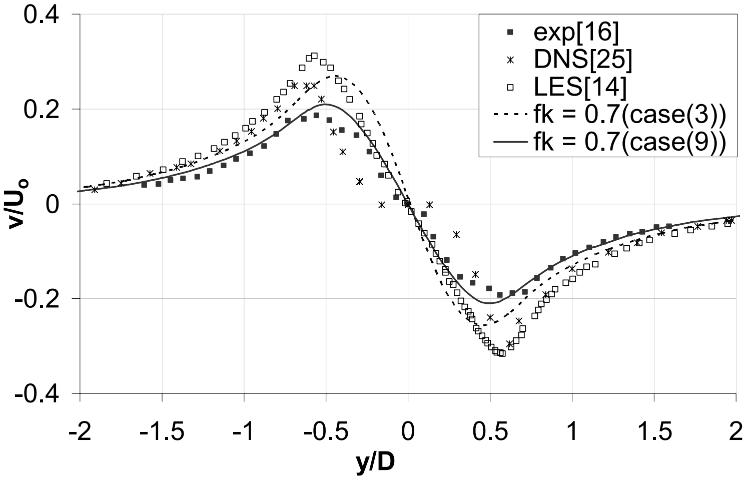

Figure 61: Effect of f_ε on PANS results. Comparison of the mean normal velocity at x/D = 1.54 for f_k = 0.7

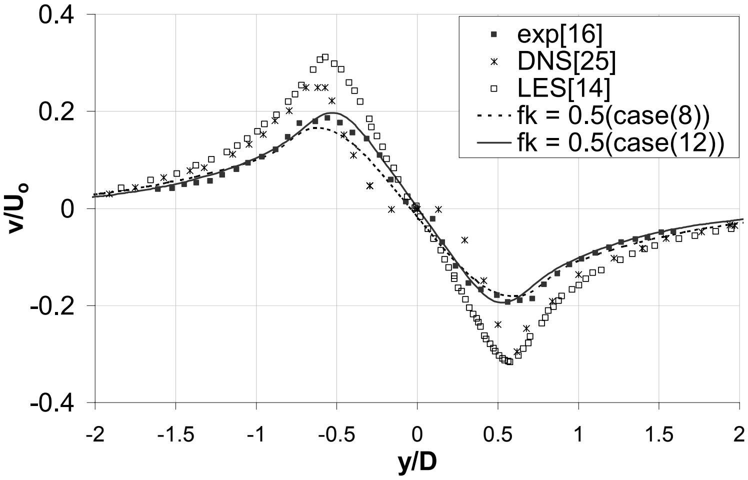

Figure 62: Effect of f_ε on PANS results. Comparison of the mean normal velocity at x/D = 1.54 for f_k = 0.5

6.3 EFFECT OF σ_{ku} VARIATION

Since PANS is a new type of hybrid turbulence model, effective application of this model to predict turbulence is only possible by a thorough understanding of each parameter and its influence in predicting nominal results which are comparable with the experiments. From the previous study we could easily conclude that varying f_ε such that $f_\varepsilon = f_k$ gives more accurate results for flow past a circular cylinder at Re_D 3900. The turbulent prandtl number for kinetic energy which is given by $\sigma_{ku} = \sigma_k \times f_k^2/f_\varepsilon$ is one of the model parameters whose effects on predicting turbulence is to be studied.

Case (14) with σ_{ku} fixed at unity (as in RANS) is compared with case (9) with σ_{ku} varying as the PANS formula. This study was performed for f_k value of 0.7 which is a good example to study the PANS methodology. The following paragraphs discuss the results from this study.

Figure 63 gives the mean streamwise velocity along the wake centerline for PANS calculations with $f_k = 0.7$. Also data from other experimental and numerical results are plotted for comparison purposes. Thought there is not much difference between the two results in the plots, but the PANS calculations with σ_{ku} corresponding to RANS formula is slightly more accurate than the one with σ_{ku} corresponding to the PANS formula. Appendix A gives a thorough insight into the reason for this increased accuracy for the low Reynolds number case.

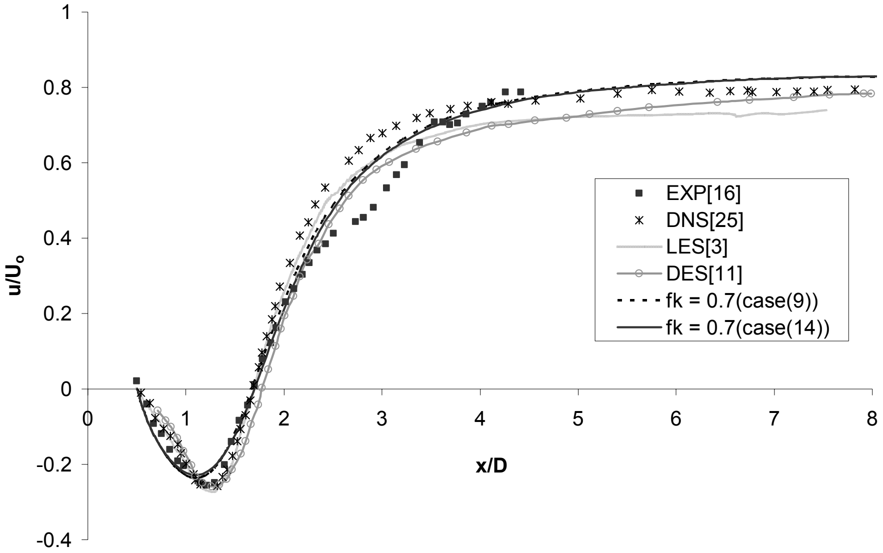

Figure 63: Effect of σ_{ku} on PANS results. Comparison of the mean streamwise velocity along wake centerline

Figures 64 – 70 give the mean velocity statistics at various planes in the wake of the cylinder. As before, other experimental and numerical results plotted alongside provide for better comparisons. The plots obtained from the σ_{ku} study prove that there is a slight improvement in the accuracy of the PANS results when σ_{ku} is fixed to unity for the low Reynolds number case.

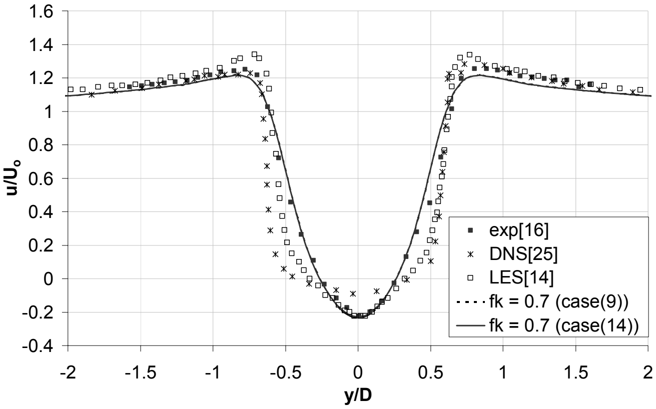

Figure 64: Effect of σ_{ku} on PANS results. Comparison of the mean streamwise velocity at x/D = 1.06

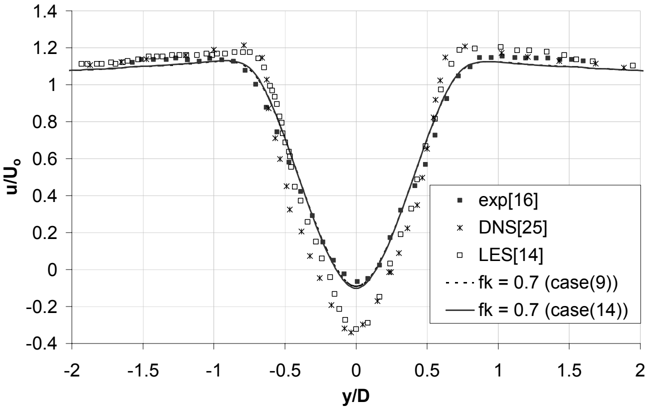

Figure 65: Effect of σ_{ku} on PANS results. Comparison of the mean streamwise velocity at x/D = 1.54

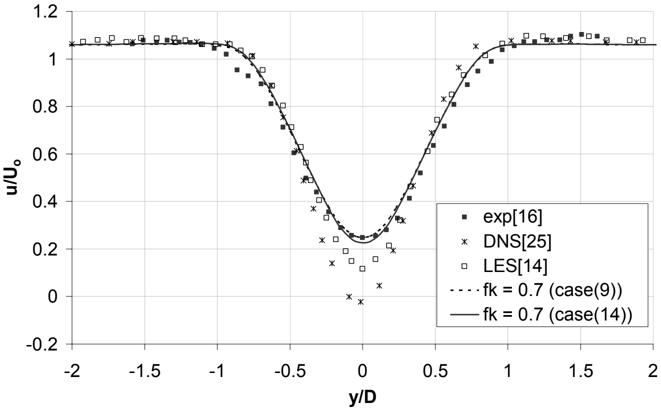

Figure 66: Effect of σ_{ku} on PANS results. Comparison of the mean streamwise velocity at x/D = 2.02

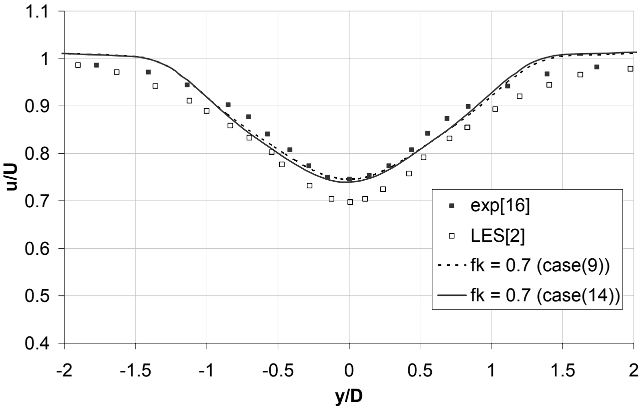

Figure 67: Effect of σ_{ku} on PANS results. Comparison of the mean streamwise velocity at x/D = 4.0

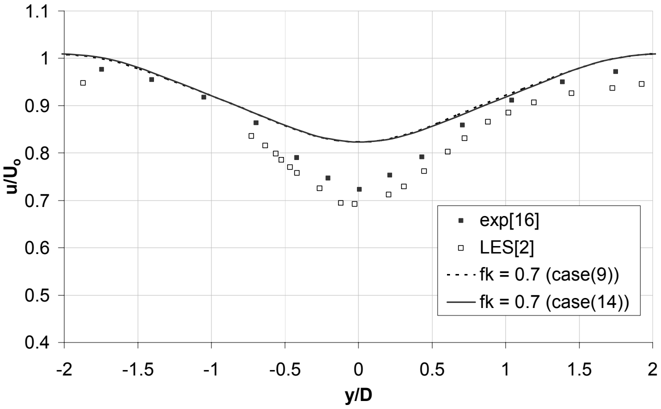

Figure 68: Effect of σ_{ku} on PANS results. Comparison of the mean streamwise velocity at x/D = 7.0

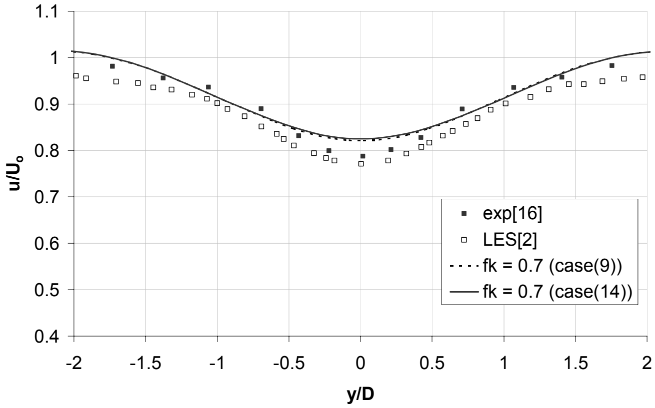

Figure 69: Effect of σ_{ku} on PANS results. Comparison of the mean streamwise velocity at x/D = 10.0

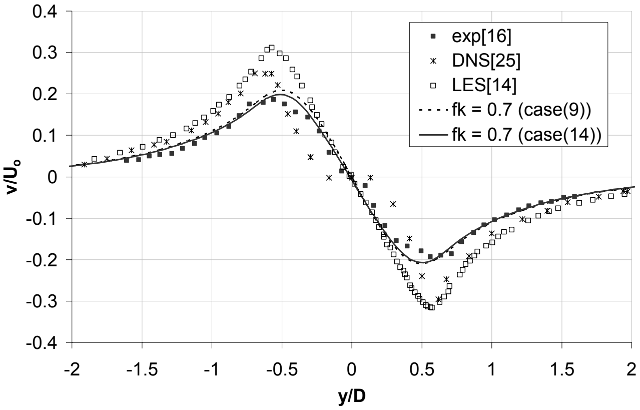

Figure 70: Effect of σ_{ku} on PANS results. Comparison of the mean normal velocity at x/D = 1.54

6.4 INFLUENCE OF f_k ON FLOW STATISTICS

Summarizing the results from our preliminary PANS calculations of flow past a circular cylinder at Re_D 3900 we can conclude that:

1. The study of varying the resolution control parameter for dissipation (f_ε) such that $f_\varepsilon = f_k$ for a given f_k value improves the accuracy of the solution largely for this low Reynolds number case.
2. Also, we can infer that fixing the turbulent Prandtl number for unresolved kinetic energy (σ_{ku}) to unity as in RANS method rather than varying it according to the PANS formula improves the accuracy of the solution slightly.

These preliminary results provide us with an intuition to set up the problem to test the PANS turbulence model for its flexibility in resolving turbulent scales of motion. Several cases were run by varying the resolution control parameter f_k from 1.0 (=RANS) to 0.5 to better understand PANS modeling capabilities. In the following paragraphs we present the results from these simulations and discuss their performance in comparison to the available experimental and numerical results. Most of the results presented in this discussion are obtained from case (1), case (11), and case (12) for f_k = 1.0, 0.7, and 0.5 respectively and with f_ε varying as f_k.

The flow around a circular cylinder at Re_D 3900 has been investigated experimentally by Ong and Wallace [19], and Lourenco and Shih [16]. DNS simulations were performed by Ma et al [17] and Tremblay et al. [25]. LES computations were presented by Breuer [3], Franke and Frank [7], Beaudan and Moin [2], and by Kravchenko and Moin [14].

6.4.1 Mean integral quantities

We first present the mean integral quantities. Table IV gives some of the important flow parameters from the PANS calculations. Also experimental results from Ong and Wallace [19] along with numerical results from Breuer [3], Kravenchenko and Moin [14] are presented. Key parameters presented include mean drag coefficient (C_d), mean back pressure coefficient (C_{pb}), mean separation angle (θ_s), and the strouhal number (S_t). The mean integral quantities strongly depend on the averaging time and this is discussed in detail by Franke and Frank [7].

The mean drag coefficient C_d, was calculated from the FLUENT output file which gives the time dependent force coefficients. For the same f_k value, PANS calculations with $f_\varepsilon = f_k$ predict a lesser value for C_d compared to the one with $f_\varepsilon = 1$. PANS calculations with $f_\varepsilon = f_k$ under-predict drag coefficient compared to the experimental values and numerical values. For $f_k = 0.5$, the predicted drag coefficient is 0.89 (exp.[19]: 0.99). However for the same case, but with $f_\varepsilon = 1$, the predicted drag coefficient is 1.23. Meanwhile, a favorable trend is observed in the variation of the drag coefficient as f_k decreases. It increases monotonically with decrease in the f_k value. The mean drag coefficient gets closer to the experimental values with decrease in the f_k value.

Table IV: Mean integral quantities for Re_D 3900

Case	**Grid Resolution**	**Δt^***	**C_d**	**-Cpb**	**S_t**	**θ_{sep}**
Experimental			0.99±0.05	0.88±0.05	0.215±0.005	85.0±2.0
DNS [25]				0.84	0.219	
LES [14]	205 x 185 x 48		1.04	0.94	0.21	88
LES [7]	184 x 192 x 32		0.978	0.85	0.209	88.2
LES [3]	165 x 165 x 32		1.071	1.011	0.215	87.7
PANS ($f_k = 0.5$) ($f_k = f_\varepsilon$)	160 x 160 x 36	0.105	0.89	0.72	0.18	95.98
PANS ($f_k = 0.7$) ($f_k = f_\varepsilon$)	160 x 160 x 36	0.105	0.87	0.68	0.175	95.99
PANS ($f_k = 1.0$)	85 x 85	0.21	0.832	0.71	0.169	117

The correlation between C_d and C_{pb} is nearly trivial as indicated earlier in the Re_D 140000 simulations. As in C_d behavior, the value of C_{pb} is under predicted for $f_e = f_k$ cases and it is over-predicted for cases with $f_e = 1$. Also C_{pb} is insensitive to any changes in the f_k value as the value remains fairly constant for f_k being reduced from 1.0 to 0.5.

Figure 71 gives the variation of the pressure coefficient (C_p) on the surface of the cylinder as a function of θ, the angle measured from the forward stagnation point. Two LES results are presented in this plot. They are LES results from Breuer [3] and LES results from Kravchenko and Moin [14]. The DNS results are from Ma et al. [17]. The DES simulations are from Hansen and Forsythe [11]. The PANS simulation with $f_k = 0.7$ and 0.5 having identical grid resolution and time-step produce similar behavior in the variation of C_p. However PANS with $f_k = 0.5$ is slightly more accurate compared to PANS with $f_k = 0.7$ for $\theta > 90^o$. For the RANS case ($f_k = 1.0$) the pressure drop is large as the flow separation is delayed. However for $\theta > 120^o$ the base pressure rises abruptly and the base pressure at the back of the cylinder is same as the PANS cases. The RANS calculations give the least accurate results. The C_p curve for $f_k = 0.7$ and $f_k = 0.5$ tends to move close towards the DNS results with a monotonic behavior.

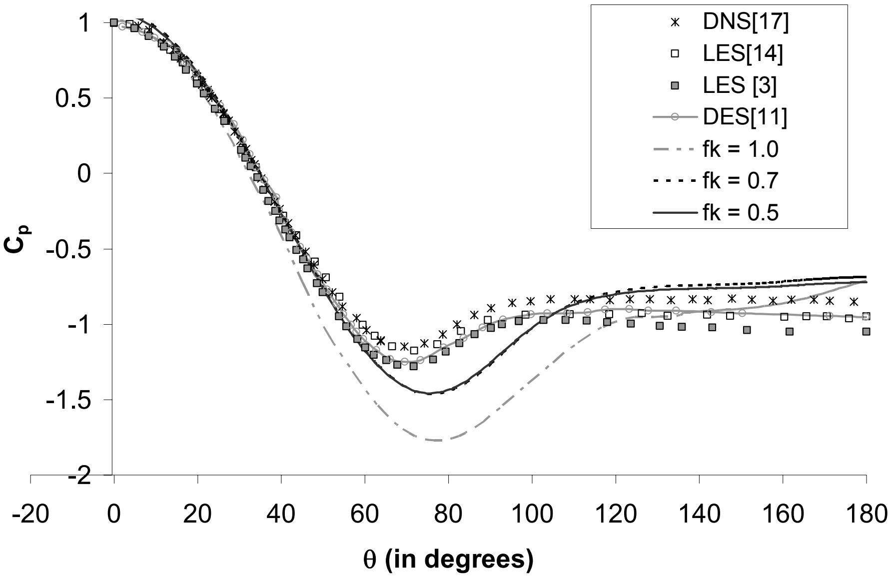

Figure 71: C_p variation on the cylinder surface for various f_k values

From the pressure distribution plots, we can observe that in PANS simulations the peak pressure in the base is much too high than the other numerical results and hence, separation occurs further downstream. The lowest value of θ_s for PANS simulations is 95.98°. Experiments predict the separation to occur before the apex of the cylinder at 85°. Ma et al. [17] do not give any value for θ_s in their DNS study. In consistence of predicting the flow parameters, the results from PANS calculations with f_k = 0.5 is more accurate compared to RANS but still not in good agreement with the measured values.

The Strouhal number (S_t) of the vortex shedding frequency is typically found to be 0.21 for Re_D 3900. Table V gives S_t for the various PANS cases run. They range from 0.169 – 0.193. PANS calculations under-predict S_t compared to the other numerical methods. But the accuracy of the results improves with decreasing f_k value.

6.4.2 Mean flow and turbulent statistics

In this section, we present the mean flow statistics and compare with existing experimental and numerical results. The experimental results presented are from PIV measurements of Lorenco and Shih [16]. The numerical results include DNS data from Ma et al. [17], LES results from Beauden and Moin [2], Kravchenko and Moin [14], and from Breuer [3]. The flow statistics for the PANS simulations were accumulated over approximately $t^* = 150U_o/D$.

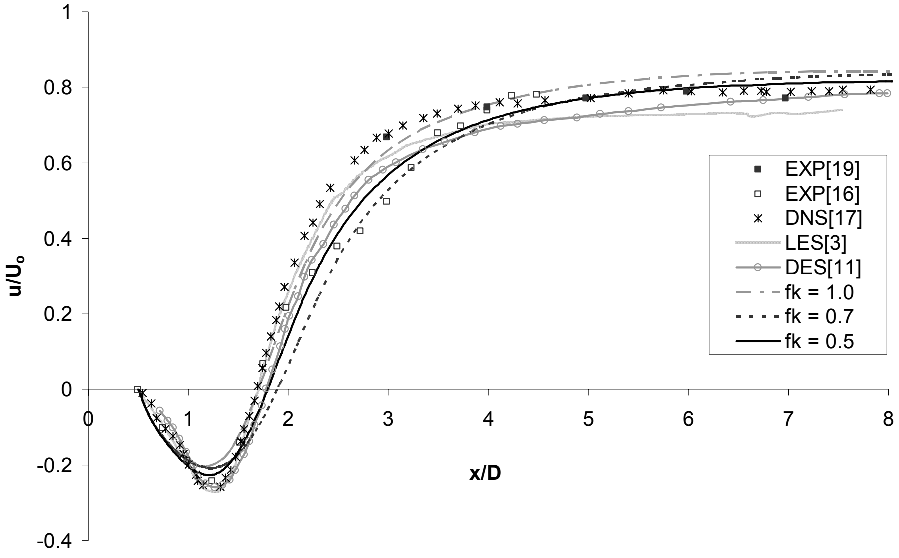

Figure 72: Effect of f_k variation. Comparison of the mean streamwise velocity along the wake centerline

Figure 72 gives the mean streamwise velocity along the wake centerline at y/D = 0. The PANS calculations with f_k = 1.0 (RANS), 0.7, and 0.5 agree very well with the experimental and numerical results compared. Even thought the variation is very less, the RANS calculations slightly under-predict the recirculation length and we get improved accuracy by decreasing the f_k value to 0.5. PANS calculations with $f_k = 0.5$ agrees more accurately with the compared results in predicting the size of the separation bubble. In the near wake region (x/D< 3) the PANS calculations are closer to the experimental results of Lorenco and shih [16] in predicting the size of the recirculation bubble compared to the LES results of Beauden [2] and Breuer [3]. In the wake region, 3<x/D <10, the RANS calculations tend to over-predict the mean streamwise velocity, but with PANS calculations by reducing f_k value, the mean velocity statistics converge towards experimental values. Overall the PANS calculations agree very well with the experimental results and numerical results.

Figures 73 - 75 gives the mean streamwise velocity at three different planes (x/D = 1.06, 1.54, and 2.02) in the very near wake (x/D <3). In figure 73 the experimental results predict a V-shaped profile for the mean streamwise velocity, whereas the DNS and the LES simulations predict a U-shaped profile. Both Ma et al. [17] and Kravchenko and Moin [14] give a detail discussion on the reasons for the cause of U-shaped profile at this section in the wake region. They conclude that the shape of the velocity profile is directly related to the level of velocity fluctuations and, consequently, to the transition in the shear layers. Franke and Frank [7] in their LES simulations demonstrate that as the averaging times increases, the mean streamwise velocity develops from a V-shaped profile to a U-shape profile at x/D = 1.06. In our simulations, the RANS simulations predict the velocity profile closer to the experimental results with a V-shape profile. The PANS results with f_k values of 0.7 and 0.5 provide very accurate results for flow statistics on this plane. The PANS calculations with f_k value of 0.5 overlaps the experimental results through most of the plot.

Figure 74 gives the mean streamwise velocity at x/D = 1.54. From the plot we can observe that PANS calculations show better comparison with the experimental results than the other numerical results plotted. Also, there is a monotonic increase in the accuracy of the solution with decrease in f_k value. Figure 75 gives the mean streamwise velocity along the wake centerline at x/D = 2.02. This plot too clearly demonstrates the increased accuracy obtained in predicting the flow statistics by reducing f_k value from 1.0 to 0.5. Comparing the flow statistics at the near wake region, we can clearly comprehend the accuracy with which PANS method predicts the complex flow past a circular cylinder.

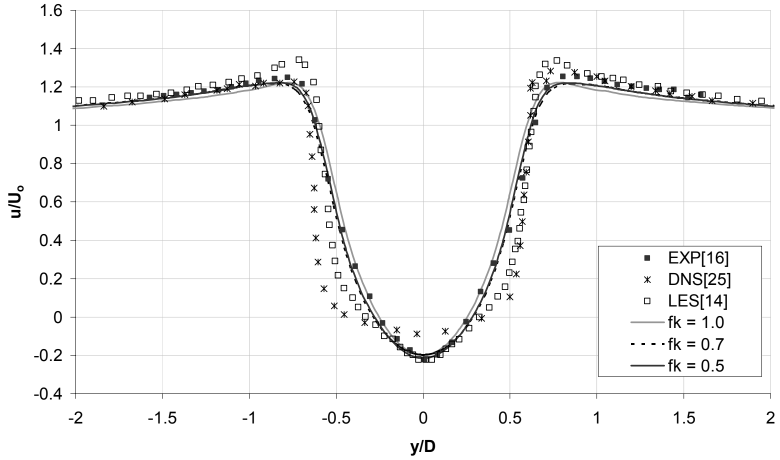

Figure 73: Effect of f_k variation. Comparison of the mean streamwise velocity at x/D = 1.06

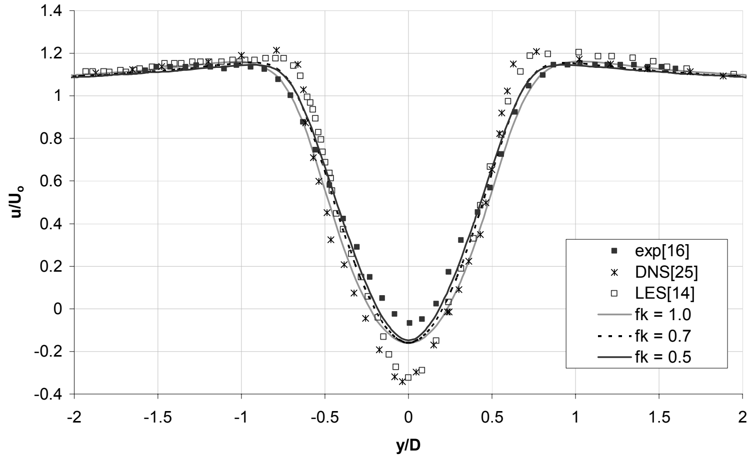

Figure 74: Effect of f_k variation. Comparison of the mean streamwise velocity at x/D = 1.54

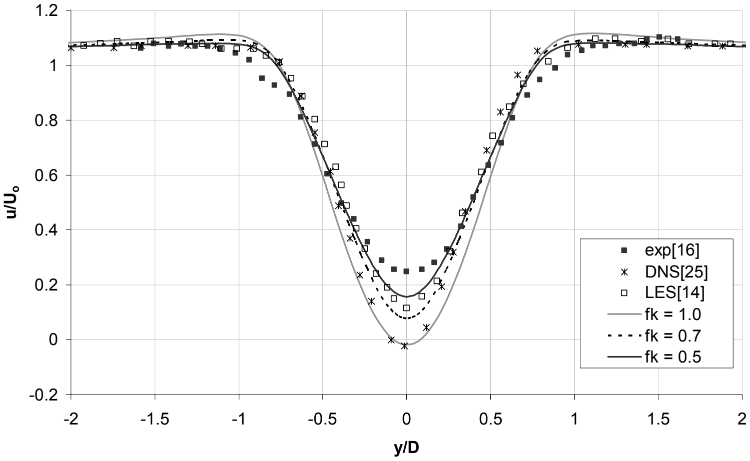

Figure 75: Effect of f_k variation. Comparison of the mean streamwise velocity at x/D = 2.02

Figures 76, 77, and 78 give the mean streamwise velocity at three different locations (x/D = 4, 7, and 10 respectively) in the far wake (x/D > 3) to evaluate the accuracy of the PANS results in the downstream region. The trend of PANS results getting closer to the experimental results with decreasing f_k values is further demonstrated in these plots for flow statistics in the far wake region.

Comparison of PANS results with different f_k values for mean normal velocities at three different planes (x/D = 1.54, 3, 4) are presented in figures 79, 80, and 81. In all these plots we can observe that the accuracy of the solution improves drastically with decrease in the f_k value. This trend is uniform for all the flow statistics including the integral quantities. Overall PANS results provide accurate results in comparison to the experimental results for various flow statistics plotted. The accuracy of the results increases with decrease in f_k value.

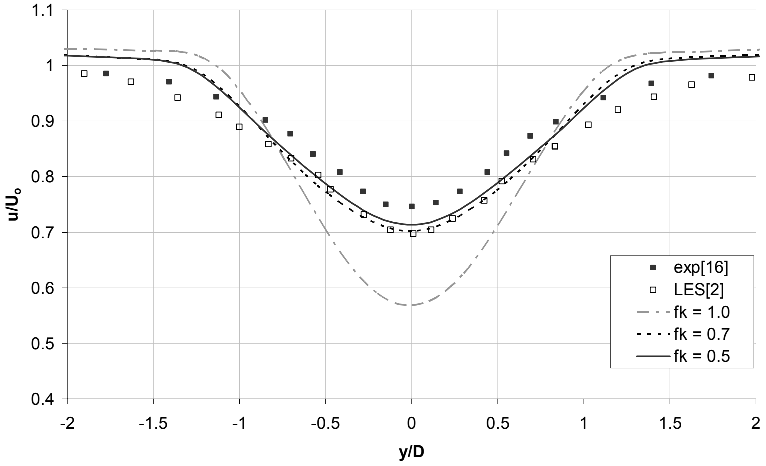

Figure 76: Effect of f_k variation. Comparison of the mean streamwise velocity at x/D = 4.0

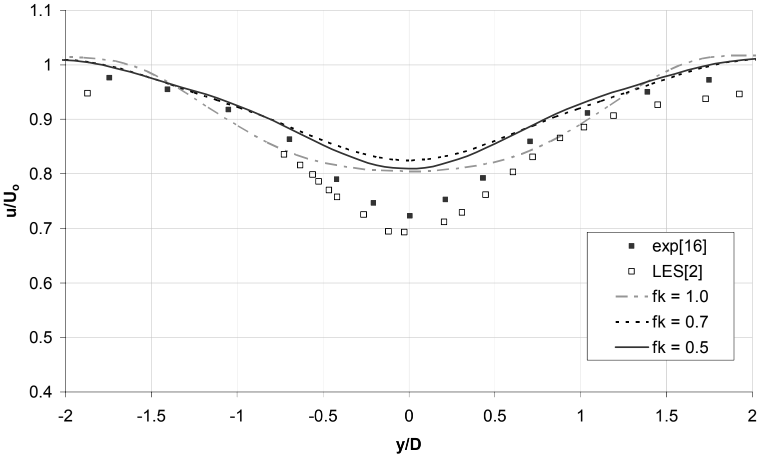

Figure 77: Effect of f_k variation. Comparison of the mean streamwise velocity at x/D = 7.0

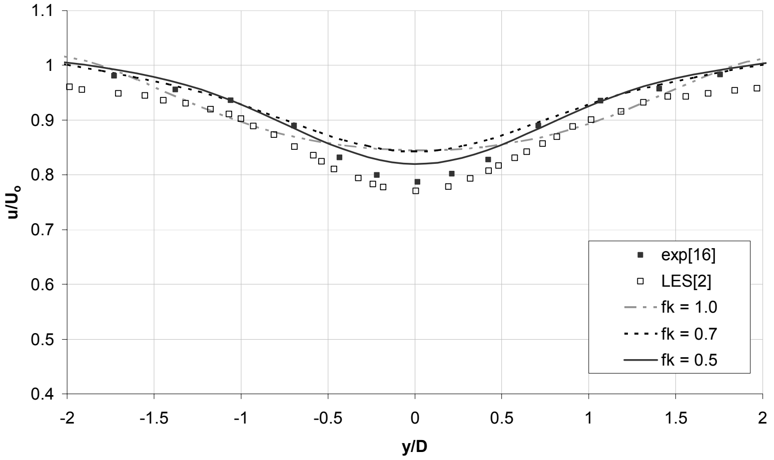

Figure 78: Effect of f_k variation. Comparison of the mean streamwise velocity at x/D = 10.0

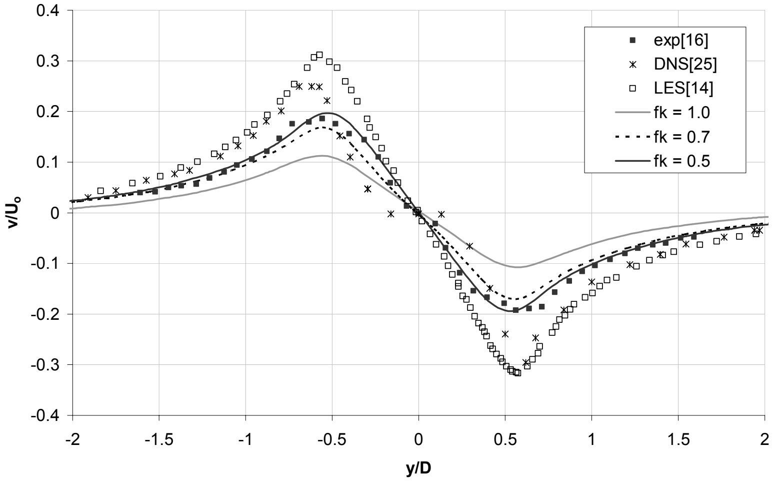

Figure 79: Effect of f_k variation. Comparison of the mean normal velocity at x/D = 1.54

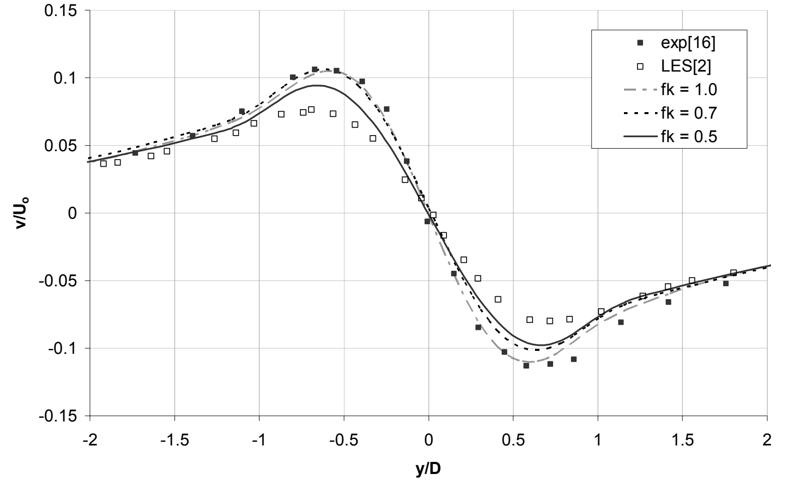

Figure 80: Effect of f_k variation. Comparison of the mean normal velocity at x/D = 3

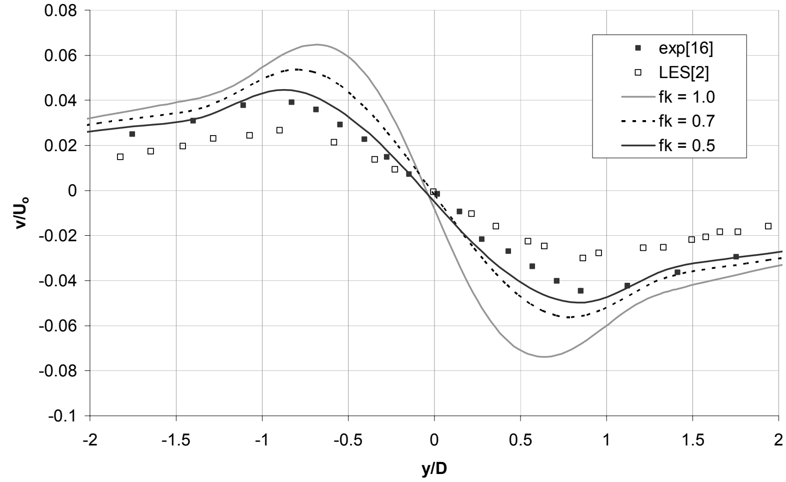

Figure 81: Effect of f_k variation. Comparison of the mean normal velocity at x/D = 4

Figures 82 – 97 depict the qualitative comparison between PANS calculations for various f_k values. These plots provide for the direct comparison of the PANS results of various physical resolution and include instantaneous contours of various quantities plotted on the z/D = 1 plane. Figures 82, 83, and 84 give the instantaneous contours of velocity magnitude for PANS with various f_k values. At this Reynolds number which is practically low for most engineering purposes, we can observe that by decreasing f_k value, more flow structures are resolved and the complexity of the flow in the wake increases. Also, the recirculation bubble size which is large for RANS calculations decreases and tends towards experimental values with decreasing f_k value. The same pattern of improved resolution of the flow with decrease in the f_k value can be observed in the instantaneous vorticity contours plotted for various f_k values as shown in figures 85 - 87. More flow structures appear in the wake region for PANS with f_k value of 0.5. However due to the Reynolds number being low, the visual distinction between the various f_k values is not as sharp in the ReD 140,000 case. Figures 88 - 90 give the contour plots of unresolved kinetic energy for various f_k values. Recall that the basis of PANS methodology is placing the cut-off based on the amount of kinetic energy to be resolved. So by decreasing the f_k value we are resolving more of the kinetic energy content of the flow and these set of figures clearly demonstrate this behavior of PANS that as f_k reduces the unresolved kinetic energy content in the flow reduces. The same behavior is observed in the contour plots of unresolved eddy viscocity in figures 91 – 93. By reducing f_k, we are decreasing the levels of unresolved eddy viscosity in the flow thus leading to better accuracy in predicting the complexity of the flow.

Figures 94 - 97 give a comparison between PANS calculations with $f_k = 0.7$ and $f_k = 0.5$. Figures 94 and 95 present the instantaneous contours of x-vorticity for the two PANS calculations. We can clearly observe that by reducing the f_k value, the vortices get sharper and more flow structures are resolved. This effect is less obvious in the instantaneous z-vorticity contours plotted in figures 96 and 97.

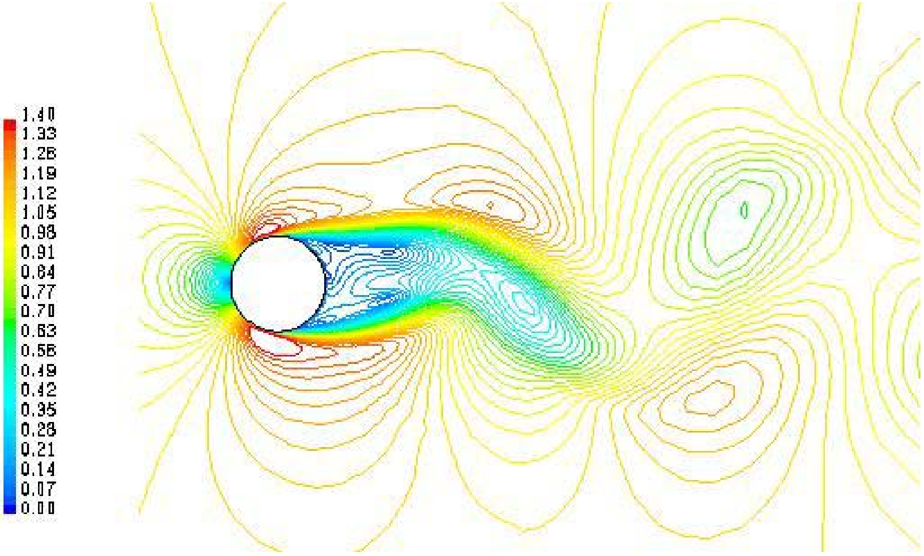

Figure 82: Instantaneous contours of velocity magnitude for f_k = 1.0 along z/D = 1.0 plane

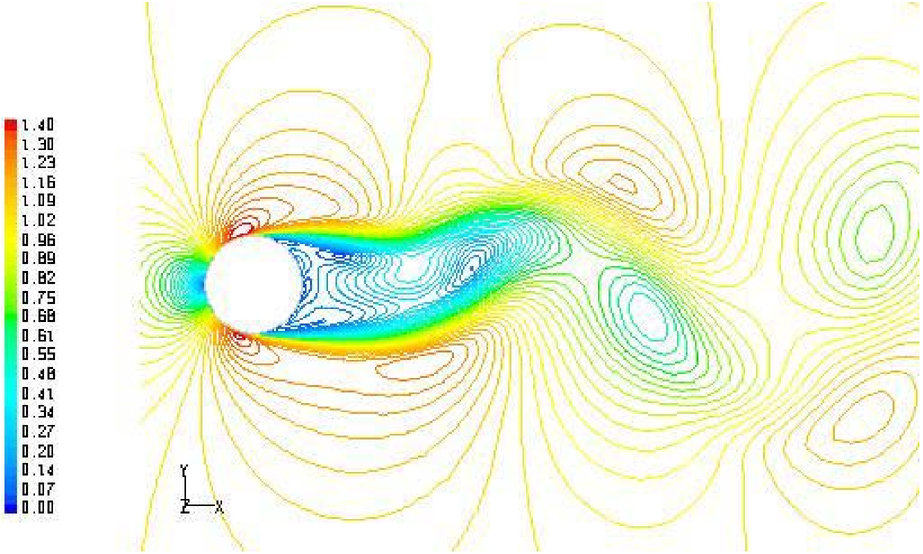

Figure 83: Instantaneous contours of velocity magnitude for f_k = 0.7 along z/D = 1.0 plane

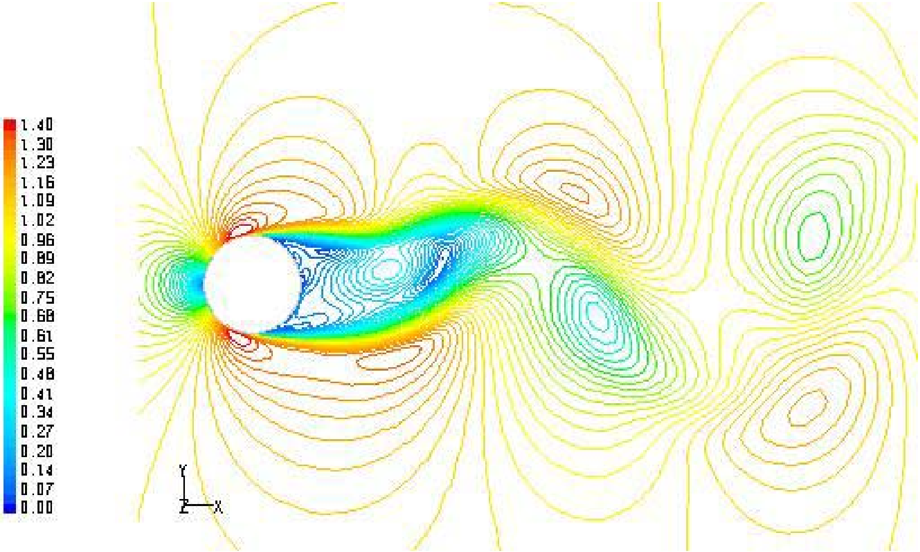

Figure 84: Instantaneous contours of velocity magnitude for f_k = 0.5 along z/D = 1.0 plane

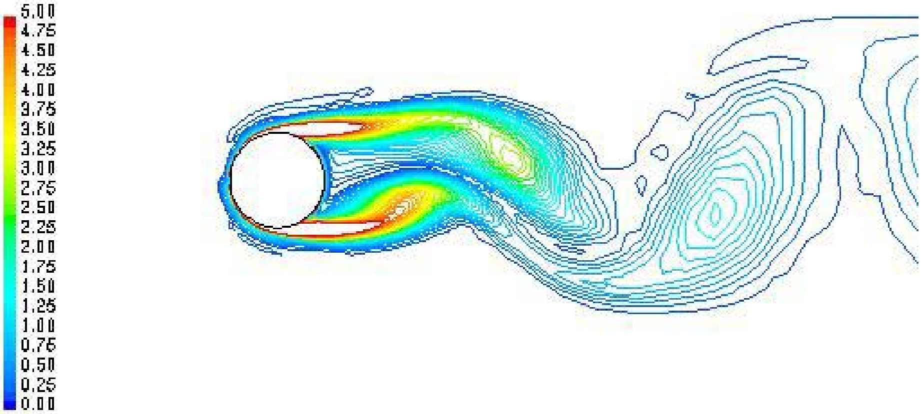

Figure 85: Instantaneous contours of vorticity magnitude for f_k = 1.0 along z/D = 1.0 plane

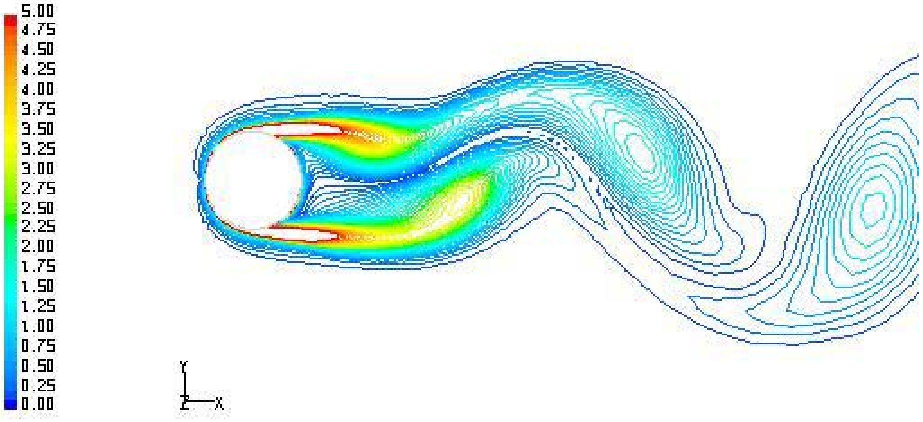

Figure 86: Instantaneous contours of vorticity magnitude for f_k = 0.7 along z/D = 1.0 plane

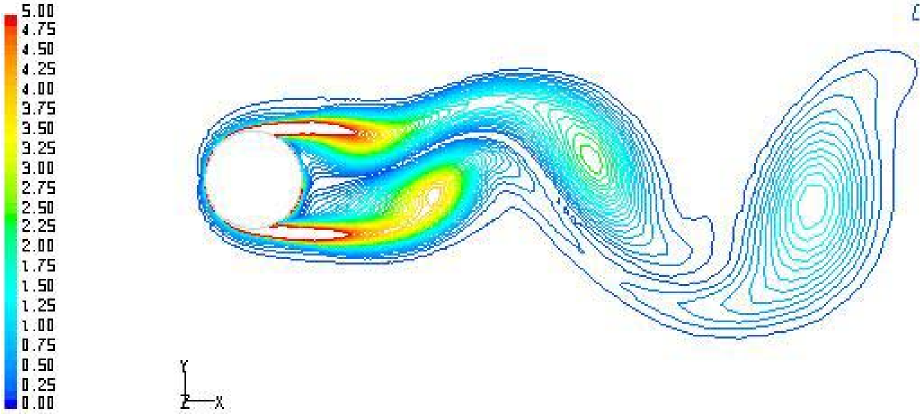

Figure 87: Instantaneous contours of vorticity magnitude for f_k = 0.5 along z/D = 1.0 plane

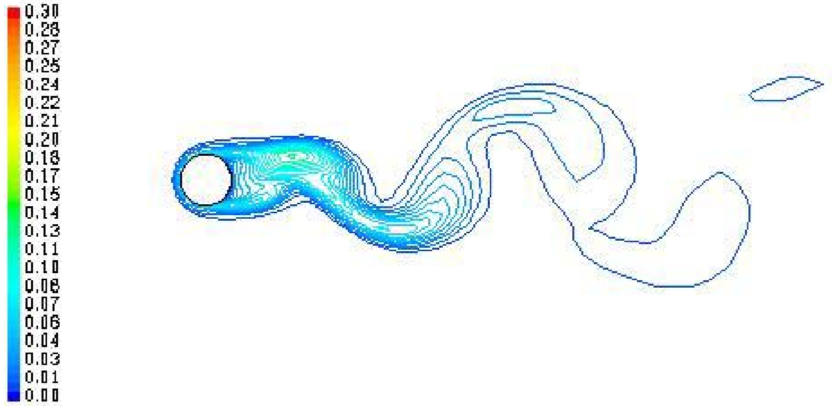

Figure 88: Contours of unresolved kinetic energy for f_k = 1.0 along z/D = 1 plane

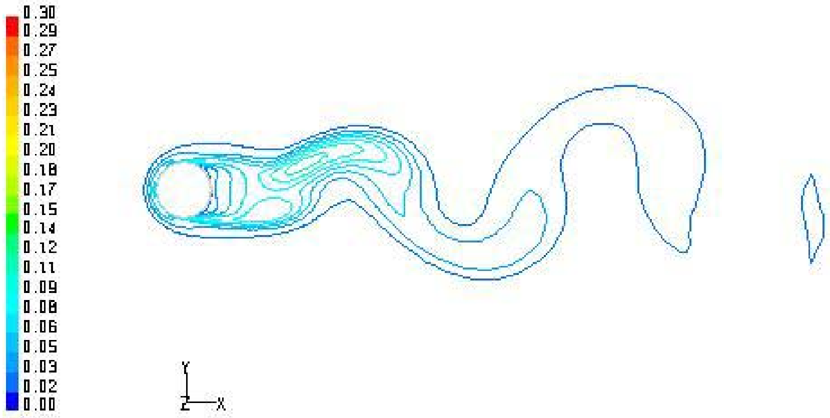

Figure 89: Contours of unresolved kinetic energy for f_k = 0.7 along z/D = 1 plane

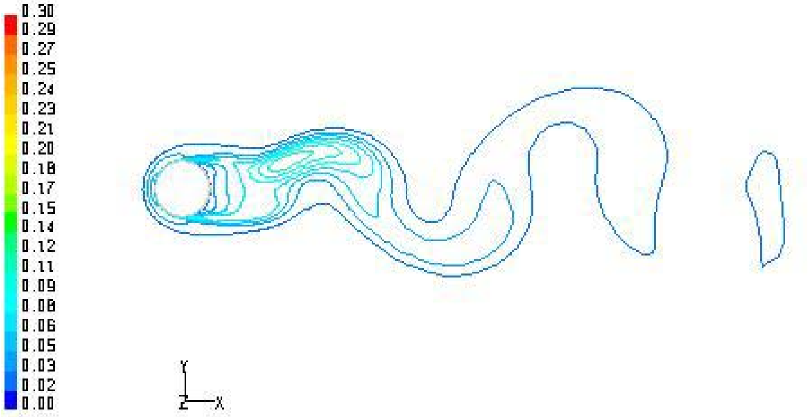

Figure 90: Contours of unresolved kinetic energy for *f*$_k$ = 0.5 along z/D = 1 plane

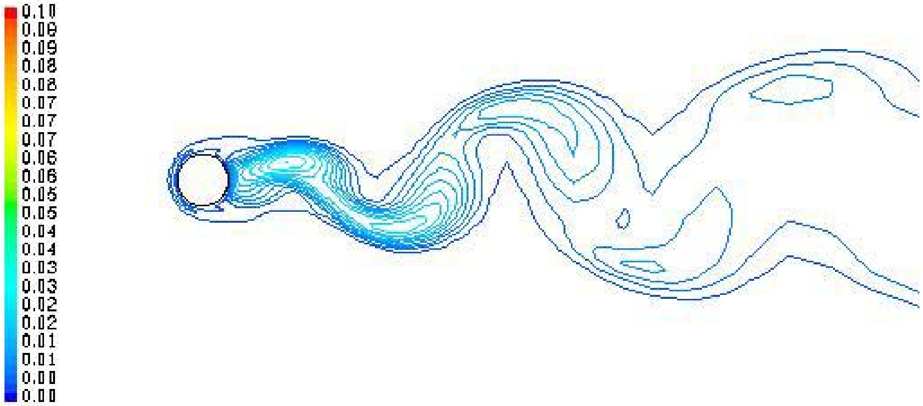

Figure 91: Contours of unresolved eddy viscosity for *f*$_k$ = 1.0 along z/D = 1.0 plane

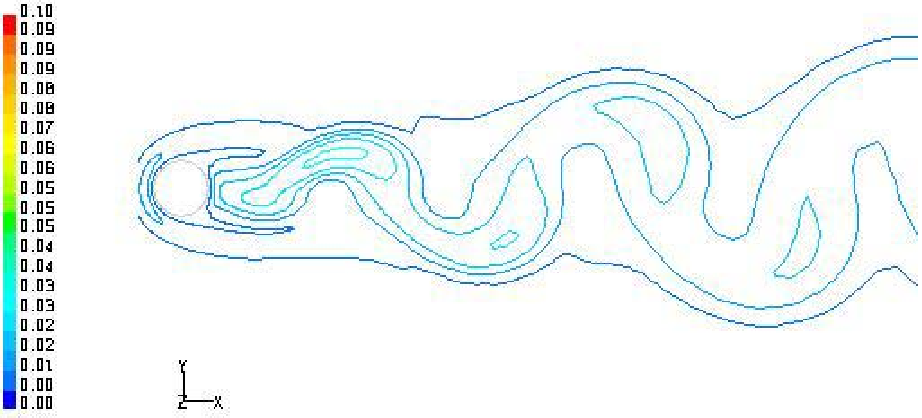

Figure 92: Contours of unresolved eddy viscosity for $f_k = 0.7$ along z/D = 1.0 plane

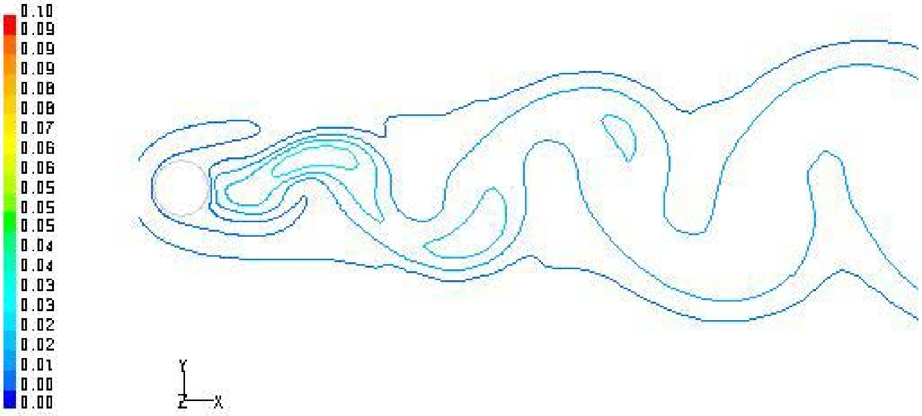

Figure 93: Contours of unresolved eddy viscosity for $f_k = 0.5$ along z/D = 1.0 plane

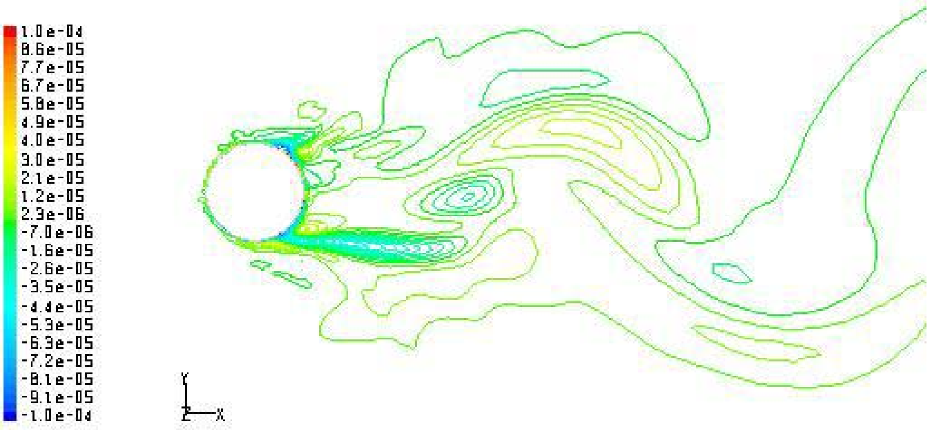

Figure 94: Instantaneous contours of x-vorticity for f_k = 0.7 along z/D = 1.0 plane

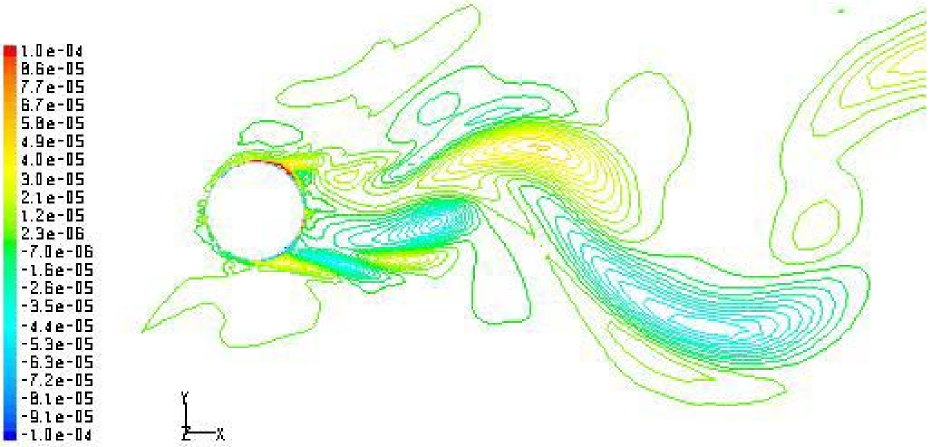

Figure 95: Instantaneous contours of x-vorticity for f_k = 0.5 along z/D = 1.0 plane

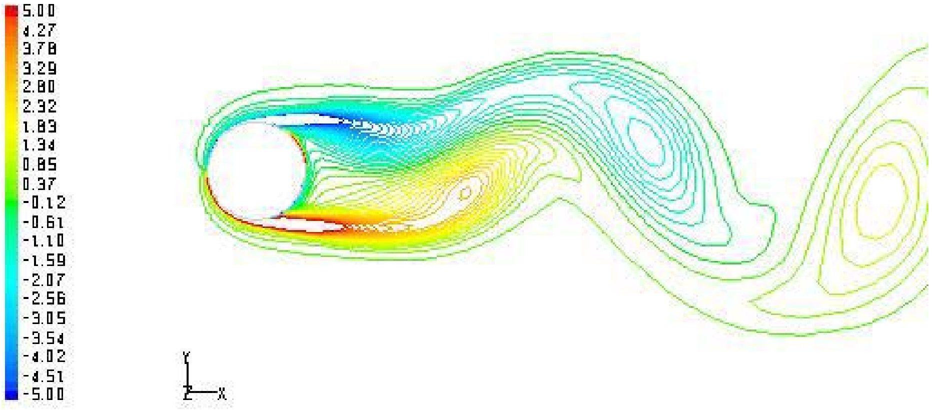

Figure 96: Instantaneous contours of z-vorticity for f_k = 0.7 along z/D = 1.0 plane

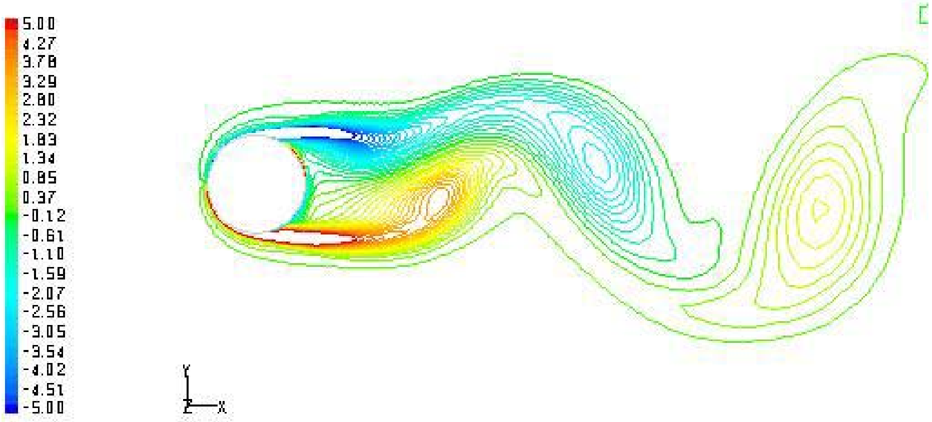

Figure 97: Instantaneous contours of z-vorticity for f_k = 0.5 along z/D = 1.0 plane

7. CONCLUSION

The flow past a circular cylinder at sub-critical Reynolds numbers of Re_D 140000 and Re_D 3900 were simulated by the method of PANS. Both these flows are categorized as subcritical since the boundary layer separation is laminar. The present study was conducted to carry out extensive investigation of numerical and modeling capabilities of this newly developed approach to model chaotic behavior in turbulent flows. The commercial CFD package FLUENT was used to conduct the cylinder flow simulations. The PANS capability of performing arbitrary–resolution simulations by decreasing the f_k value is thoroughly exploited by conducting the cylinder flow simulations at f_k values of 1.0, 0.7, and 0.5 for both Reynolds numbers studied.

The RANS simulations predict a much delayed separation for Re_D 140,000 and Re_D 3900. This is mainly due to an unrealistic estimation of eddy viscosity in the stagnation region where the flow remains laminar. The PANS calculations overcome this difficulty. As the f_k value is reduced, the unresolved kinetic energy progressively decreases and also the unresolved eddy viscosity leading to more realistic and accurate results. By decreasing the f_k value more and more unsteady scales of motion are captured as indicated in the instantaneous vorticity contour plots. The vorticity structures get sharper and more complex leading to better visualization of the complexity of the wake structures evolving from the flow past a circular cylinder. Comparing the mean statistics of the flow at various cross-sections in the wake region, we can decisively conclude that results typically go from RANS to experimental predictions with decreasing f_k value. In fact, the PANS simulations produce more accurate comparisons for some flow statistics than the LES simulations.

7.1 SUMMARY OF Re_D140000

The test case of turbulent flow past a circular cylinder at Re_D 140000 involves remarkably complex flow features. The present PANS calculations demonstrate the feasibility of applying PANS to such practically relevant high Reynolds number flows. LES approach to this problem is an expensive approach due to its demanding requests of computational time and accurate mesh generation. In PANS calculations, one can control the grid resolution by controlling the resolution control parameters (f_k and f_ε) and hence, these calculations can be performed with less computational effort. This aspect of PANS makes it a viable option in modeling turbulent flows with high Reynolds number.

The RANS calculations as observed in section 5, do not predict any motion in the spanwise direction since there is no production in the z-direction. Hence even a three-dimensional simulation produces only two-dimensional variation which is physically incorrect as previous experimental and numerical studies have proven that the wake region has three dimensional vortical structures. PANS simulations with $f_k = 0.5$ and $f_k = 0.7$ clearly capture the three dimensionality of the wake region in the cylinder flow. The agreement of PANS calculations with experimental results of Cantwell and Coles [5], LES results of Breuer [4], and DES results of Travin et al. [24] is fair. The PANS simulations predict the drag coefficient within experimental uncertainty. The separation angle and the Strouhal number are slightly over-predicted in comparison to experimental values, but agree well with the DES results of Travin et al. [24].

For this high Reynolds number calculation setting $f_\varepsilon = 1$ and $\sigma_{ku} = \sigma_k \times f_k^2/f_\varepsilon$ in the PANS parameters predicted the results with better accuracy. This is in agreement with the physics of the flow at high Reynolds number where there is no overlapping between the energy spectra and dissipation spectra (see appendix A).

7.2 SUMMARY OF Re_D 3900

The PANS simulation of turbulent flow past a circular cylinder at Re_D 3900 produced good agreement with the compared experimental and numerical results. Thorough investigation of the cases and resolution control parameters concluded that setting $f_\varepsilon = f_k$ and $\sigma_{ku} = \sigma_k$ gave the most accurate results. These variations are in accordance with the physics of the flow at low Reynolds number where there is overlapping of the energy and dissipation spectra (refer appendix A). The PANS simulations in general under-predicted the mean drag coefficient and also predicted the boundary layer separation to occur after the apex of the cylinder whereas experiments predict the separation to occur before the apex of the cylinder. The mean flow statistics computed at various cross-sections in the wake region were accurate in comparison to experimental and numerical results. The PANS calculations failed to capture the flow complexity in the spanwise direction as the iso-vorticity contour plots failed to show any significant variation in the spanwise direction.

With this, we have successfully proven the applicability of PANS in predicting turbulent flows of engineering importance. PANS can perform turbulent flow simulations of varying resolution with less computational efforts.

REFERENCES

1. Achenbach, E., Distribution of local pressure and skin friction around a circular cylinder in cross-flow up to Re 5×10^6. *J. Fluid Mech.* **34**(4) (1968) 625–639.
2. Beaudan, P. and Moin, P., Numerical experiments on the flow past a cylinder at sub-critical Reynolds number. *Report No. TF-62* (1994) Department of Mechanical Engineering, Stanford University, Stanford, California.
3. Breuer, M., Large eddy simulation of the subcritical flow past a circular cylinder: Numerical and modeling aspects. *Internat. J. Numer. Methods Fluids* **28** (1998) 1281–1302.
4. Breuer, M., A challenging test case for large eddy simulation: high Reynolds number circular cylinder flow. *Internat. J. Heat Fluid Flow* **21** (2000) 648–654.
5. Cantwell, B. and Coles, D., An experimental study of entrainment and transport in the turbulent near wake of a circular cylinder. *J. Fluid Mech.* **136** (1983) 321–374.
6. Ferziger, H. J., Peric, M., *Computational methods for fluid dynamics,* Springer-Verlag: New York (2002).
7. Franke, J., and Frank, W., Large eddy simulation of the flow past a circular cylinder at $Re_D = 3900$. *J. Wind Eng. Ind. Aerodyn.* **90** (2002) 1191–1206
8. Germano, M., Turbulence: the filtering approach *J. Fluid Mech.* **238** (1992) 325–336.
9. Girimaji, S. S., Partially-averaged Navier Stokes method: a variable resolution (from RANS to DNS) turbulence model. Submitted to *Phys. Fluids*.
10. Girimaji, S. S., Srinivasan, R., and Jeong, E., PANS turbulence model for seamless transition between RANS and LES: fixed-point analysis and preliminary results. FEDSM2003-45336, *Proc. of ASME FEDSM'03 2003 4th ASME-JSME Joint Fluids Engineering Conferences* Honolulu, Hawaii, 2003.

11. Hansen, P. R., Forsythe, R. J., Large and detached eddy simulations of a circular cylinder using unstructured grids. *41st AIAA Aerospace Sciences Meeting and Exhibit* Reno, Nevada **2003-0775** (2003)
12. Jeong, E., *Selected problems in turbulence theory and modeling*, Ph.D. Dissertation Department of Aerospace Engineering, Texas A&M University: College Station (2003)
13. Jiménez, J., and Moser, D. R., LES: Where are we and what can we expect. *29th AIAA fluid dyn. conference* Albuquerque, New Mexico **98-2891** (1998)
14. Kravchenko, A.G. and Moin, P., Numerical studies of flow over a circular cylinder at Re_D 3900. *Phys. Fluids* **12**(2) (2000) 403–417.
15. Launder, B.E. and Sandham, N.D., *Closure strategies for turbulent and transitional flows.* Cambridge University Press: Cambridge(2002)
16. Lourenco, L. M., Shih, C., Characteristics of the plane turbulent near wake of a cylinder, A particle image velocimetry study. Unpublished, data obtained from [2] (1993)
17. Ma, X., Karamanos, G.-S., and Karniadakis, G. E., Dynamics and low-dimensionality of a turbulent wake. *J. Fluid Mech.* **410** (2000) 29–65.
18. Mittal, R., and Moin, P., Suitability of upwind-biased finite-difference schemes for large-eddy simulation of turbulent flows. *AIAA* **35** (1997) 1415–1417
19. Ong, L., and Wallace, J., The velocity field of the turbulent very near wake of a circular cylinder. *Exps. Fluids* **20** (1996) 441–453.
20. Pope, S. B., *Turbulent flows.* Cambridge University Press: Cambridge (2000)
21. Rocchi, D., and Zasso, A., Vortex shedding from a circular cylinder in a smooth and wired configuration: comparison between 3D LES simulation and experimental analysis. *J. Wind Eng. Ind. Aerodyn.* **90** (2002) 475–489
22. Roshko, A., Experiments on the flow past a circular cylinder at very high Reynolds number. *J. Fluid Mech.* **10**(3) (1961) 345–356.

23. Shih, W. C. L., Wang, C., Coles, D., and Roshko, A., Experiments of flow past rough circular cylinders at large Reynolds numbers. *J. Wind Eng. Ind. Aerodyn.* **49** (1993) 351–368
24. Travin, A., Shur, M., Strelets, M., and Spalart, P., Detached-eddy simulations past a circular cylinder, *Flow, Turbulence and Combustion* **63** (1999) 293–313
25. Tremblay, F., Manhart, M., and Friedrich, R., DNS of flow around a circular cylinder at subcritical Reynolds number with Cartesian grids. In: *Proc. of the Eight European Turbulence Conference* Barcelona, Spain EUROMECH, CIMNE, 27-30 June, 2000, 659–662.
26. Wang, M., Catalano, P., and Laccarino, G., Prediction of high Reynolds number flow over a circular cylinder using LES with wall modeling. In: *Ann. Research Briefs* Stanford, California, Center for Turbulence Research (2001) 45–50.
27. Williamson, C., Vortex dynamics in the cylinder wake. *Ann. Rev. Fluid Mech.* **28** (1996) 477–534.
28. Zdravkovich, M.M., *Flow around Circular Cylinders*. Oxford University Press: Oxford (1997).

APPENDIX A

TURBULENCE ENERGY SPECTRUM FUNCTION

According to Richardson [in 19], the kinetic energy enters turbulence through the large scales of motion which are proportional to the geometry of the flow. These scales also known as eddies are highly unstable and break up transferring their energies to somewhat smaller eddies. This energy cascading process continues from small eddies to smaller eddies until in the smallest eddy, the Reynolds number is sufficiently small, eddy motion is stable, and the molecular viscosity is effective in dissipating the kinetic energy.

From Kolmogorov's first similarity hypothesis, we know that velocity statistics pertaining to the universal equilibrium range have a universal form that is uniquely determined by the dissipation rate (ε) and kinematic viscosity (ν). Kolmogorov's second similarity hypothesis predicts that the energy spectrum function has a universal form uniquely determined by ε, independent of ν.

Figure A-1 shows the typical energy spectrum for a high Reynolds number normalized by the kolmogorov scales. It shows the various ranges in the scales of motion. Based on the Kolmogorov's hypothesis, the energy containing range is the only range that is dependent on the particular flow. Figure b gives the energy spectrum normalized by the kolmogorov scales for two different Reynolds number of flow. The dissipation ranges for both these Reynolds number are similar, while the energy containing range moves to lower values of $k\eta$ as Reynolds number increases.

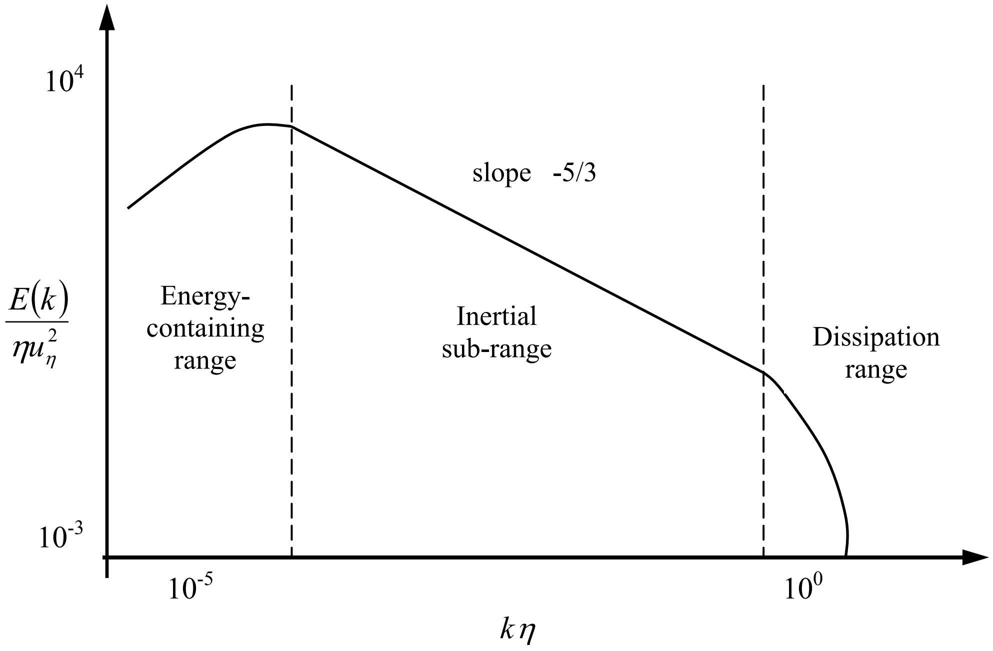

Figure A- 1: Typical energy spectrum for a high Reynolds number turbulent flow normalized by Kolmogorov scales

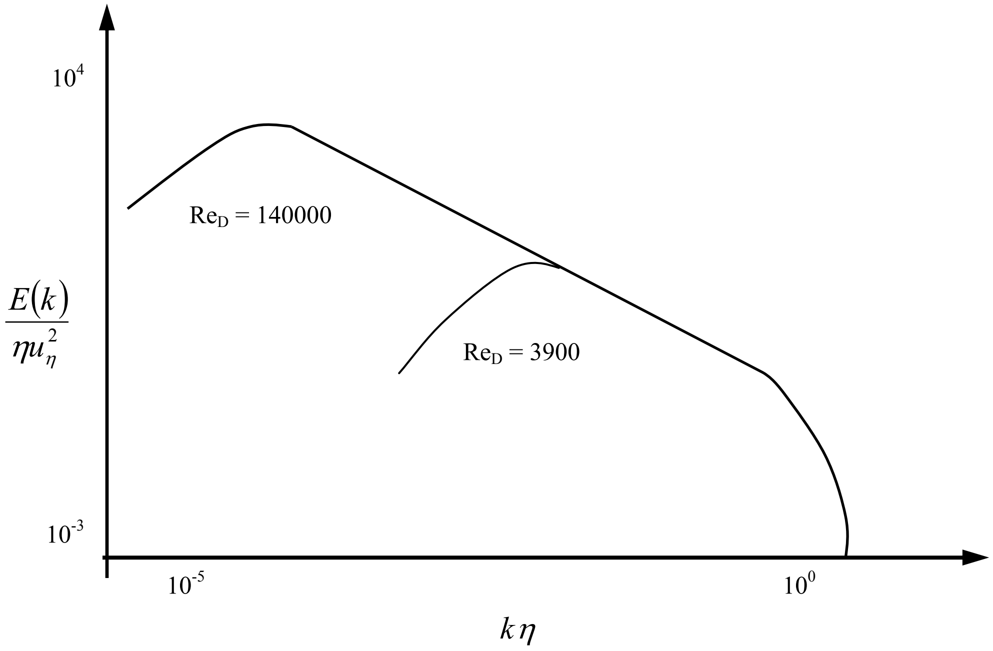

Figure A- 2: The Energy spectrum for various Reynolds number scaled by kolmogorov scales

From figure A-2 we can conclude that for lower Reynolds number of flows, the inertial range is not extensive as in the higher Reynolds number case. This concept can be more clearly understood from figure A-3 which gives the energy and dissipation spectra normalized by the kolmogorov scales at Re_D 140000 and Re_D 3900. The high Reynolds number case has more kinetic energy content. Consequently the energy spectra are scaled by different numerical factors so that they can be compared on the same plot. From figure c we can clearly observe that for the high Reynolds number case the overlap area between the energy spectra and dissipation spectra is less whereas the energy spectra and the dissipation spectra overlap significantly indicating that there is no clear separation of scales.

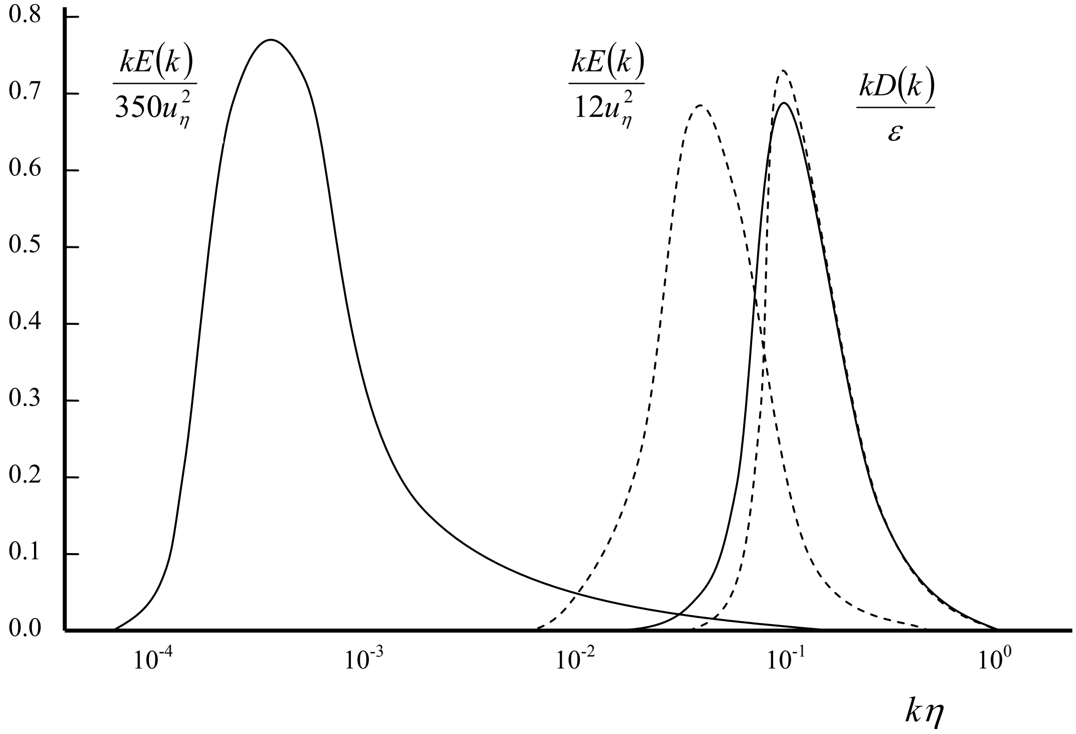

Figure A- 3: Energy and Dissipation spectra normalized by the kolmogorov scales at Re_D 140,000 (solid lines) and Re_D 3900 (dashed lines)

While performing PANS calculations for the high Reynolds number cases, placing the cut-off in the inertial sub-range by having f_k = 0.7 or 0.5, we are still clear of the dissipation scales i.e. there are no dissipation scales being resolved. So f_ε = 1 for this case. Whereas for the low Reynolds number case when we place the cut-off in the inertial scales by having f_k = 0.7 or 0.5 we might be resolving some dissipation scales and this necessitates changing f_ε to account for the resolving of the dissipation scales.

VITA

Sunil Lakshmipathy received his B.E. degree in mechanical engineering from Bangalore University in 1999. He worked as an assistant systems engineer for Tata Consultancy Services before joining the Master's program in aerospace engineering at Texas A&M University in September 2001 and graduated in December 2004. He worked as an intern for Robert Bosch GmBH from October 2003 to April 2004. His areas of interest include CFD and turbulence modeling. He can be contacted through Dr. Sharath S. Girimaji at the Aerospace Engineering Department at Texas A&M University, College Station, TX 77843-3141.